UNIVERSIDAD NACIONAL AUTÓNOMA DE MÉXICO
PROGRAMA DE MAESTRÍA Y DOCTORADO EN INGENIERÍA
INGENIERÍA ELÉCTRICA – SISTEMAS ELÉCTRICOS DE POTENCIA

THERMO-ELECTROMAGNETIC LUMPED PARAMETER MODEL OF A SUPERCONDUCTING SYNCHRONOUS GENERATOR FOR WIND POWER GENERATION

TESIS
QUE PARA OPTAR POR EL GRADO DE:
DOCTOR EN INGENIERÍA

PRESENTA:
ALEJANDRO BAEZ MUÑOZ

TUTORES PRINCIPALES
DR. FREDERIC TRILLAUD, INSTITUTO DE INGENIERÍA, UNAM
DR. JUAN RAMÓN RODRÍGUEZ RODRÍGUEZ, FACULTAD DE INGENIERÍA, UNAM
COMITÉ TUTOR
DR. LUIS MIGUEL CASTRO GONZÁLEZ, FACULTAD DE INGENIERÍA, UNAM
DR. RAFAEL ESCARELA PÉREZ, UAM-AZCAPOTZALCO
DR. HOCINE MENANA, UNIVERSITY OF LORRAINE, NANCY-FRANCE

CIUDAD UNIVERSITARIA, CD. MX., ENERO 2023

JURADO ASIGNADO:

Presidente:	Dr. Rodríguez Rodríguez Juan Ramón
Secretario:	Dr. Castro González Luis Miguel
1 er. Vocal:	Dr. Trillaud Frédéric
2 do. Vocal:	Dr. Escarela Pérez Rafael
3 er. Vocal:	Dr. Menana Hocine

Esta tesis se realizó en el Instituto de Ingeniería, UNAM.

TUTORES DE TESIS:

Dr. Frédéric Trillaud   Dr. Juan Ramón Rodríguez Rodríguez

_____   _____
FIRMA   **FIRMA**

To-morrow, and to-morrow, and to-morrow,
Creeps in this petty pace from day to day
To the last syllable of recorded time,
And all our yesterdays have lighted fools
The way to dusty death. Out, out, brief candle!
Life's but a walking shadow, a poor player
That struts and frets his hour upon the stage
And then is heard no more: it is a tale
Told by an idiot, full of sound and fury,
Signifying nothing.

William Shakespeare

Declaration

I hereby declare that except where specific reference is made to the work of others, the contents of this dissertation are original and have not been submitted in whole or in part for consideration for any other degree or qualification in this, or any other university. This dissertation is my own work and contains nothing which is the outcome of work done in collaboration with others, except as specified in the text and Acknowledgements. This dissertation contains fewer than 65,000 words including appendices, bibliography, footnotes, tables and equations and has fewer than 150 figures.

<div align="right">

Alejandro Baez Muñoz
Noviembre 2023

</div>

Declaración

Por la presente declaro que, salvo cuando se haga referencia específica al trabajo de otros, el contenido de esta tesis doctoral es original y no ha sido presentada, en su totalidad o en parte, para la consideración de cualquier otro título o calificación en esta o cualquier otra universidad. Declaro que en esta tesis se presenta un trabajo propio y original y no contiene nada que sea el resultado de un trabajo realizado en colaboración con otros, excepto lo que se especifica en el texto y en los agradecimientos. El presente trabajo contiene menos de 65.000 palabras, incluyendo apéndices, bibliografía, notas al pie, tablas y ecuaciones, y tiene menos de 150 figuras.

Alejandro Baez Muñoz
November 2023

Acknowledgements

I would like to express my deepest gratitude to my esteemed supervisor, Dr. Frederic Trillaud, for his invaluable guidance, support, and push throughout my doctoral journey. His exceptional mentorship, profound knowledge, and strong dedication have been instrumental in shaping my research capabilities, academic approach, and personal growth. His belief in my abilities has instilled in me a sense of responsability and duty that has carried me through the challenges of this endeavor.

I am also deeply indebted to Dr. Luis Miguel Castro for his insightful contributions, constructive criticism, and support. His rigorous guidance and thorough feedback have enriched my understanding of the research topic and broadened my perspectives, enabling me to approach the research with greater depth and clarity. His dedication to academic excellence has served as an inspiration throughout my doctoral studies.

I extend my sincere gratitude to Dr. Rafael Escarela from the Universidad Autónoma Metropolitana, and Dr. Hocine Menana from the University of Lorraine, France, for their invaluable intellectual stimulation and unwavering support. Their expertise and insights have guided me to solidify my knowledge and develop innovative strategies for the presented work.

I would like to express my heartfelt appreciation to my co-supervisor, Dr. Juan Ramón Rodriguez, for his guidance in the field of power electronics. His expertise and insights have been instrumental in refining my understanding of complex concepts. I am also grateful for the opportunity to participate in the course "DFIG Wind Turbine Control" taught by Dr. David Campos of Strathclyde University, a valuable learning experience made possible by Dr. Rodriguez's guidance.

I am also grateful to my doctoral colleagues, particularly M.Eng. Wilder Durante, for his camaraderie, support, and expertise in FEM studies and the use of specialized software. His willingness to share his knowledge and collaborate on research projects has been invaluable

Finally, I would like to express my special thanks to my mother, Maria del Carmen Muñoz, for her understanding and unwavering support throughout my doctoral journey. Her belief in me has been a source of strength and motivation, enabling me to persevere through the challenges. Her encouragement has been an invaluable pillar of support throughout my life.

Abstract

A dynamic lumped-parameter model of a REBCO field coil synchronous generator including details of the thermoelectromagnetic phenomenology of the superconducting coil is presented in the classic dq0 frame of reference. The electrical, thermal and magnetic REBCO field coil models are built through equivalent circuit networks. The magnetic modeling is constructed by using the magnetic equivalent circuit (MEC) method based in a magnetic finite element model (FEM) to estimate the magnetic flux distribution in the HTS machine and particularly in the HTS field coil. The main objective is to introduce a more traditional approach through a generic-like model of High Temperature Superconducting (HTS) field coil Synchronous Machine (SM) at a reasonable accuracy avoiding the shortcomings of using the FEM in terms of complexity, computation time and resources. This modeling framework is capable of inferring trends in the behavior of HTS machines connected to power grids under typical transients, which can be useful for power systems engineering studies.

The model can be easily coupled with external circuits related to renewable energy conversion applications, such as wind energy systems. In this context, an HTS field coil synchronous machine for wind power applications is designed to demonstrate the effectiveness of the proposed model and its easy coupling capacity with external circuits. Then, the proposed model is used to identify the fundamental transient problems of the grid-connected HTS field coil machine under the most severe operating condition, which is a three-phase short circuit at the stator terminals (i.e., the terminals associated with the wind power converter). Thus, two cases are considered: 1) no full transition of the HTS to the normal-resistive state under stable condition, 2) full transition of the HTS under unstable condition. The response of the HTS machine is compared against that of a conventional machine. The corresponding analysis is then used to find a basis for understanding the fundamental behavior of HTS wind generators connected to an electrical grid. Further work will require analyzing the wind power converter system and its related control schemes coupled with the HTS field coil SM.

Table of contents

List of figures

List of tables

Chapter 1

Introduction

1.1 Motivation

The modeling of superconducting (SC) materials presents a complex challenge due to various physical phenomena involved, including thermal, electrical, magnetic, and mechanical effects. The finite element (FE) method is often used to model these materials for accurate and reliable results. However, the implementation, computational time, and memory requirements of a finite element model (FEM) of a superconducting winding in a rotating machine for power systems engineering studies can be prohibitively complex. As a result, the motivation of this project is to find an alternative approach to simulating hundreds of high temperature superconductor (HTS) tape in a field-wound synchronous machine (SM) without using the FEM that consumes large amounts of computation resources. Instead, a generic multiphysics lumped-parameter model may represent an advantageous alternative on the SC dynamic response in steady state and transients operation. Such lumped-parameter models can be easily implemented in dynamic simulators such as Matlab/Simulink and EMTP software.

1.2 Objectives

a) Develop a thermoelectromagnetic lumped-parameter reference model for the HTS field winding of a SM.

b) Integrate the thermoelectromagnetic HTS field coil model into a 8th order SM model.

c) Develop an HTS-SM model that can be easily integrated with external circuits related to renewable energy conversion applications.

d) Conduct transient studies in a designed 15 MW HTS field coil machine for wind power applications.

e) Analyze and benchmark the thermoelectromagnetic HTS field coil SM model in the dq0 frame of reference against a conventional SM with the same operation conditions.

f) Simulation of the thermoelectromagnetic HTS field coil SM model connected to the grid through a full-scale power converter.

1.3   Justification

By 2050, solar power is predicted to become the top global electricity source generation [1]. However, even with the available solar energy potential, its lower average capacity factor (CF) of 19% to 31% and lack of inertia raise concerns about the stability of future power systems. On the other hand, wind energy is expected to rank fourth, with an average CF of 18% to 49% for onshore and 30% to 53% for offshore technologies [2]. Offshore wind energy has a higher CF due to less variation and higher wind velocities compared to onshore technologies. For the offshore development, wind turbines ought to be optimized in size, weight, maintenance cycle, and power density to meet the increasing demand for renewable energies at a reduced cost. For example, using the gearbox typically found in wind turbines with double fed induction machines can lead to frequent maintenance and failures [3]. Therefore, direct-drive wind turbines where the rotor turbine are direclty coupled with the generator shaft are a suitable option to reduce the maintanence cycle. This kind of turbines admit two types of electrical generators, permanent magnet (PM) and wounded excitated (WE) synchronous machines (SM). Due to the unpredictable nature of the wind turbine's input kinetic energy in the direct-drive configuration, the voltage and frequency at the stator terminals of the SM fluctuate. In order to establish a connection between the variable frequency stator voltage and the power system, it is imperative to employ a voltage source converter (VSC) that can effectively convert it into a terminal voltage with constant frequency and magnitude. This conversion is vital to ensure optimal coupling with the interconnected power system. In addition, the dc-link capacitors in the VSC can emulate larger inertia in direct drive wind turbines than their original capacity by using emulated inertia control [4, 5]. As a result, wind energy conversion systems can be integrated into power systems without significantly compromising grid stability. The General Electric offshore direct-drive wind turbine with a power capacity of 14 MW is one of the most significant developments in wind turbines today. This turbine is equipped with a PM-SM and is projected to maintain a capacity factor ranging from 60% to 64% [6].

However, PM machines require large amounts of rare earth elements (RE), such as dysprosium and neodymium, to achieve this power capacity [7]. Dysprosium, for example, is more difficult to extract and process than many other REs and comparably more valuable. Furthermore, the quasi-monopolistic dominance of China over RE processing and permanent magnet production may become a problem due to the projected increasing demand for wind energy sources on the world future power grids [8–10]. Consequently, wind turbines development requires improving the electrical generator power density capability and the efficiency while maintaining a reduced volume and low RE consumption [11]. Two feasible options for above 10 MW output power wind turbines could meet the criteria of enhanced power density and a larger efficiency: the SC-SM and the magnetic pseudo direct drive (PDD) SM. The first one can reduce the weight and size of the machine while increasing the rotor magnetic flux density capacity without electrical power losses [12–14]. The second option can achieve the same effect by increasing rotor speed through a magnetic gearbox without mechanical power losses [15]. Both machines have their pros and cons as shown in Table 1.1. However, if PM machines need approximately 250 kg of rare earth elements to produce the same power capacity that SC machines can achieve with only 2 kg [16]. Consequenlty, the PDD-SM requires even more RE for the magnetic gearbox. Additionally, the elements needed for superconductors are not as rare as those needed for PMs. So, even if a RE supply chain issue is present in the future, the SC machine technology applied to wind energy conversion systems could mantain its growing rate to satisfy the wind energy demand. Finally, the enviromental impact can be reduced with the SC machines thus making it a better option for the future development of wind turbines.

Table 1.1 Comparison between the SC-SM and the PDD-SM. The pros are represented with (+), whereas the cons with (-).

Characteristic	SC-SM	PDD-SM
Cooling method	(–) Cryogenic	(-) Conventional
Maintanence and repairment	(+) Reduced	(+) Reduced
Overall cost	(-) High-cost SC materials	(+) Low-cost PM
Weight and size	(+) Reduced	(+) Reduced
Rare earth consumption	(+) Reduced	(–) Higher
Iron requirement	(+) Reduced	(-) Higher
Efficience	(+) Higher	(+) Higher

1.4   Contribution

A nonlinear superconducting field coil resistance model is developed and integrated into a classical dq0 frame of reference SM model. A 2D heat flux model has been developed through an equivalent thermoelectric circuit to predict the thermal behavior of such a coil enveloped within a modular cryostat topology. Furthermore, the proposed lumped parameter magnetic model is a novel and original contribution that accurately estimates the magnetic behavior of the HTS field coil through a flexible code that includes the superconductor screening currents. Thus, a generic modeling framework in the dq0 frame of reference is proposed for power systems engineering studies to infer trends in the behavior of an HTS field coil machine connected to a power grid. The dq0 model facilitates the integration of a variable frequency power converter model for renewable energy systems studies. The presented lumped parameter model avoids the shortcomings of the finite element model in terms of computation time and resources when simulating the HTS machine coupled to external circuits under transient conditions, allowing the study of complex transient regimes with duration of several power cycles including diverse coil configurations to account for the performance of the HTS winding.

1.5   Hypothesis

- The proposed thermoelectromagnetic lumped parameter model of the HTS field coil synchronous machine assumes a homogeneous, isotropic, and non-dispersive distribution of the corresponding scalar and vectorial quantities.

- The relative motion between the stator and rotor is neglected in the magnetic model, so the simulation results correspond only to an estimate of the machine's real behavior.

- The magnetic finite element method (FEM) neglects the dependence of the thermal and magnetic critical current on the HTS coil. However, a set of fitted parameters can be used to model the non-uniform distribution of current density in the superconducting coils. This approach should be based on the coil shape and tape technology.

- The dq0 HTS-SM model does not account for saturation or harmonic distortion.

- The proposed model can be easily coupled with external circuits in the dq0 or the abc reference frame.

- A strategy for regulating the stator d-axis reference current to zero is adopted to facilitate the HTS generator speed control within a wind power system.

Chapter 2

State of art

2.1 Brief history of superconductivity

In the early 20th century, the Dutch physicist Heike Kamerlingh Onnes at Leiden Institute achieved the liquefaction of helium motivated by a growing scientific interest in gas liquefaction. This breakthrough prompted further exploration of material properties at low temperatures, including electrical resistivity. Onnes conducted research on various metals before turning to pure mercury, where he observed that its electrical resistance suddenly decreased to zero just below a temperature of 4.2K, which led to the discovery of the superconducting state. Onnes also discovered that the zero potential difference exhibited by a sample in this new state only lasts until a specific current and magnetic field threshold is reached, after which it sharply increases [17]. Following this achievement, it was discovered that other elemental metals could reach the SC state by decreasing their temperature below a specific threshold unique to each material, called the critical temperature T_c. The magnetic properties of the SC state were not fully understood until 1933 when W. Hans Meissner and Robert Ochsenfeld found that below their critical temperature, certain superconducting materials can also expel the magnetic flux from within when exposed to an external magnetic field (Meissner effect), as long as this value does not exceed a threshold, known as the critical magnetic field H_c [18]. In 1935, Fritz and Heinz London proposed a phenomenological theory of the electromagnetic properties of superconductors in the Meissner effect, explaining how the magnetic field penetrates the SC material for a short distance from the surface, which served as the basis for understanding superconductivity in the subsequent years [19]. In 1950, Ginzburg and Landau overcame the limitations of some physics assumptions as in the London theory. Seven years later, in 1957, John Bardeen, Leon N. Cooper, and J. Robert Schrieffer developed the BCS theory, which incorporated the London theory with modifications brought by the quantum mechanics, and by describing the true nature and source of the SC state

through the concept of Cooper pairs [20]. By 1962, research and development of materials gave way to a new class of superconductors known as type II superconductors that made it possible to understand many unknown properties of superconducting materials until that moment [21]. Under 75 years of research on superconductivity, the only available SC wires to be used in actual applications were the low-temperature superconductors (LTS) with a T_c of about 23 K for a compound of niobium and germanium. However, early in 1986, evidence for superconductivity in an oxide of lanthanum, barium and cooper at temperatures of about 30 K was reported by J. Georg Bednorz and Karl Alex Muller [22]. Furthermore, one year later M. K. Wu, J. R. Ashburn, and C. J. Torng published a paper where superconductivity was achieved in a new mixed-phase Y-Ba-Cu-O compound system at ambient pressure with a critical temperature of about 93 K [23], and with it, a new era of SC materials known as high-temperature superconductors (HTS) was born.

2.2 Types of superconductors

2.2.1 Type-I superconductors

The SC materials which present zero resistance and the Meissner effect below a given critical temperature and a given critical magnetic field are defined as type-I superconductors. The Meissner effect is characterized by the total exclusion of the magnetic field from the interior of the SC material by means of screening currents circulating below the surface of the sample over a thin layer with thickness λ_L, known as London penetration depth [19]. Type-I superconductors exhibit a single critical external magnetic field H_{c0}, as shown in Fig. 2.1.
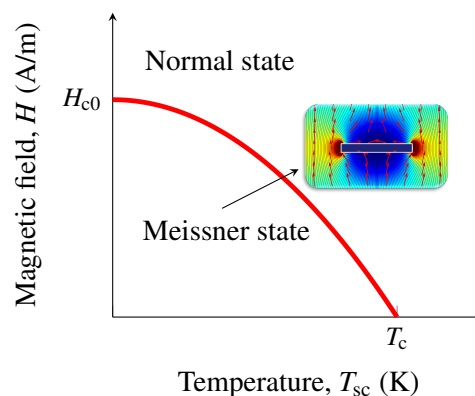
Fig. 2.1 Phase diagram for type-I superconductor.

2.2.2 Type-II superconductors

The type-II superconductors are characterized by their reversible magnetic behavior. The Meissner effect is present below the first critical magnetic field H_{c1}, while the normal state is found above a second critical magnetic field H_{c2}. The phase between H_{c1} and H_{c2} is known as the mixed state. When the magnetic field overpasses H_{c1} without exceeding H_{c2}, the magnetic flux penetrates the SC sample as quantized flux tubes (fluxoids) inducing supercurrents that circulate around them, known as Abrikosov vortices. These vortices are pinned to the material defects (known as the "pinning force") creating an opposite magnetic flux that expels the external applied one from the superconducting regions. Any change in the input current or the external magnetic field will force the vortices to rearrange themselves at a new point of operation where all vortices are pinned again. Under such a context, a Lorentz force will be created due to the input current and magnetic flux density interaction, whose magnitude must be lower than the pinning force to avoid the vortices movement that induce an electric field, i.e., an increase in the material resistivity related to energy disipation. As the magnetic field increases towards H_{c2}, the number of vortices increase until the SC state is destroyed.

The mixed state represents the occurence of superconductivity coexisting with the normal state, as shown in Fig. 2.2. All of the HTS materials are type-II superconductors. They can conduct high currents under relatively large applied magnetic fields, suitable for power system applications.
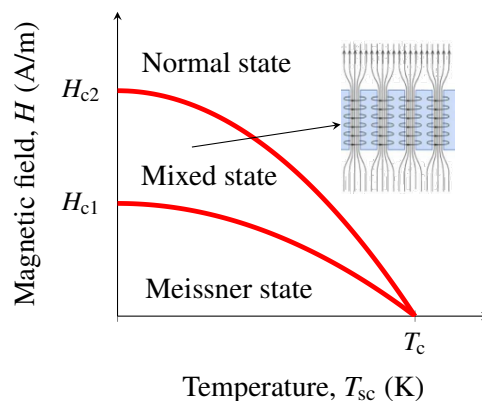
Fig. 2.2 Phase diagram for type-II superconductor.

(a) MgB2,
$T_c = 39$ K [24].

(b) BSCCO,
$T_c = 108$ K [25].

(c) REBCO,
$T_c = 92$ K [26].
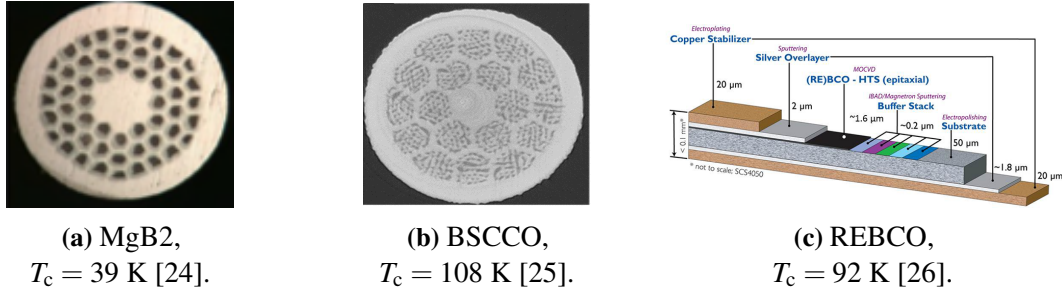
Fig. 2.3 Commercial HTS conductors.

2.3   2G-HTS conductors

After more than thirty years of the HTS materials discovery, HTS wires are available for different applications including power systems equipment. These wires may contain HTS compounds as Magnesium Diboride (MgB2), Bismuth strontium calcium copper oxide (BSCCO), or Rare-earth (RE) barium cooper oxide (REBCO) [24–28]. Fig. 2.3 illustrates the HTS wires with their corresponding T_c that are commonly used in power system devices, such as SC fault current limiters (SCFCL), SC magnetic energy storage systems SMES, flywheels, and HTS wind generators. Typically, the REBCO coated conductors comprise different layers of metallic, substrate and RE materials as illustrated in Fig. 2.3c. Indeed, the metallic layers comprises copper and silver while the substrate corresponds to a compund known as Hastelloy. REs such as gadolinium, samarium or yttrium are used depending on the manufacturer.

The HTS layer resistance of a l_{tp} length sample given by (2.2) is modeled from the V-I characteristic (see Fig.2.4) obtained from experimental measurements and fitted through a power law [29], as follows,

$$V = V_c \left(\frac{i_{sc}}{I_c} \right)^n \tag{2.1}$$

where $V_c = E_c l_{tp}$ is the critical voltage; E_c is an arbitrary critical electric field criterion ranging from 0.1 to 10 μV/cm; n is the index value of transition. While the critical current I_c is the current at which the voltage drop between the voltage probes of a SC sample rises above the critical voltage. This property depends on the superconductor's type, quality, and preparation method that impacts the SC thermoelectromagnetic behavior from which the corresponding resistance is obtained [30, 31].

$$R_{sc}(i_{sc}, T_{sc}, B) = \frac{V_c}{I_c^n(T_{sc}, B)} i_{sc}^{n-1} \tag{2.2}$$
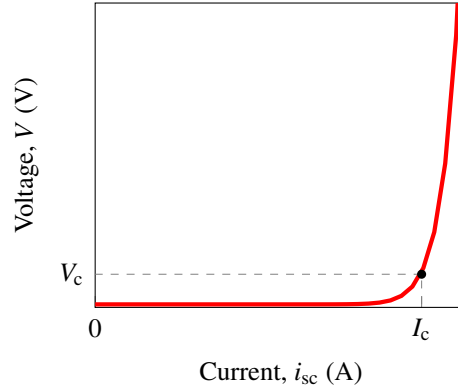
Fig. 2.4 REBCO *V*-*I* characteristic.

Assuming the electric field and the current density constant through the cross-section of the superconductor *E*-*J* relation can be inferred from (2.1) as,

$$\mathbf{E} = E_c \frac{\mathbf{J}}{J_c}^n |\mathbf{J}|^{n-1} \tag{2.3}$$

where J_c is the critical current density defined as I_{c0}/A_{sc}, with A_{sc} being the cross section of the SC layer. The non-linear resistivity of the HTS material can be derived from (2.3), and is given by,

$$\rho_{sc} = \frac{E_c}{J_c^n} |\mathbf{J}|^{n-1} \tag{2.4}$$

2.4 Critical current and n index of transition

The critical current I_c and the index n of transition are determined from the *V*-*I* characteristic measured at a reference temperature T_{ref} and in self-field (SF) condition. As a result, $I_{c0} = I_c(T_{ref})$ and $n_0 = n(T_{ref})$ provide reference values for the critical current and the index of transition. The parameters I_c and n depend on temperature and magnetic flux density. Furthermore, their properties may change from supplier to supplier due to the complexity of manufacturing HTS materials [32]. The critical currents of different tapes from various manufacturers have been characterized by many. It is possible to express I_c and n as functions depending on different parameters as follows,

$$I_c = I_{c0} \cdot I_{c,T}(T_{sc}) \cdot I_{c,B}(B_{sc}, \theta_{sc}) \tag{2.5}$$

$$n = n_0 \cdot n_T(T_{sc}) \cdot n_B(B_{sc}) \tag{2.6}$$

where $I_{c,T}$, $I_{c,B}$, n_T and n_B are empirical functions that can be fitted to actual measurements.

2.4.1 Thermal dependence of critical current and n index of transition

When dealing with REBCO thin films, the dependence of the critical current on temperature can be modeled as a linear function as follows [31],

$$I_{c,T}(T_{sc}) = \left(\frac{T_{sc} - T_c}{T_{ref} - T_c} \right) I_c(T_{ref}) \tag{2.7}$$

while the *n* index of transition is given by,

$$n_T = n_0 \frac{T_{ref}}{T_{sc}} \tag{2.8}$$

By substituting T_{sc} with T_{cs} in (2.7) and equating the corresponding critical current with the operational current (i_{fd}). The current sharing temperature may be expressed as follows,

$$T_{cs} = \frac{|i_{fd}|}{I_c(T_{ref})} (T_{ref} - T_c) + T_c \tag{2.9}$$

The linear relationship between the critical current and the SC layer temperature is shown in Fig. 2.5a. The linear function approach is not entirely true near the critical current value. Nevertheless, it provides a simple approximation to represent the temperature impact on the critical current for transients studies [31].
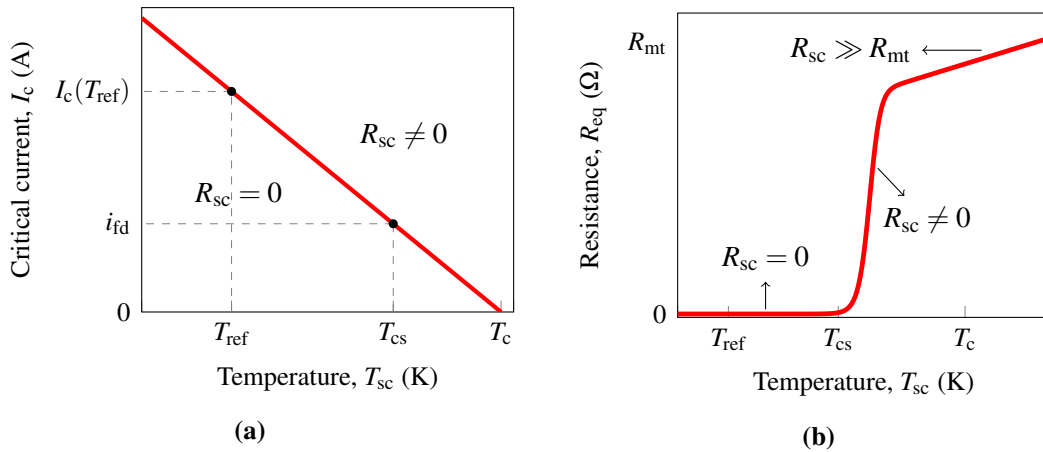
Fig. 2.5 Thermal impact on the SC resistance: (a) Dependence of the critical current on SC layer temperature. (b) Equivalent parallel resistance as a function of the SC layer temperature.

For REBCO coated conductors at a reference temperature $T_{\text{ref}} = 77$ K, in the nominal regime the current flows solely in the HTS layer ($R_{\text{sc}} \rightarrow 0$) as long as its local temperature T_{sc} remains below a current-sharing temperature T_{cs}. Whereas it redistributes amongst all the layers (metallic and HTS) during transients $(R_{\text{sc}} \neq 0)$ when T_{sc} rises above T_{cs}. In case the transient causes the SC state to quench, the resistance of the HTS layer will increase significantly compared to the metallic layers resistance value. As a result, the equivalent parallel resistance R_{eq} conformed by the metallic layers and the HTS layer will saturate at the equivalent metallic resistance R_{mt}. The current will then flow in the metallic layers and not the superconductor. Fig. 2.5b provides an illustration of how R_{eq} changes with temperature.

2.4.2 Magnetic dependence of critical current

The most widely used analytical equations for modeling the dependence of critical current on magnetic flux density over HTS tapes are shown in Table 2.1. The majority of the presented models rely on the external magnetic flux density's magnitude $|\mathbf{B}|$, and the constant fitting parameters specific to each model, such as B_0, α, k, v, and u [33]. The adapted Kim and power-law model considers the local orthonormal components of the magnetic flux density, $B_{\parallel}$ and $B_{\perp}$, which are paralell and perpendicular to the wider surface of the tape, respectively. The magneto-angular anisotropy model, which is an adaptation of the Kim-power-law model with anisotropy, considers the impact of $|B|$ and its corresponding angle θ with respect to the tape's parallel face.

Fig. 2.6a shows the evolution of I_{c} as a function of $|\mathbf{B}|$ applied perpendicularly and parallely to the tape surface by assuming a constant operating temperature over the magneto-angular anisotropy model. While Fig. 2.6b shows the evolution of the critical current according to the angular direction θ of the applied magnetic flux density for two magnitudes of applied magnetic flux density. In addition, Fig. 2.6c shows the definition of the angular direction compared to the tape surface. The critical current diminishes with a magnetic field perpendicular to the tape surface compared to a parallel magnetic field. The magneto-angular anisotropy fitting parameters for Fig. 2.6 were extracted from an experimental database provided to the community by the Robinson Institute at the University of Victoria in New Zealand [29, 34]).

Table 2.1 Available models to represent the I_c dependence with external magnetic field **B** [35, 36].

Model	Equation	Model	Equation
Kim	$I_c = I_{c0}\left(1 + \dfrac{|\mathbf{B}|}{B_0}\right)^{-1}$	Power-law	$I_c = \dfrac{I_{c0}}{|\mathbf{B}|^{\alpha}}$
Linear	$I_c = I_{c0}\left(\dfrac{B_0 - |\mathbf{B}|}{B_0}\right)$, if $|\mathbf{B}| < B_0$ $I_c = 0,$ if $|\mathbf{B}| \geq B_0$	Exponential	$I_c = I_{c0}\exp\left(-\dfrac{|\mathbf{B}|}{B_0}\right)$
Adapted Kim and Power-law	$I_c = I_{c0}\left(1 + \dfrac{\sqrt{k^2 B_\parallel^2 + B_\perp^2}}{B_0}\right)^{-\alpha}$	Adapted Kim and Power-law with anisotropy	$I_{c,k} = I_{c0,k}\left(1 + \dfrac{|\mathbf{B}| f_k(\theta)}{B_{0,k}}\right)^{-\alpha_k}$ $f_k(\theta) = \sqrt{v_k^2 \cos^2(\theta - \delta_k) + u_k^2 \sin^2(\theta - \delta_k)}$
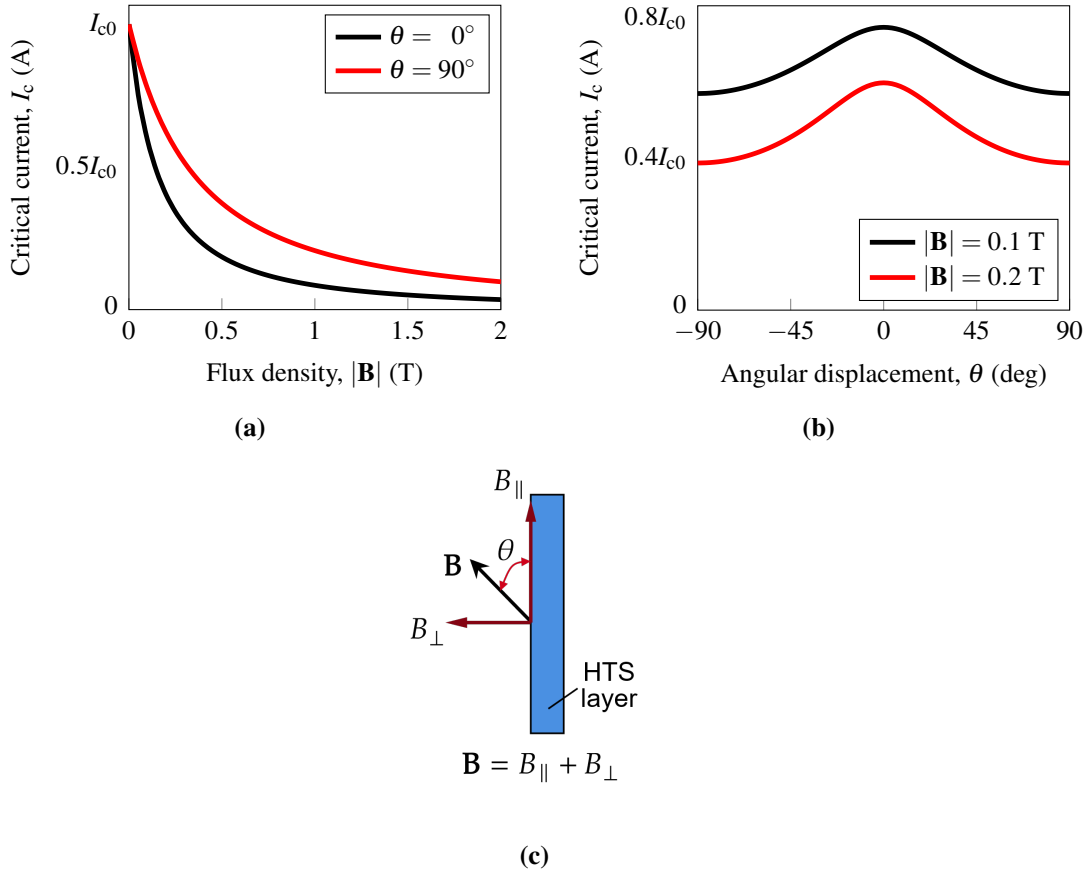
Fig. 2.6 Impact of the magnetic flux density on the critical current I_c by using the magneto-angular anisotropy model. (a) Critical current vs. Flux density. (b) Critical current vs. Flux density angular direction. (c) Definition of the angular direction θ of the applied magnetic flux density **B** compared to the tape surface.

2.5   HTS rotating machines

Few companies designed and tested LTS rotating machines from the 70s through the 90s. These machines exhibited superior performance in terms of improved reactive power under overexcited and underexcited operating conditions, longer rotor life, and higher efficiency even under partial load conditions, as compared to conventional technologies of the same era [37]. Almost all the designed machines were high-powered synchronous machines with niobium-titanium (NbTi) field windings cooled by helium gas for utility and military applications, as shown in Table 2.2. However, the cost of the LTS wires, the helium requirement and the complex cryogenic system did not make these machines economically competitive technology.

Table 2.2 LTS rotating machines projects over time [38].

Year	Company	Country	Application	Power (MW)	Speed (rpm)	Poles	Cryogenic cooling	Conductor type
1972	Westinghouse	USA	Utility	5	-	-	He	NbTi
1974	Westinghouse	USA	Aeronautical	5/10	12000	4	He	NbTi
1978	SuperGM	Japan	Utility	78	3600	-	He	NbTi
1978	GE	USA	Utility	20	3600	2	He	NbTi
1978	Westinghouse	USA	Utility	300	3600	2	He	NbTi
1970s	Alstom	France	Utility	250	-	-	He	NbTi
1980	GE	USA	Air Force	20	7000	-	He	NbTi Nb3Sn
1982	GE & Alstom	USA France	Utility	250	3000	-	He	NbTi
1983	GE	USA	Navy	2.25	1200	-	He	NbTi
1987	GE & Alstom	USA France	Demo	0.018	3000	-	He	NbTi

The HTS materials discovery in 1986 and the rapid advances in their development resulted in windings operating at higher temperatures than the LTS materials, with a simpler cryogenic system. Cryogenic coolant for HTS wires are neon, hydrogen, or nitrogen, making HTS machine technology more suitable and economically feasible for power applications than LTS electrical machines. At the end of the nineties and until now, high-torque propulsion motors, synchronous condensers, and large generators for wind, marine, and hydro applications were developed using HTS wire technology [38–42]. As the number of HTS wire manufacturers increases and the cost of HTS materials potentially decreases due to rising demand, the prominent advantages of HTS-based equipment, such as increased power density, efficiency, enhanced electrical stability, and low RE consumption, may become a reality in the near future.

Table 2.3 HTS rotating machines projects over time [38, 42].

Year	Company	Country	Application	Power (MW)	Speed (rpm)	Poles	Cryogenic cooling	Conductor type
1996	Rockwell Automation	USA	Industrial	0.15	1800	4	Ne	BSCCO
2000	Rockwell Automation	USA	Industrial	0.74	1800	4	Ne	BSCCO
2001	AMSC	USA	Industrial	3.73	1800	4	Ne	BSCCO
2001	Siemens	Germany	Demo	0.4	1500	4	Ne	1G-HTS
2003	AMSC	USA	Navy	5	200	6	He	BSCCO
2003	AMSC	USA	Navy	36.5	120	-	He	BSCCO
2003	GE	USA	Utility	1.5	3600	-	He	BSCCO
2004	Siemens	Germany	Generator	4	3600	-	Ne	1G-HTS
2005	General Atomics	USA	Navy	37	-	-	He	NbTi
2005	AMSC	USA	Utility	8	1800	-	Ne	BSCCO
2006	Siemens	Germany	Navy	4	120	-	-	
2007	AMSC	USA	Marine	36.5	120	-	He	-
2008	GE	USA	Aerospace	1.3	10000	-	Ne	BSCCO
2009	FAMU, NASA, Georgia Tech.	USA	-	0.16	2700	-	-	-
2009	NEDO	Japan	Marine	0.007	360	-	He	YBCO
2009	Converteam	France	Hydro	1.7	214	-	He	BSCCO
2010	Siemens	Germany	Marine	4	120	-	Ne	1G-HTS
2010	KHI	-	Marine	1	190	-	He	BSCCO
2011	Wuhan Institute	China	Marine	1	500	-	N2	BSCCO
2011	Doosan	South Korea	Marine	5	200	-	He	BSCOO
2012	Converteam	France	Hydro	1.7	214	28	He	BISCCO
2012	KHI	-	Marine	3	160	-	He	BSCCO
2013	IHI	-	Marine	0.4	250	-	LN2	BSCCO
2015	Changwon National University	South Korea	Wind	0.01	600	-	Ne	YBCO
2019	Illinois	USA	Aerospace	10	6000	-	-	Nb3Sn
2019	Ecoswing Project	European Union	Wind	3.6	15	40	He	GdBCO
2020	KalsiGPS	-	Wind	10	10	-	He	MgB2
2020	TECO	-	Marine	3.6	1800	-	LN2	YBCO
2020	AMSC	USA	Wind	8	11	-	LN2	YBCO
2020	Changwon National University	South Korea	Wind	12	10	-	He	YBCO

These properties may be decisive in saving fuel and space while improving machine capabilities for onboard applications. Furthermore, for mega-watt range power generation reducing the overall dimensions and weight of the machine to increase efficiency and to improve some features on transient stability issues [43, 44]. From the late 1990s to 2013, almost all HTS machines were designed with BSCCO windings for naval applications. Operating temperatures were higher than those of LTS machines, but helium cooling was still required. In the following years, the main application of HTS machines shifted to wind energy, as shown in Table 2.3.

2.5.1   Common topologies

HTS wires are more suitable for DC field windings than AC ones, due to their known sensitivity to AC fields. As a result, most HTS machine projects have a HTS rotor and a conventional copper armature winding. [45, 46]. The field coil exciter current supply or any power electronic device connected to the machine may create AC currents and fields that may affect the HTS rotor [47]. Most of the HTS rotating electrical machine designs correspond to radial magnetic flux type topology [38, 43, 48], although some axial magnetic flux type machines with HTS windings or HTS bulks have also been developed [49–51]. The radial flux type devices are mostly multi-MW range synchronous machines with HTS-coil rotor. The stator usually is designed with a three-phase copper winding and the rotor with an HTS field winding made of REBCO tapes. The most common topologies for HTS field coil SM are given in Fig. 2.7.
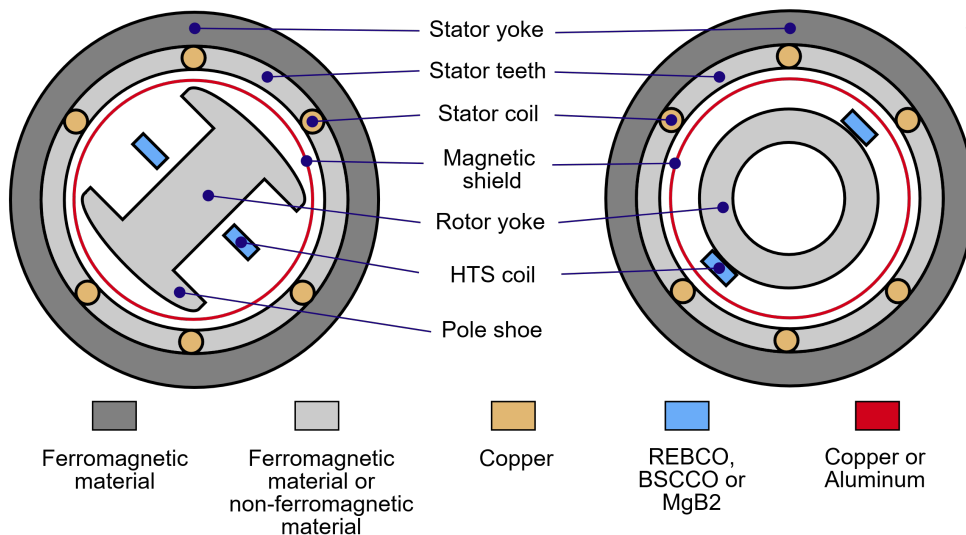
Fig. 2.7 HTS rotating electrical machine common topologies [3, 52].

The rotor configuration may be chosen as a salient pole rotor or smooth rotor comprised of ferromagnetic or nonferromagnetic material (known as air core rotor). In iron-core machine topology, the weight increases and the HTS tape length decreases. This is because the ferromagnetic material in the iron core guides the magnetic flux lines, reducing the ampere-turns needed and the overall cost [53]. On the contrary, an air core rotor does not have any magnetic material so the magnetic leakage increases and more ampere-turns are needed to establish the corresponding magnetic flux over the machine [3]. An air core rotor reduce significantly the machine weight but with an increment in HTS tape length, so the overall machine cost severely rise. Such a configuration presents a reduced synchronous reactance due to the augmented airgap, allowing an improvement in the machine transient stability. However, the reduction in synchronous reactance may create larger short-circuit at the stator currents which lead to large electromechanical strains that can degrade the conductors. The stator topology may be chosen with or without ferromagnetic teeth. Magnetic teeth help to reduce the HTS tape length but adds harmonic content to the resultant airgap magnetomotive force (MMF), while nonmagnetic teeth removes such harmonic content reducing the synchronous reactance but increasing the HTS coil length. Regardless of the topology chosen, an electromagnetic shield is necessary to mitigate the impact of rapid changes in magnetic flux over the HTS coil due to possible machine transients which can produce additional losses in the HTS coil. [54, 55]. A cost-effective HTS rotating machine requires an equilibrium between the usage of ferromagnetic material and HTS length. This is because HTS wires are still relatively costly, and materials development has not yet allowed for larger electromechanical strains [56, 57].

2.5.2   HTS field coil cooling topologies

The HTS coils are indirectly cooled by a cryogenic fluid or gas, using a cryocooler. A cryogenic transfer coupling is used to push cryogen through the coil structure via the opposite drive end shaft extension. [32]. The cryogenic system configuration impact the thermal behavior of the HTS coil. There are two main rotor thermal design concepts, cold and warm rotor [58]. The cold rotor configuration, given in Fig. 2.8a, refers as the cooling of the HTS coils within the same cryogenic system as the rotor structure that supports them, i.e., both elements are at the same temperature. Whereas the warm rotor configuration, shown in Fig. 2.8b, refers as the cooling of the HTS coils separately of the rotor structure that supports them, i.e., both elements are at different temperatures. The main thermal characteristics of cryogenic rotor topologies are presented in Table 2.4, pointing out the pros or cons of cold and warm rotor configurations.
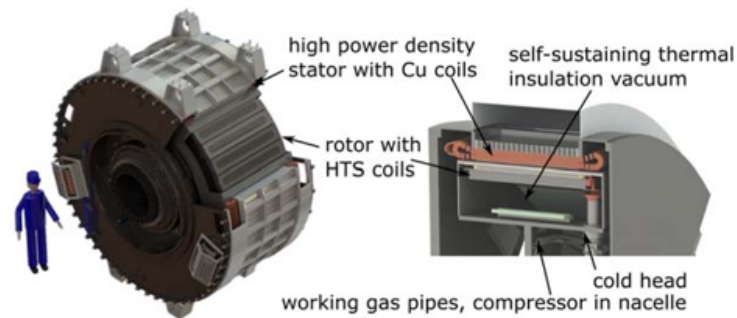
(a) Cold rotor topology [59].
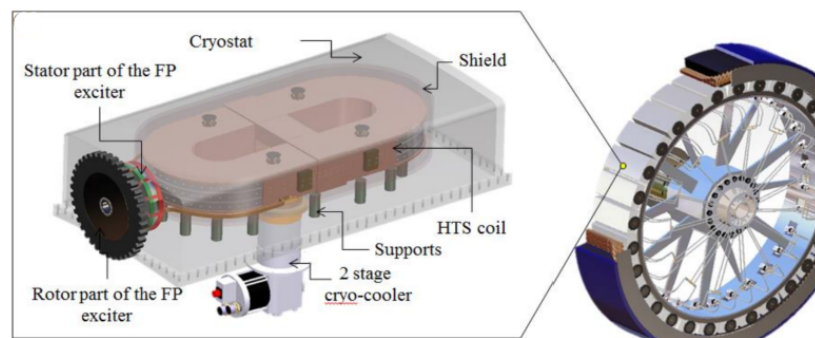
(b) Warm rotor topology [60].

Fig. 2.8 Main thermal concepts rotor designs for HTS machines.

Table 2.4 Main thermal characteristics of cold and warm rotors. The pros are represented with (+), whereas the cons with (-).

Characteristic	Cold rotor	Warm rotor
Cooling rate	(-) Slow	(+) Fast
Maintanence and repairment	(-) Overall rotor	(+) Modular elements
Thermomechanical strains	(+) Less sensitive	(-) Sensitive
Thermal inertia	(+) Large	(-) Smaller
Cryogenic system	(+) Relatively simpler	(-) Complex

2.5.3 HTS generator for wind power applications

As mentioned before, multi-MW HTS rotating machines are machines of reduced volume and weight, at increased power density and efficiency. This is possible due to the rotor high flux density, which sets them apart from conventional direct-drive (DD) wind turbines. Advantages of using DD HTS wind turbine generators are well documented ranging from conceptual designs to component demonstrations or downscaled prototypes [61]. One can

find partially to fully SC generators where both stator and rotor windings are made by SC wires [62], going through topologies with rotating armature where the stator windings rotates around the SC rotor, axial and radial flux type generators and air or iron core concepts [57]. Since raw materials used for producing second-generation (2G) HTS wires are cheap, it is expected that the price of 2G HTS wires would decrease by a factor of 10 if a large amount is demanded by the market [61, 63, 64]. In 2019, the EcoSwing project, funded by the EU Horizon 2020 programme and 9 partners from academia and industry, designed and manufactured the world's first full-scale MW-class DD HTS wind turbine generator. First, the HTS generator was tested to be subsequently installed and operated on a commercial wind turbine located in Thyborøn, Denmark. The rotor of an existing DD PM-SM and its corresponding power converter were replaced with an iron-core SC cold rotor that was wound with REBCO tapes and four low-cost power converters connected to a splitted stator winding. The stator winding was divided into four segments to avoid intense shortcircuit currents which leads to large torque arising from a small synchronous reactance. This modification has resulted in significant improvements to the weigth (25% less than the original PM-SM) and a gain in efficiency of the system up to 92% [14, 59, 65]. Unlike the multi-MW offshore projects, EcoSwing is aiming for the middle-range onshore wind power generation market to demonstrate how the HTS wind turbines may not be only focused on offshore systems but also in onshore ones. This project has achieved a Technological Readiness Level (TRL) of 7 out of the nine levels that exist. The remaining TRL levels pertain to the development and operation in a power grid system. At those stages, simulation of HTS machines interconnected with the electrical network may be convenient to ensure a proper integration into the power system considering the physical constraints of HTS tapes.

2.5.4   HTS rotating machines modeling

Numerical models for HTS have mainly been designed to compute AC losses under various conditions, such as sinusoidal transport current cycles, external magnetic fields, or a combination of both. Simulating the electromagnetic behavior of HTS can be challenging, especially in applications where magnetic fields vary. The magnetic flux density in HTS windings depends on the distribution of current density, which is not uniform. This distribution is affected by screening currents that can cause power losses and increase the temperature of the SC material. Analyzing these issues with the FEM is a typical approach to generate accurate models for traditional and HTS coils [66, 67]. This method can compute the current density distribution and estimate AC loss in HTS coils as given in [68]. Various formulations of the Maxwell's equations have been considered to model HTS wires and coated conductors [69]. Those formulations include the H formulation [70], the T-ϕ formulation [71], the A-V formu-

lation [72], the *T-A* formulation [73, 74], and the *J-A* formulation [75]. Those formulations may be combined with multi-scale or homogenization techniques to achieve accuracy at relatively low computational costs. The best approach was found to be a combination of the *T-A* formulation and the homogenization technique [76]. However, despite the benefits of such approach, it is inefficient in terms of computation resources (time and memory) if transient studies considering several power cycles must be conducted [77]. It becomes unsustainable if relative long transients, such as those present in power grids are simulated. A sudden change in the power system can cause the machine to experience a strong electromagnetic and thermal reaction, which can result in the quench of the HTS winding, disrupting the machine's stability and impacting the electrical network [47]. Additionally, It is important to study fast dynamic phenomena in DD wind turbines because of the power electronics. This can be accomplished through transient models based on either abc or dq0 quantities as shown in [78]. There are only a few references in literature regarding the simulation of an HTS machine during severe transient behavior. One such reference is in [79], where a three-phase short circuit is applied to the load side terminals of a step-up transformer connected to an HTS field coil synchronous machine. The HTS coil temperature are predicted using a FE (finite-element) quench model. In this case the fault currents are computed using a two-dimensional (2-D) finite-element electromagnetic model of the generator coupled to an external mechanical and electrical circuit in a commercial FE package. The transient FE analysis takes the current and magnetic field results from the system analysis as inputs and calculates the Joule heating, the temperature, and the resistance of the coil. However, the nonuniform distribution of the current density is not taken into account, so the impact of the magnetic flux density do not degradate the corresponding superconductor critical current in a "realistic" way. In [80], a three-phase short circuit is applied at stator terminals through a lumped-parameter dq0 SM model and by considering a negligible but constant HTS field resistance. Therefore, the transient dynamics of the superconductor are neglected. Another HTS SM dq0 model is used in [81] to simulate a severe fault condition, where the main goal is to determine a suitable stainless steel damper layer to protect the HTS field winding but the nonlinear behavior of the superconductor was also neglected. The same short circuit fault was simulated in [82] to identify the corresponding influence on the HTS field coil through the FEM but also without considering the HTS physical details. In [83], a series of short circuit tests were performed on a real air-core HTS rotor and a conventional stator. Those tests were unable to provide any evidence to show if a quench occurred in the HTS winding by heating due to a lack of suitable instrumentation. The temperature of the center coil was monitored, but the output signal of the thermometer experienced distortion due to inductive voltages caused by transients in the rotating machine. The DC power supply restrained the reaction in

the winding, made it challenging to examine the status of individual coils due to inductive transients. However, the measures of the field current indicate that the corresponding transient lasts longer than anticipated compared with a traditional machine. Finally, in [84], the field current in the HTS field winding of a wind-based SM under various short circuit scenarios was simulated. The study focused more on mechanical strains created by short circuit currents than on the dynamics of the superconductor. Still, the need for quantitative analysis of critical current was emphasized to prevent a quench in the SC field winding. Taking into account this background, the present thesis proposes a lumped-parameter model which considers relevant details of the physics of the superconductor by integrating an equivalent thermoelectric, magnetic and electrical circuits, which allows for building an equivalent nonlinear resistance of the HTS field winding at a reasonable computational speed. This nonlinear resistance is then incorporated into a 8th order dq0 model of a hybrid SM (SC rotor conventional stator) for analyzing power system transients. The subsequent chapter introduces the details of this model.

2.6   HTS-SM power converter modeling

Power electronic systems (PESs) are utilized to manage the electrical power flow within electrical networks comprised of an electrical energy source, a load, a power electronic circuit, and a control circuit (see Fig. 2.9). The power electronic circuit consists of electronic switching devices and passive components controlled by gating/switching signals and feedback signals [85]. The characteristics of such a circuit depend on the chosen electronic switching device. Switching devices can be categorized into different types: uncontrollable (power diodes), semicontrollable (thyristors and silicon-controlled rectifiers (SCRs)), and fully controllable (metal-oxide-semiconductor field-effect transistors (MOSFETs), Bipolar junction transistors (BJTs), insulated-gate bipolar transistors (IGBTs), gate-turn-off thyristors (GTOs), and integrated gate-commutated thyristors (IGCTs) [86, 87]. Furthermore, PESs may also be classified based on their corresponding electrical signal conversion processes, such as AC-to-DC, DC-to-AC, DC-to-DC, and AC-to-AC.

One of the most prevalent power conditioning converters for renewable energy applications is based on the voltage source converter (VSC) topology, in which the DC-side voltage circuit maintains a constant polarity, while the average power flow direction is determined by the polarity of the DC-side current. VSCs use fully controllable switching devices chosen by the application characteristics, such as rated power and frequency. Nonetheless, as the switching frequency grows, the commutation losses grow too. Therefore, a trade-off must be
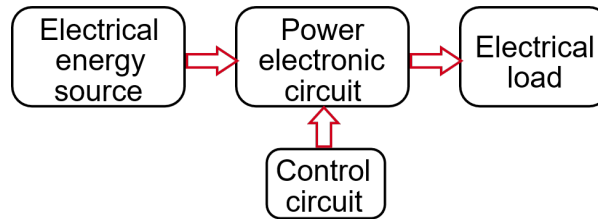
Fig. 2.9 Basic block diagram of a power electronic system

considered between losses and operating frequency to maintain the balance between cost, efficiency, and size for every particular renewable energy application.

High-power VSC behavior is typically simplified using straightforward switching models for power system studies and control design purposes to reduce the complexity of power electronics modeling and the computational burden in renewable energy source simulations. [88]. In this context, the present thesis aims to describe a suitable power converter model that can be readily coupled with the proposed thermoelectromagnetic HTS field coil SM model. However, the control tuning design for such a superconducting system is beyond the scope of the present thesis and will be addressed in a forthcoming work. The PES needed by the proposed HTS-SM is based on a variable-frequency power converter for direct-drive horizontal-axis wind turbine systems [89, 90]. The converter decouples the wind turbine electrical generator from the power grid using a controlled DC-link capacitor and two power transistor-based VSCs (back-to-back configuration). One VSC is connected to the generator terminals, while the other is connected to the power grid through a coupling impedance, as illustrated in the diagram of Fig. 2.10. Both VSCs are connected to the DC-link capacitor.
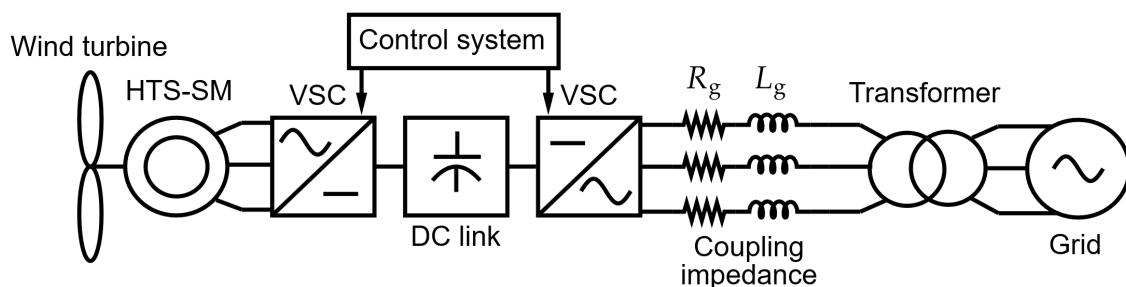
Fig. 2.10 Direct-drive horizontal-axis grid-connected wind turbine system diagram

The input mechanical power determines the generator-side converter terminal voltages $V_{s,abc}$, which control the machine output electrical power. The power is then rectified and delivered to the DC-link capacitor, whose voltage V_{DC} serves as a reference to control the grid-side converter terminal voltages $V_{g,abc}$, establishing a power flow between them. Furthermore, a maximum wind power extraction is possible when the machine speed is regulated to its optimal value based on a maximum power point tracking (MPPT) algorithm. A deeper understanding of such a system can be found in [89, 91].

2.6.1   VSC modeling framework

A back-to-back power converter topology consists of a pair of two-level, three-phase VSC converters with 3 pairs of IGBT-diode as shown in Fig. 2.11. The converter model is simplified for power system studies by neglecting electronic switching. Therefore, an average model sampled with a sinusoidal pulse-width modulation (PWM) signal with a high frequency modulation ratio m_f is usually assumed. The frequency of the carrier signal f_{ref} is greater than the reference voltage signal frequency f_c, i.e., $f_{ref} \gg f_c$.
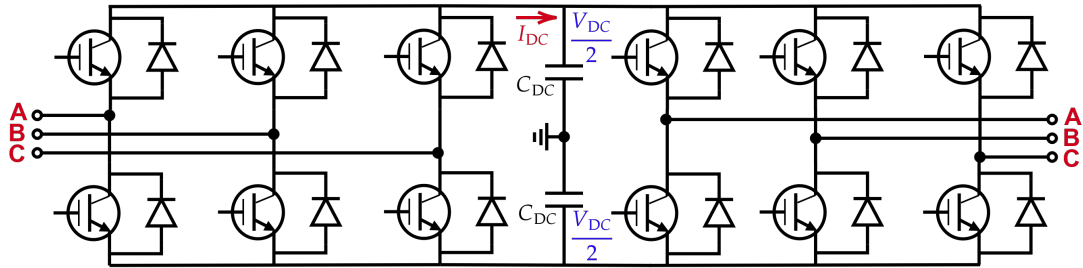
Fig. 2.11 Back-to-back power converter diagram

The DC link is modeled by two DC voltage sources of $V_{DC}/2$. However, as a simplified averaged power converter model is chosen, the DC-link of Fig.2.11 can be modeled by only one equivalent capacitor C with the same value as the original model. The instantaneous VSC phase terminal voltage $V_{tr,j}$ are defined with respect to the sinusoidal modulation function m_j given in (2.11) and the DC-link voltage V_{DC} as follows,

$$V_{tr,j}(t) = \frac{1}{2}m_j \, V_{DC} \tag{2.10}$$

where the sinusoidal modulation function with peak magnitude of M_j, phase angle θ_j, and modulation angle θ_{m_j} is defined by,

$$m_j = \left|M_j\right| \cos\left(2\pi f_c\, t + \theta_j + \theta_{m_j}\right) \tag{2.11}$$

The DC currents leaving a common node between a pair of connected IGBT-diode are given by,

$$I_{j,DC} = \frac{1}{2}m_j\, i_j \tag{2.12}$$

where i_j represents the phase current flowing through the "j" VSC phase terminal.

The DC-link current corresponds to the sum of the rectified three-phase currents of (2.12), which yields ,

$$I_{DC} = \sum_{j=1}^{3} I_{i,DC} \tag{2.13}$$

As a result of (2.10), the VSC terminal voltages are controlled by adjusting the modulation functions while maintaining a suitable DC-link voltage. Thus, when the VSC is connected to a source or load, the associated currents described in (2.12) can be modified, altering the power flow into and out of the VSC system through the DC-link current given by (2.13).

Chapter 3

HTS synchronous machine modeling

3.1   Introduction

This chapter presents the modeling of a hybrid SM with a SC tape-wounded rotor and conventional stator. Its particularity, compared to a typical machine model, is found in the details of the thermoelectromagnetic behavior of the SC material. The superconductor resistance dependence on the magnetic flux density and the temperature is used to describe entirely this behavior. The HTS coil thermoelectromagnetic model is divided into three equivalent submodels: electrical, thermal, and magnetic. The former estimates the current distribution i_{sc} and i_{mt} between the superconductor and the metallic layers. The electrical model of the field coil, relies on series-connected equivalent parallel circuits. [32, 92, 93]. The coil temperature behavior $\mathbf{T}_{coil}$ is computed from the power losses $\mathbf{P}_l$ arising in each tape layer using an equivalent thermo-electrical circuit [30, 94, 95]. The remaining model estimates the machine flux distribution created by the current-carrying conductors through a magnetic equivalent circuit (MEC) knowing the flux lines given by a FEM [96, 97]. The magnetic FEM, relies on a classic 2D machine model with a moving mesh to simulate the rotor angular displacement θ_r. It serves three purposes: 1) to yield a fair distribution of the current density in the HTS winding during transients to estimate the magnitude of the magnetic flux density impacting the coil, 2) to provide the expected magnetic flux lines across the machine, easing the building of the MEC model, and 3) as a reference for the MEC validation. In this context, the complete SC field coil model, from which the equivalent resistance is obtained, is coupled to a classical dq0 SM model to simulate an HTS machine connected to the grid. The algorithm to compute the equivalent HTS field coil resistance R_{fd} and its coupling with the dq0 model for a given simulation time t_{stop} is presented in Fig. 3.1.

First, the parameters at steady-state are computed. Then, the electrical model estimates the current distribution in the field winding in order to compute the power losses and the mean value of the magnetic flux density $\bar{B}$ over the HTS coil. The equivalent resistance is then calculated and integrated to the SM model until the simulation stops. The next subsection introduces the machine topology before delving into the modeling details.
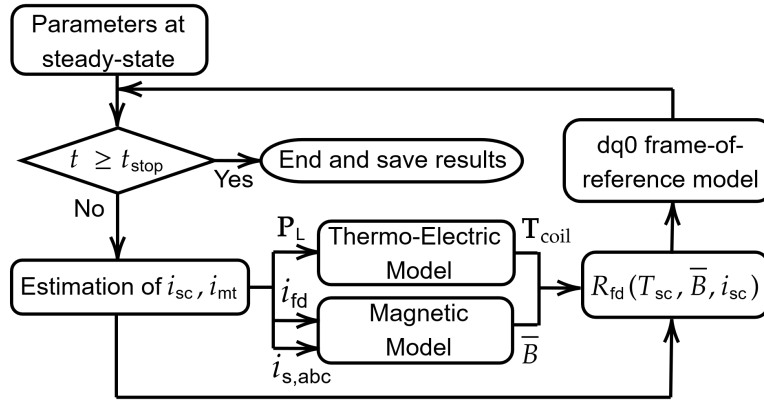
Fig. 3.1 Algorithm to compute the equivalent resistance of the HTS field coil and its coupling with the machine dq0 model.

3.2 Machine topology

The generator topology is based on a salient pole synchronous machine with p poles, with a conventional slotted stator and a warm-type wounded-rotor made of superconducting racetrack-shaped coils [56] for wind power applications. All racetrack coils, supplied with a DC current I_{fd}, are assumed to be wounded identically with N_{fd} turns and the same insulated commercial REBCO tape. The cooling system uses a modular structure as proposed in [98] so that each coil is conduction cooled through a stainless steel cooling plate connected to a pipe in which liquid nitrogen (LN2) flows at $T_{op} = 77$ K. The modular cryostat (MC) system is a cryogenically isolated system consisting of an outer box, a multilayer insulation chamber, a vacuum chamber, and an internal box. The outer box encloses all the sections and provides structural support. The multilayer insulation chamber and vacuum chamber isolate the system from the outside environment, while the internal box surrounds the LN2 cooling tube, cooling plate, and HTS field coil. The cooling plate gives extra thermal inertia to the MC system and mitigates the heat produced by the HTS field coil under a machine transient.
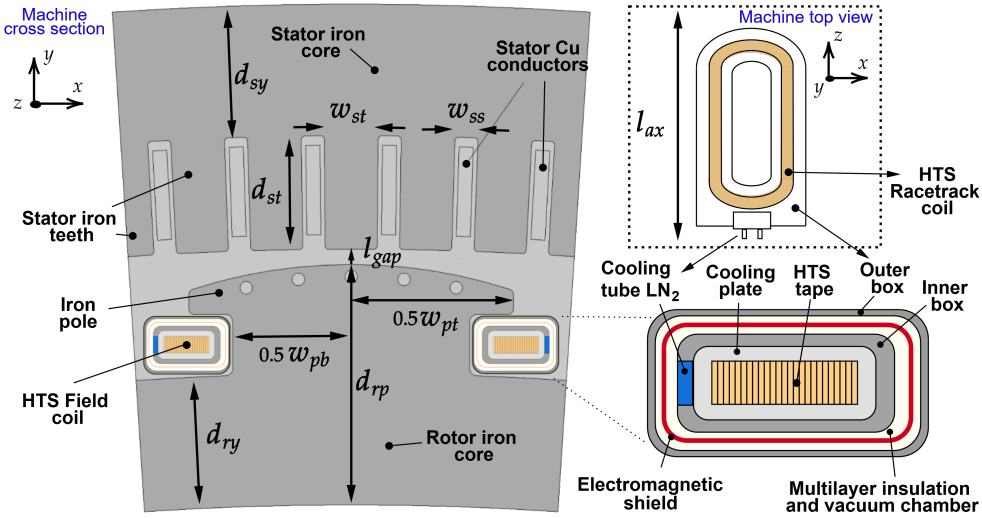
Fig. 3.2 HTS field coil synchronous machine topology. Concept and geometrical parameters.

Fig. 3.2 illustrates the cross-section of a machine pole section. The geometric parameters *l*, *d*, and *w* represent the length, the depth and the width, respectively, whereas the subscripts sy, st, pt, pb, ry, gap and ax, represent the stator iron core, the stator iron teeth, the pole tip, the pole body, the rotor iron core, the air gap, and the axial direction, respectively.

3.2.1 REBCO tape

A REBCO tape from Superpower Inc.® with thick copper stabilizers for electrical stability and mechanical robustness has been chosen. The tape comprises different layers of metallic, substrate and REBCO materials. The silver layers give electrical stability and allow a better current redistribution between the metallic layers and the HTS layer under transients. The substrate is made from Hastelloy®. The tape's parameters and their corresponding dimensions are summarized in Table 3.1.

Table 3.1 Structure and parameters of commercial REBCO tape (SCS12050) [99, 100].
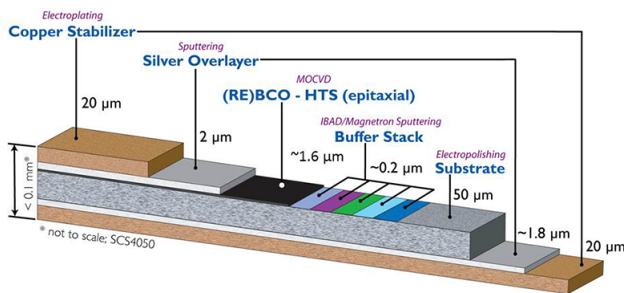
Parameters	Values
Critical current, I_{c0} (T_{op}, SF)	300 A
Reference n-value, n_0 (T_{op}, SF)	21
Critical temperature, T_c	92 K
Tape width, w_{tp}	12 mm
Tape thickness, t_{tp}	0.1 mm

3.3 HTS coil thermoelectromagnetic modeling

The Joule's dissipation and the magnetomotive force MMF are coupled with the thermo-electromagnetic model and fully built into the magnetic flux density-, temperature- and current-dependent resistance of the HTS field coil. In the present work, the critical current dependence on magnetic flux density is represented through the exponential model found in [35], which is focused solely on the magnitude of the magnetic flux density over the superconductor sample as follows,

$$I_{c,T}(\bar{B}) = \exp\left(-\frac{\bar{B}}{B_0}\right) \tag{3.1}$$

with B_0 as a constant fitting parameter [33], and $\bar{B}$ as the average magnetic flux density over the tape. The critical current behavior considering the thermal and magnetic dependence yields,

$$I_c(T_{sc}, B_{sc}) = \begin{cases} I_c(T_{ref}) \cdot \exp\left(-\dfrac{\bar{B}}{B_0}\right) & , T_{ref} \leq T_{sc} < T_{cs} \\[3mm] I_c(T_{ref}) \cdot \exp\left(-\dfrac{\bar{B}}{B_0}\right) \cdot \left(\dfrac{T_{sc} - T_c}{T_{ref} - T_c}\right) & , T_{cs} \leq T_{sc} < T_c \\[3mm] 0 & , T_{sc} \geq T_c \end{cases} \tag{3.2}$$

3.3.1 Electrical model

Each turn "k" (see Fig. 3.3) of the SC field coil is electrically modeled as a parallel circuit made of two resistances: the HTS layer nonlinear resistance $R_{sc,k}$ computed from (2.2), and the metallic layers' equivalent resistance $R_{mt,k}$ known as the matrix resistance. The equivalent matrix resistance per turn, composed of a number of metallic layers N_{mt} and their corresponding cross-section A_η, length l_η, and temperature-dependent resistivity ρ_η is given by,

$$\frac{1}{R_{mt,k}} = \sum_{\eta=1}^{N_{mt}} \frac{1}{\rho_\eta(T_\eta)} \frac{A_\eta}{l_\eta} \tag{3.3}$$
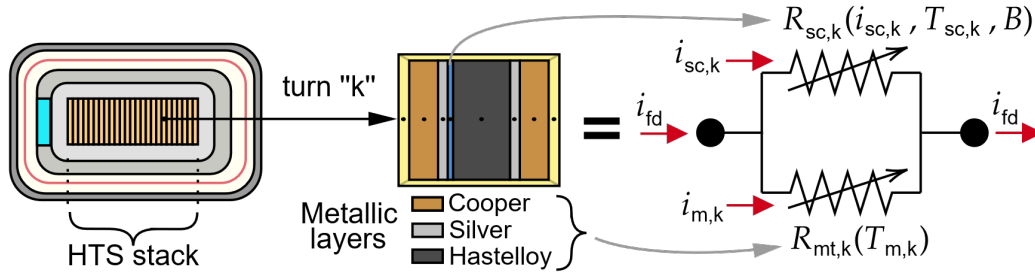
Fig. 3.3 Model of one turn of the full HTS field coil. Each turn connected in series carry I_{fd} current.

By expressing the resistance voltage drops of the matrix and the SC layer given in Fig. 3.3 through the Ohm's law, while rearranging the matrix current regarding the field and SC layer currents. The SC current $i_{sc,k}$ in the turn "k" is solved via the following polynomial,

$$i_{sc,k}^{n_k} + \frac{I_{c,k}^{n_k}}{V_{c,k}} R_{mt,k} \left(i_{sc,k} - i_{fd} \right) = 0 \tag{3.4}$$

Equation (3.4) is solved using the Newton-Raphson algorithm for every field coil turn. The current repartition between the matrix and the SC layer is obtained through Kirchhoff's current law. Therefore, the power losses P_l in every layer at every winding turn can be obtained through Joule's law as,

$$P_{lsc,k} = R_{sc,k} i_{sc,k}^2, \qquad P_{l\eta,k} = R_{\eta,k} i_{\eta,k}^2 \tag{3.5}$$

where $i_{\eta,k}$ is the current flowing through a specific metallic layer, computed by the current divisor $i_{\eta,k} = \left(R_{mt,k}/R_{\eta,k} \right) i_{m,k}$.

Finally, by assuming every rotor pole has the same electrical behavior, and wound with the same number of turns per pole $N_{fd,p} = N_{fd}/p$, the series-connected HTS field coil resistance is computed via (2.2) and (3.3) as follows,

$$R_{fd} = p \sum_{k=1}^{N_{fd,p}} \left[\frac{R_{sc,k} R_{mt,k}}{R_{sc,k} + R_{mt,k}} \right] \tag{3.6}$$

with "k" representing a given turn.

3.3.2   Thermal model

The thermal model is based on a nodal approach for which the heat flows from the HTS stack to the heat sink via a discretized network of thermal conductances and thermal capacitances. The schematic drawing in Fig. 3.5 illustrates the fundamental heat flow path within the MC and the temperature nodes from which the thermal model is constructed. The temperature distribution is solved over time via an explicit scheme, associating one temperature node per tape layer, one node to the insulation between tapes, one node to the insulation between tapes and cooling plate, 4 cardinal nodes for the cooling plate and one node for the cooling tube with LN2. The assumptions are listed below:

1. The MC system is modeled as an adiabatic process. The vacuum chamber and multi-layer insulation chamber isolate the system from the environment, so there is no heat transfer between the system and the exterior.

2. The heat capacity $c_{\mathrm{p}}^{\mathrm{th}}$ and the thermal conductivity k^{th} of the cooling plate, and all the coil layers are a function of temperature (see Appendix A).

3. The local temperature of materials is uniformly distributed across each layer of the tape.

4. Heat flux is assumed to be propagated in the x and y directions. There is no conduction along the z axis

5. The convection coefficient h_{conv} illustrated in Fig. 3.4 characterizes the heat transfer between a solid and the moving LN2 [30].
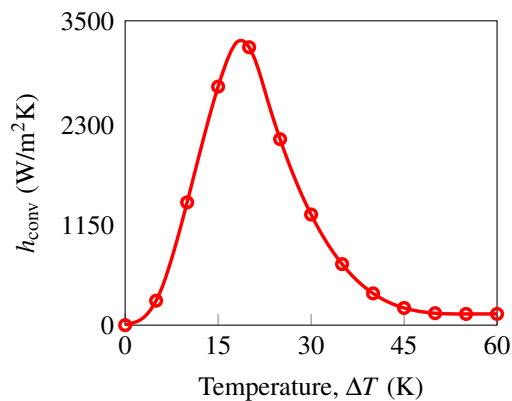
Fig. 3.4 Convection coefficient curve
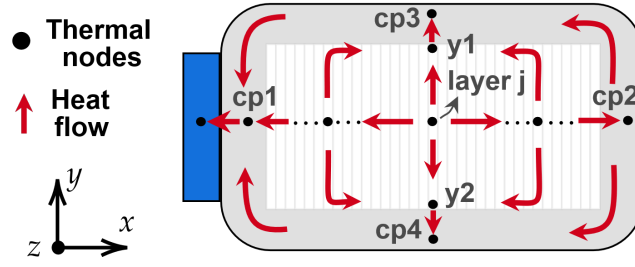
Fig. 3.5 Diagram of heat flow path within the modular cryostat.

The Fourier's law which describes the conduction of heat through a solid in the x and y directions can be splitted as follows,

$$Q_x = -k^{\text{th}} A_{yz} \frac{\partial T}{\partial x}, \qquad Q_y = -k^{\text{th}} A_{xz} \frac{\partial T}{\partial y} \tag{3.7}$$

where A_{yz} and A_{xz} are the cross-sectional areas in the planes yz and xz, respectively, and represent two isothermal surfaces from which the heat flow Q enters and leaves perpendicularly, as illustrated in Fig. 3.6. Linearizing the temperature gradients in (3.7) yields the relation $Q_x = G_x^{\text{th}} \Delta T$ and $Q_y = G_y^{\text{th}} \Delta T$, where $G_{x,y}^{\text{th}}$ are the thermal conductances of material "j" in the x and y directions defined as follows,

$$G_{j,x}^{\text{th}} = k_j^{\text{th}}(T_j) \frac{A_{j,yz}}{l_{j,x}}, \qquad G_{j,y}^{\text{th}} = k_j^{\text{th}}(T_j) \frac{A_{j,xz}}{l_{j,y}} \tag{3.8}$$

where T_j, $l_{j,x}$, $l_{j,y}$ and k_j^{th} are the temperature, the thickness, the width and the thermal conductivity of the material "j". The thermal resistances $R_{j,x}^{\text{th}}$ and $R_{j,y}^{\text{th}}$ defined in Fig. 3.6 correspond to the reciprocal of (3.8), respectively.

(a) Heat transfer in x axis.

(b) Heat transfer in y axis.
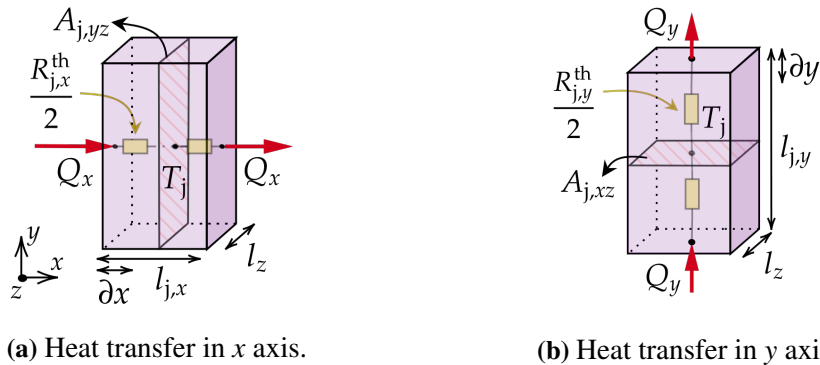
Fig. 3.6 Schematic diagram of the unidimensional heat transfer in solids over x and y axis.

The convection heat transfer is described through a thermal conductance given by,

$$G^{\text{th}}_{\text{conv}} = h_{\text{conv}}(\Delta T)A_{\text{conv}} \tag{3.9}$$

where ΔT and A_{conv} are the temperature difference and the contact surface area between the corresponding solid and the LN2 cooling tube, respectively. The evolution of h_{conv} as a function of ΔT is given in Fig. 3.4. The power change in a material "j" caused by heat transfer and heat generation, is given by

$$m_{\text{j}}c^{\text{th}}_{\text{p,j}}\frac{\mathrm{d}T_{\text{j}}}{\mathrm{d}t} = Q_{\text{in}} - Q_{\text{out}} + P_{l,\text{j}} \tag{3.10}$$

where Q_{in}, Q_{out} and P_l are the heat flux entering and leaving from the material, and the heat generation due to Joule's heating, respectively. The term $m_{\text{j}}c^{\text{th}}_{\text{p,j}}$ represents the capacity to store energy given a temperature increment. This parameter may be analogous to the capacitance in an electric circuit, so the thermal capacitance C^{th}_{j} may be given by,

$$C^{\text{th}}_{\text{j}} = m_{\text{j}}c^{\text{th}}_{\text{p,j}} = \text{Vol}_{\text{j}}\zeta_{\text{j}}c^{\text{th}}_{\text{p,j}} \tag{3.11}$$

where Vol_{j}, ζ_{j} and $c^{\text{th}}_{\text{p,j}}$ are the material volume, density and temperature-dependent specific heat, respectively. A discretized expression for a material "j", from which the temperature value at a step time $t + \Delta t$ is computed through the temperature value at current time t, is obtained with an explicit numerical method applied to (3.10) as follows,

$$\frac{C^{\text{th,t}}_{\text{j}}}{\Delta t}\left(T^{\text{t}+\Delta\text{t}}_{\text{j}} - T^{\text{t}}_{\text{j}}\right) = Q^{\text{t}+\Delta\text{t}}_{\text{in}} - Q^{\text{t}+\Delta\text{t}}_{\text{out}} + P^{\text{t}}_l \tag{3.12}$$

When examining expressions (3.7) to (3.12), it is observed that the relationships between temperature and heat flux are comparable to those between voltage and current.

Table 3.2 Analogies between thermal and electric circuit parameters.

Parameter	Symbol	Unit		Parameter	Symbol	Unit
Heat flux	Q	W	$\leftrightarrow$	Electrical current	i	A
Heat source	P_l	W	$\leftrightarrow$	Current source	i_{s}	A
Temperature	T	K	$\leftrightarrow$	Voltage	V	V
Thermal resistance	R^{th}	K/W	$\leftrightarrow$	Resistance	R	Ω
Thermal conductance	G^{th}	W/K	$\leftrightarrow$	Conductance	G	S
Thermal conductivity	k^{th}	W/Km	$\leftrightarrow$	Conductivity	σ	Sm
Thermal capacitance	C^{th}	J/K	$\leftrightarrow$	Capacitance	C	F
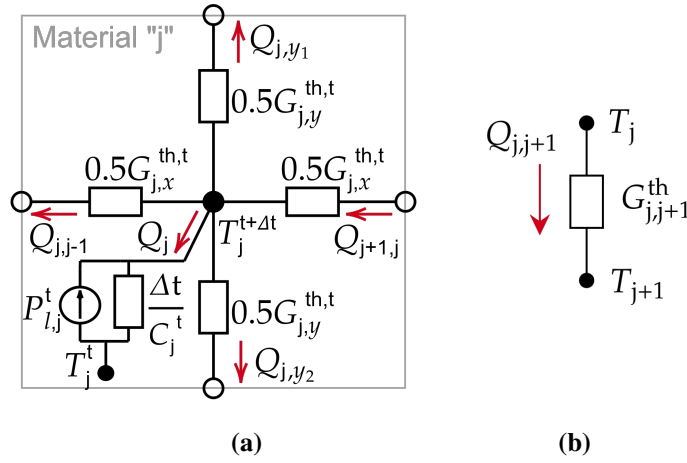
Fig. 3.7 Schematic diagram of the unidimensional heat transfer in solids over *x* and *y* axis.

Table. 3.2 presents an analogy between electric and thermal circuits that is used to construct the modular cryostat equivalent thermo-electric network of the proposed HTS machine. This network consists of temperature nodes, thermal conductances, thermal capacitances, and heating sources. For this purpose, the primitive circuit in Fig. 3.7a can be used as an stencil to model any given layer or material "j" under certain assumptions: 1) The upper and bottom nodes corresponding to the insulation between the tapes and the cooling plate do not present heat flux in the *x* direction. 2) The cooling plate enveloped by the MC internal box, the vacuum chamber and the multilayer insulation chamber represents an adiabatic boundary for the system. Moreover, only one cooling plate node is linked to the cooling tube, where heat is transmitted through convection. This link is built through the convection conductance of (3.9). In agreement with Fig. 3.7a, whether in the *x* or *y* directions, the nodal connection between two adjacent materials (for instance, "j" and "j+1") consists of two series-connected thermal conductances simplified into one, as follows,

$$G_{j,j+1}^{th} = 2 \left(\frac{1}{G_j^{th}} + \frac{1}{G_{j+1}^{th}} \right) \tag{3.13}$$

Based on Fig. 3.7b, the heat flux passing through the thermal conductance, given by the above expression, can be represented as follows,

$$Q_{j,j+1} = G_{j,j+1}^{th} \left(T_j - T_{j+1} \right) \tag{3.14}$$

The overall thermal model is established by substituing (3.13) and (3.14) into (3.12), which express the heat fluxes entering and leaving node "j" in terms of thermal conductances and temperatures.
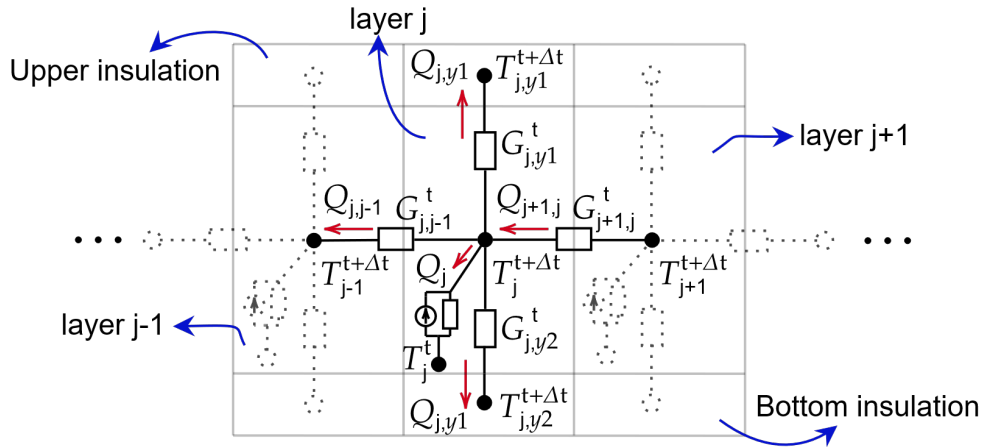
Fig. 3.8 REBCO tape thermal model.

Each field coil turn consists of eight layers, including the insulation at both ends. Therefore, the circuit stencil of Fig. 3.7a is repeated and properly connected side by side $v = N_{\text{fd,p}} \times 8$ times in the x direction to build the HTS field coil thermal model. The Fig. 3.8 illustrates the nodal connection between one tape's layer "j" and its adjacent layers "j-1","j+1","y1" and "y2". The insulation layers enveloping the HTS stack correspond to the interface at which the heat flows between the HTS field coil and the cooling plate. In Fig.3.5, the nodes "cp1" and "cp2" are connected to layers "1" and "v", respectively. Meanwhile, the nodes "cp3" and "cp4" are connected to the upper and bottom insulation nodes "y1" and "y2", which represent an equivalent insulation layer conformed by all the insulation layers of the HTS stack in the y direction. The thermal circuit corresponding to the upper and bottom insulation are presented in Fig. 3.9, while the thermal circuit for the cooling plate is illustrated in Fig. 3.10.
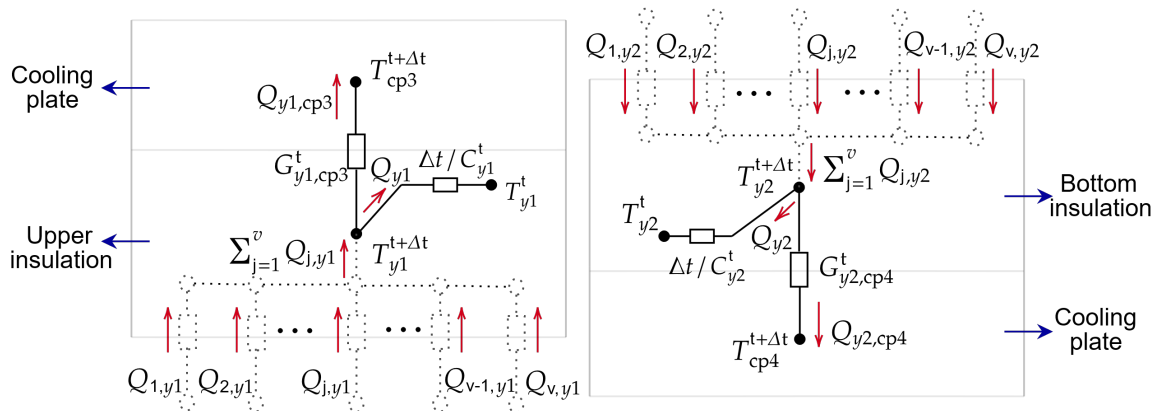
Fig. 3.9 Upper and bottom insulation thermo-electric circuit model.
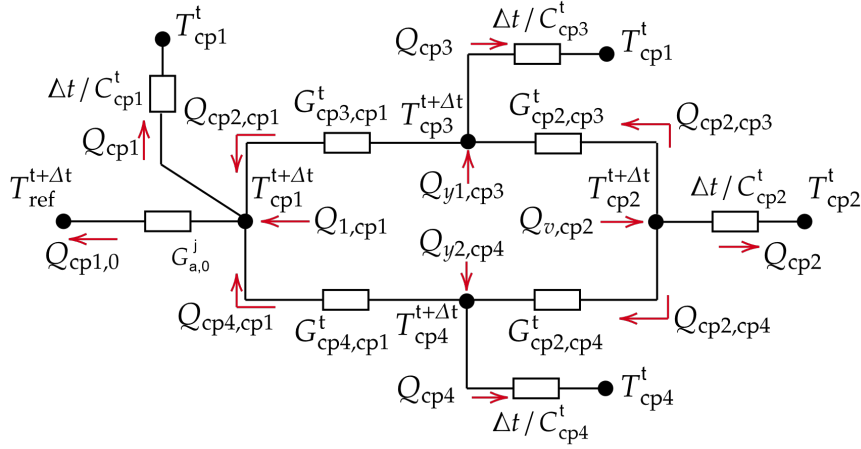
Fig. 3.10 Cooling plate thermo-electric circuit model.

The nodal analysis is used to formulate the thermal system of equations from the complete thermo-electric circuit built by combining Fig. 3.8 to Fig. 3.10. Then, by rearranging and representing (3.12) in a matricial form, the resultant expression is given by,

$$\mathbf{T}^{t+\Delta t} = \left(\frac{1}{\Delta t} \mathbf{C}^{th,t} + \mathbf{G}^{th,t} \right)^{-1} \cdot \left(\frac{1}{\Delta t} \mathbf{C}^{th,t} \mathbf{T}^{t} + \mathbf{T}_{op} \mathbf{G}_{bd}^{th,t} + \mathbf{P}_{tp}^{t} \right) \tag{3.15}$$

where $\mathbf{T}^{t}$, $\mathbf{T}^{t+\Delta t}$ and $\mathbf{T}_{op}$ are the vectors of temperature at time t and $t + \Delta t$, and at the boundary nodes, given from (3.16) to (3.18); $\mathbf{G}_{bd}^{th,t}$ is the boundary convective thermal conductance connecting one node of the cooling plate to the LN2, defined by (3.19); $\mathbf{G}^{th,t}$ is the matrix of thermal conductances connecting one node to the next given from (3.20) to (3.23); C is the matrix of thermal capacitances shown in (3.25); $\mathbf{P}_{tp}^{t}$ is the power dissipated in each layer of the tape.

$$\mathbf{T}_{coil}^{t} = \begin{bmatrix} T_{cp1}^{t}, & \cdots, & T_{cp4}^{t}, & T_{1}^{t}, & T_{2}^{t}, & T_{3}^{t}, & \cdots, & T_{v}^{t}, & T_{y1}^{t}, & T_{y2}^{t} \end{bmatrix}^{T} \tag{3.16}$$

$$\mathbf{T}_{coil}^{t+\Delta t} = \begin{bmatrix} T_{cp1}^{t+\Delta t}, & \cdots, & T_{cp4}^{t+\Delta t}, T_{1}^{t+\Delta t}, T_{2}^{t+\Delta t}, T_{3}^{t+\Delta t}, & \cdots, & T_{v}^{t+\Delta t}, T_{y1}^{t+\Delta t}, T_{y2}^{t+\Delta t} \end{bmatrix}^{T} \tag{3.17}$$

$$\mathbf{T}_{op} = \begin{bmatrix} T_{ref}, & \cdots, & 0, & 0, & 0, & 0, & \cdots, & 0, & 0, & 0 \end{bmatrix}^{T} \tag{3.18}$$

$$\mathbf{G}_{bd} = \begin{bmatrix} G_{cp,ref}, \cdots, & 0, & 0, & 0, & 0, & \cdots, & 0, & 0, & 0 \end{bmatrix}^{T} \tag{3.19}$$

$$\mathbf{G}^{th,t} = \left[\begin{array}{c|c} \mathbf{G}_{coil}^{th,t} & \mathbf{G}_{coil,cp}^{th,t} \\ \hline \mathbf{G}_{cp,coil}^{th,t} & \mathbf{G}_{cp}^{th,t} \end{array} \right] \tag{3.20}$$

$$
\mathbf{G}_{cp}^{th,t} = \begin{bmatrix} G_{cp1,cp1}^{th,t} & 0 & G_{cp1,cp3}^{th,t} & G_{cp1,cp4}^{th,t} \\ 0 & G_{cp2,cp2}^{th,t} & G_{cp2,cp3}^{th,t} & G_{cp2,cp4}^{th,t} \\ G_{cp3,cp1}^{th,t} & G_{cp3,cp2}^{th,t} & G_{cp3,cp3}^{th,t} & 0 \\ G_{cp4,cp1}^{th,t} & G_{cp4,cp2}^{th,t} & 0 & G_{cp4,cp4}^{th,t} \end{bmatrix}
\tag{3.21}
$$

$$
\mathbf{G}_{coil}^{th,t} = \begin{bmatrix} G_{1,1}^{th,t} & G_{1,2}^{th,t} & 0 & \cdots & 0 & G_{1,y1}^{th,t} & G_{1,y2}^{th,t} \\ G_{2,1}^{th,t} & G_{2,2}^{th,t} & G_{2,3}^{th,t} & \cdots & 0 & G_{2,y1}^{th,t} & G_{2,y2}^{th,t} \\ 0 & G_{3,2}^{th,t} & G_{3,3}^{th,t} & \cdots & 0 & G_{3,y1}^{th,t} & G_{3,y2}^{th,t} \\ \vdots & \vdots & \vdots & \ddots & \vdots & \vdots & \vdots \\ 0 & 0 & 0 & \cdots & G_{v,v}^{th,t} & G_{v,y1}^{th,t} & G_{v,y2}^{th,t} \\ G_{y1,1}^{th,t} & G_{y1,2}^{th,t} & G_{y1,3}^{th,t} & \cdots & G_{y1,v}^{th,t} & G_{y1,y1}^{th,t} & 0 \\ G_{y2,1}^{th,t} & G_{y2,2}^{th,t} & G_{y2,3}^{th,t} & \cdots & G_{y2,v}^{th,t} & 0 & G_{y2,y2}^{th,t} \end{bmatrix}
\tag{3.22}
$$

$$
\mathbf{G}_{cp,coil}^{th,t} = \begin{bmatrix} G_{cp1,1}^{th,t} & 0 & 0 & \cdots & 0 & 0 & 0 \\ 0 & 0 & 0 & \cdots & G_{cp2,v}^{th,t} & 0 & 0 \\ 0 & 0 & 0 & \cdots & 0 & G_{cp3,y1}^{th,t} & 0 \\ 0 & 0 & 0 & \cdots & 0 & 0 & G_{cp4,y2}^{th,t} \end{bmatrix}
\tag{3.23}
$$

$$
\mathbf{G}_{coil,cp}^{th,t} = \left[\mathbf{G}_{cp,coil}^{th,t}\right]^{T}
\tag{3.24}
$$

$$
\mathbf{C}_{coil}^{th,t} = \begin{bmatrix} C_{cp1}^{th,t} & \cdots & 0 & 0 & 0 & 0 & 0 & 0 & 0 & 0 \\ \vdots & \ddots & \vdots & 0 & 0 & 0 & 0 & 0 & 0 & 0 \\ 0 & 0 & C_{cp4}^{th,t} & 0 & 0 & 0 & 0 & 0 & 0 & 0 \\ 0 & 0 & 0 & C_{1}^{th,t} & 0 & 0 & \cdots & 0 & 0 & 0 \\ 0 & 0 & 0 & 0 & C_{2}^{th,t} & 0 & \cdots & 0 & 0 & 0 \\ 0 & 0 & 0 & 0 & 0 & C_{3}^{th,t} & \cdots & 0 & 0 & 0 \\ \vdots & \vdots & \vdots & \vdots & \vdots & \vdots & \ddots & \vdots & \vdots & \vdots \\ 0 & 0 & 0 & 0 & 0 & 0 & \cdots & C_{v}^{th,t} & 0 & 0 \\ 0 & 0 & 0 & 0 & 0 & 0 & \cdots & 0 & C_{y1}^{th,t} & 0 \\ 0 & 0 & 0 & 0 & 0 & 0 & \cdots & 0 & 0 & C_{y2}^{th,t} \end{bmatrix}
\tag{3.25}
$$

3.3.3   Magnetic model

The magnetic flux lines distribution in a synchronous machine, obtained from the solution of a magnetic FEM, defines the basis for developing a MEC model built by a reluctance network to estimate the magnetic flux density affecting the SC electromagnetic state. The assumptions taken into account for building the MEC are the following: 1) The direction of the flux in each reluctance element is known a priori, 2) Only the fundamental component of the magnetic flux is considered in the analysis, 3) The magnetic hysteresis is neglected, 4) The mesh-based machine MEC is static and do not consider the machine rotation. The MEC model is based ont the Ampere's law and magnetic field Gauss's law, which can be directly analogous to Kirchhoff's voltage and current laws applied to magnetic systems under certain assumptions. The Ampere's law describes the line integral of the field intensity $\mathbf{H}$ over a closed path l_Γ as the total enclosed ampere-turns i_T by that path. In other words, the sum of every MMF drop F_{mm}^d over a closed loop equals the sum of every MMF source F_{mm}^s within the closed path. The integral form of the Ampere's law considering the closed path given in Fig. 3.11 is defined as follows,

$$\oint_{l_\Gamma} \mathbf{H} \cdot d\mathbf{l} = \int_{a_0}^{a_1} \mathbf{H} \cdot d\mathbf{l} + \int_{a_1}^{a_2} \mathbf{H} \cdot d\mathbf{l} + \cdots + \int_{a_{n-1}}^{a_n} \mathbf{H} \cdot d\mathbf{l} = i_T \tag{3.26}$$

where a_j represents the nodes of the section "j" on the closed trajectory. The enclosed ampere-turns are the sum of any current-carrying winding within the closed path defined by,

$$i_T = \sum F_{mm,j}^s = \sum N_j i_j \tag{3.27}$$

where N_j represents the number of turns of the "j" winding and i_j is its corresponding current. Assuming that the magnetic field $\mathbf{H}$ is uniform along the closed trajectory, the MMF drop $F_{m,j}^d$ in any section "j" can be obtained based on (3.26) as follows,

$$F_{m,j}^d = \int_{a_{j-1}}^{a_j} \mathbf{H} \cdot d\mathbf{l} \simeq H_j l_j \tag{3.28}$$

where H_j and l_j are the magnetic field intensity and the length of the section "j" on the closed trajectory, respectively. The Kirchhoff's voltage law (KVL) for magnetic systems may be defined by substituing (3.27) and (3.28) in (3.26) to obtain :

$$\sum F_{mm,j}^d - \sum F_{mm,j}^s = 0 \tag{3.29}$$
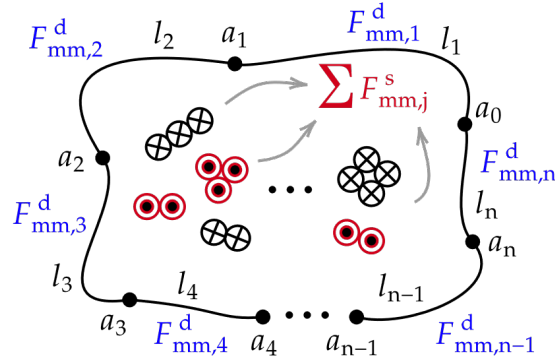
Fig. 3.11 Diagram of a closed magnetic path with current-carrying coils.

The magnetic Gauss's law states that the integration of the magnetic flux density in a closed surface A_Γ is zero, i.e., the flux entering over a closed surface is the same flux leaving from it (see Fig. 3.12). As the closed surface is conformed by "j" open surfaces, the corresponding expression yields,

$$\oint_{A_\Gamma} \mathbf{B} \cdot \mathbf{n} dA = \sum_j \int_{A_j} \mathbf{B} \cdot \mathbf{n} dA = 0 \qquad (3.30)$$

The magnetic flux density over an open surface is defined as the magnetic flux ϕ_m given by,

$$\phi_m = \int_A \mathbf{B} \cdot \mathbf{n} dA \qquad (3.31)$$

Substitution of (B.2) in (3.30) states the flux conservation which corresponds to Kirchhoff's current law (KCL) for magnetic systems, as,

$$\sum_j \phi_{m,j} = 0 \qquad (3.32)$$

The magnetic flux trajectories of a SM are modelled through a series of magnetic flux tubes that meet the laws given in (3.29) and (3.32). The flux lines penetrating a flux tube are always assumed perpendicular to their bases and never leak from their longitudinal direction. The flux tube bases are considered as volumes with small enough thickness to represent equipotential planes where the MMF drop between any point is negligible, known as magnetic nodes [106, 107]. Additionally, to represent the flux tube MMF drop given by (3.28), an analogy with electric circuits is used, yielding the magnetic scalar potential difference between two arbitrary and consecutive magnetic nodes "a" and "b" as $U_a - U_b$. The simplest magnetic flux tube presents a constant length l and cross section A, as shown in the closed surface given in Fig. 3.12.
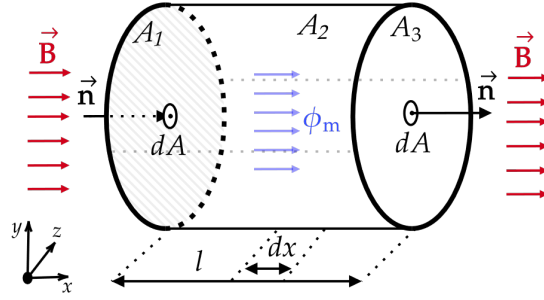
Fig. 3.12 Conservation of the magnetic flux density.

However, as the MEC flux tubes are fitted to the machine elements, the area, the length, the material property, or even part of the enclosed current may vary between magnetic nodes. For this reason, general expressions are defined in (3.33) to describe the flux tubes in terms of lumped parameters, i.e., in terms of reluctance R_m or permeance P_m, which are reciprocal ($R_m=1/P_m$). Nevertheless, if the flux tube geometry varies between their nodes, it could be easier to model a reluctance rather than a permeance or vice versa. The reluctance is commonly obtained when the flux tube presents a varying area, as shown in Fig. 3.13a, while the permeance is convenient when the variation is defined by the flux tube length, as given in Fig. 3.13b [106]. The magnetic permeability in (3.33) is stated as a function of the corresponding spatial coordinate due to the variation of the flux tube areas presented in Fig. 3.13. The construction of the MEC, composed of reluctances (or permeances, related to their MMF drops) and MMF sources, can be treated with the same rules as an electrical circuit. Indeed, the analogy between the MEC and electric circuit variables are presented in Table. 3.3. The set of equations describing the magnetic system can be solved using circuit analysis techniques such as nodal or mesh analysis.

$$R_m = \int \frac{1}{\mu(x)A(x)}\mathrm{d}x \qquad \Leftrightarrow \qquad P_m = \int \frac{\mu(x,y)}{l(x,y)}\mathrm{d}A \qquad (3.33)$$

Table 3.3 Analogies between magnetic and electric circuit parameters.

Parameter	Symbol	Unit		Parameter	Symbol	Unit
Magnetic flux	ϕ_m	Wb	$\leftrightarrow$	Electrical current	i	A
Magnetomotive force	F_{mm}	A-t	$\leftrightarrow$	Voltage	V	V
Magnetic scalar potential	U_a	A-t	$\leftrightarrow$	Electric scalar potential	V_a	V
Reluctance	R_m	H^{-1}	$\leftrightarrow$	Resistance	R	Ω
Permeance	P_m	H	$\leftrightarrow$	Conductance	G	S
Magnetic permeability	μ	Hm^{-1}	$\leftrightarrow$	Conductivity	σ	Sm

(a) Varying area flux tube

(b) Varying length flux tube
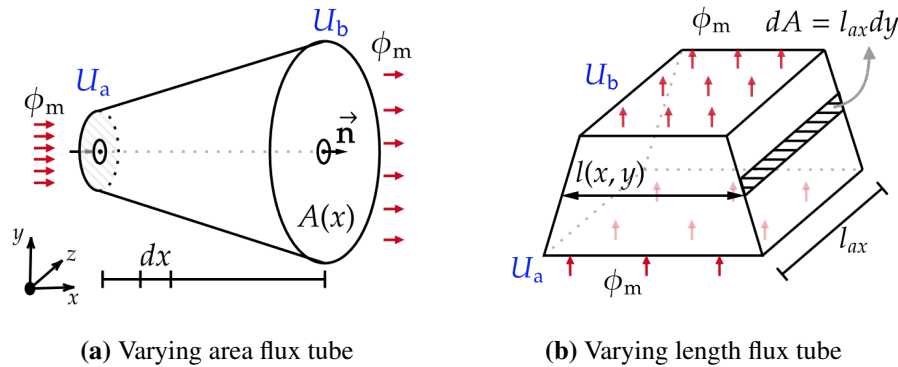
Fig. 3.13 Magnetic flux tube geometries typical for an electrical machine's MEC.

A ramped field current flowing in the HTS stack from a zero value to three times the tape critical current ($3I_c = 900$ A) is imposed in a FEM to induce a non-uniform distribution of current density in the HTS tapes simulating screening currents that arise during transients, as illustrated in Fig 3.14. The FEM provides information on the magnitude and distribution of magnetic flux density resulting from the non-uniform distribution of current density that serves as a basis for modeling the corresponding reluctance circuit. Due to the transient nature of the field current, two fronts of current (red color in Fig. 3.15), an upper ("u") and a lower ("l") front, are induced in the superconductor layer as the superconductor attempts to block out the penetration of the magnetic field. The closer the field current is to the critical current, the more uniform and wider both fronts become as shown by Fig. 3.15. Additionally, an asymmetry on the fronts, in the distribution of current density and magnetic field, is created due to the proximity of the iron pole on two sides of the coil.

(a)

(b)
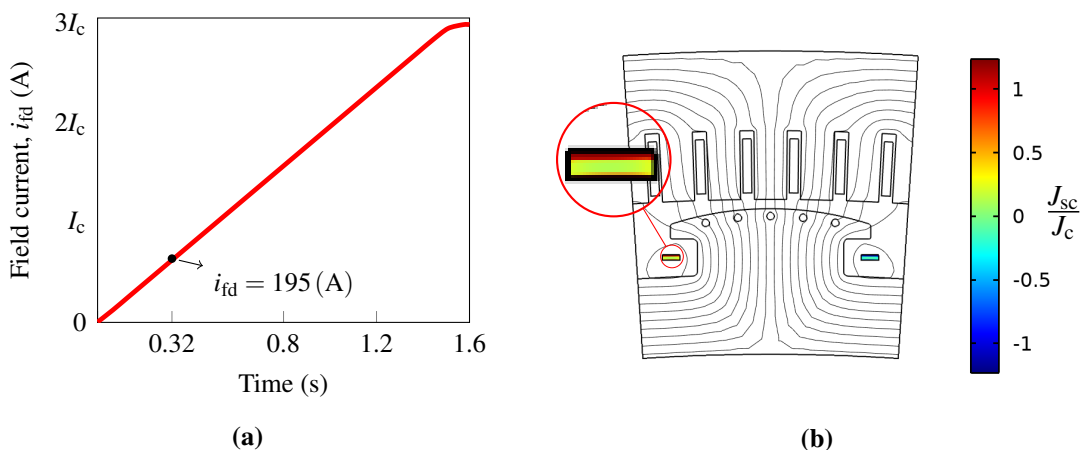
Fig. 3.14 (a) Transport current vs time simulation. (b) Magnetic flux distribution on a machine pole section and the normalized current density distribution in the HTS stack at $i_{fd} = 195$ A and $\theta_r = 0$.

(a) $i_{\text{fd}} = 115$ (A)

(b) $i_{\text{fd}} = 215$ (A)

(c) $i_{\text{fd}} = 274$ (A)

(d) $i_{\text{fd}} = 353$ (A)
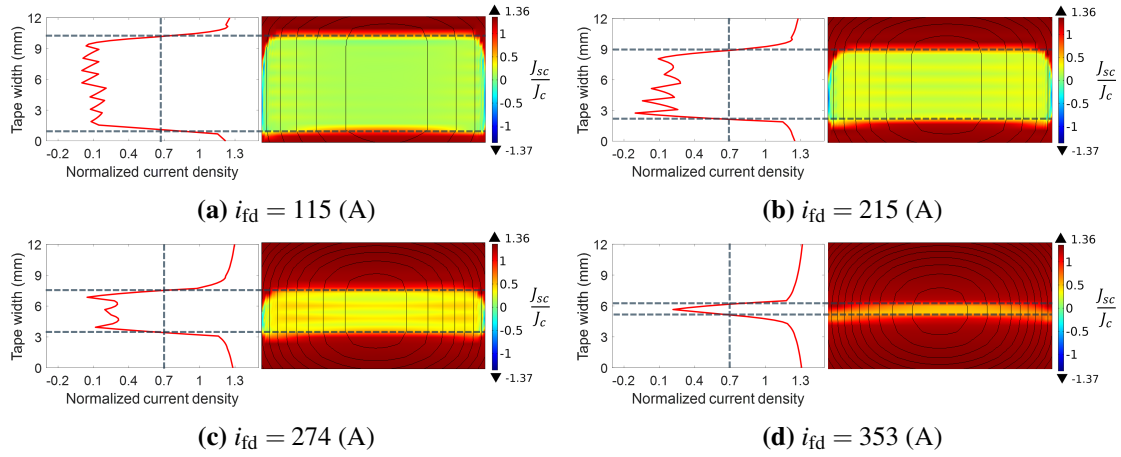
Fig. 3.15 Changes of the magnetic flux distribution due to the current density within the HTS coil for different values of the ramped field current.

The position of the fronts of current are defined by two front functions k_u and k_l given by,

$$k_u(i_{\text{fd}}) = 0.2750 \ \tanh\left(\frac{i_{\text{fd}} - 170}{180}\right) + 0.225 \tag{3.34}$$

$$k_l(i_{\text{fd}}) = 0.2540 \ \tanh\left(\frac{i_{\text{fd}} - 230}{180}\right) + 0.246 \tag{3.35}$$

To define these fronts, the current density is plotted on a cut line passing along both front edges. The corresponding interpolated data are then processed in Matlab. The front edge is defined as the fraction of the tape width for which the normalized current density J_{sc}/J_c reaches 70%. The interpolated data and fits are shown in Fig. 3.16.

(a) Upper front function k_u

(b) Lower front function k_l
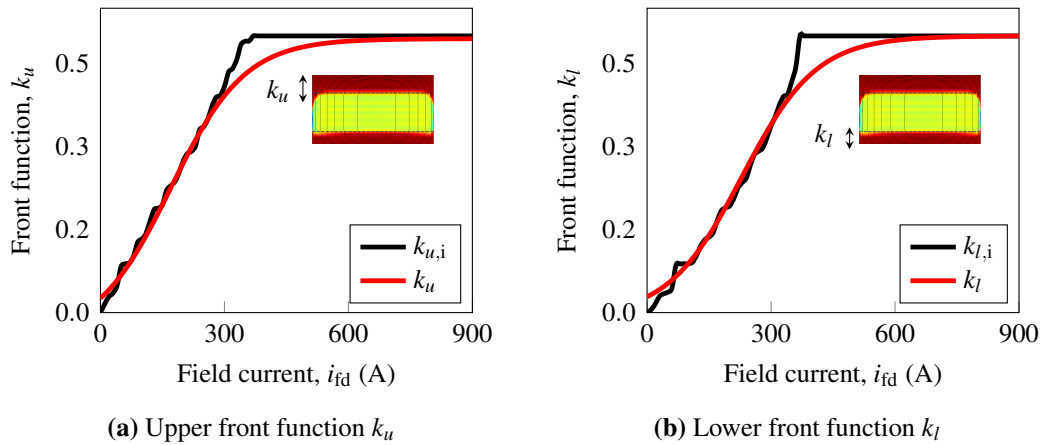
Fig. 3.16 Front functions: Interpolated data $k_{u,\text{i}}$ and $k_{l,\text{i}}$ and fitting curves k_u and k_l.

(a) Magnetic path

(b) Enclosed current density

(c) Reluctance circuit
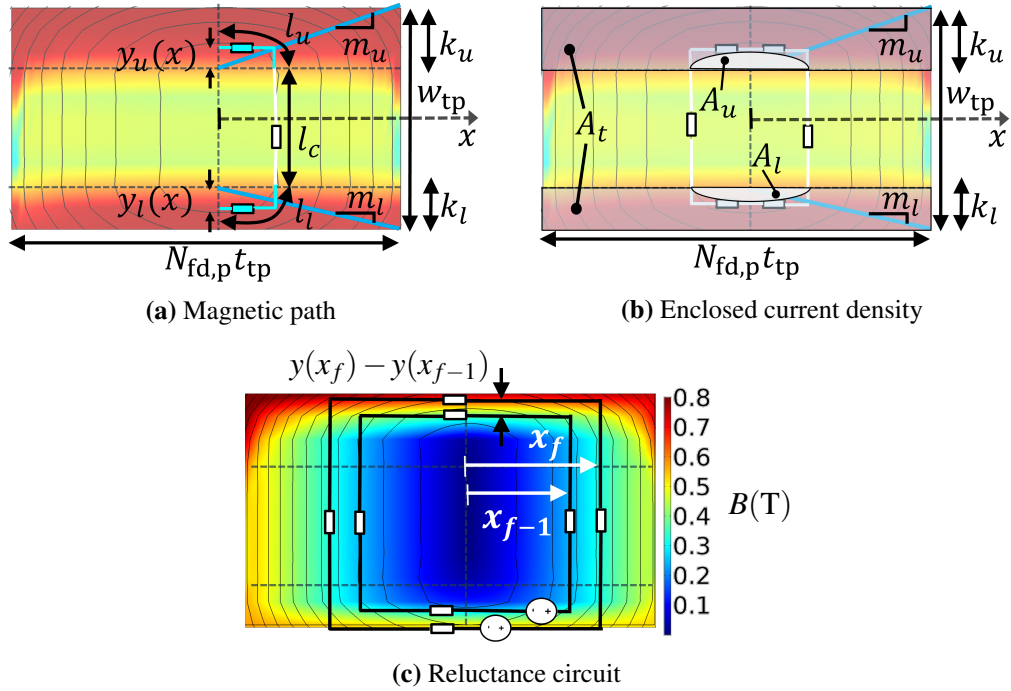
Fig. 3.17 MEC of the HTS field coil corresponding to a given distribution of current density. (a) Magnetic elliptic path, (b) cross-sectional areas corresponding to the current penetration. (c) reluctance circuit on top of the magnitude of the magnetic flux density computed with the FEM.

As shown in Fig. 3.17a, two HTS field coil MEC reluctances defined as R_{mu} and R_{ml} are related with the upper and lower fronts of current, while the third one defined as R_{mc} corresponds to the magnetic flux line between these two fronts of current. These reluctances are computed through (3.33) by assuming the magnetic permeability as $\mu = \mu_0$, and the following geometric parameters,

$$l_{\text{u,l}} = \frac{\pi}{4} x \left(1 + m_{\text{u,l}}\right) \left(1 + \frac{3\, h_{\text{u,l}}}{10 + \sqrt{4 - 3\, h_{\text{u,l}}}}\right), \qquad A_{\text{u,l}} = x\, m_{\text{u,l}}\, l_{\text{ax}},$$

$$l_{\text{c}} = 1 - k_{\text{u}}(i_{\text{fd}}) - k_{\text{l}}(i_{\text{fd}}), \qquad A_{\text{c}} = x\, l_{\text{ax}}$$

(3.36)

where x, w_{tp}, $N_{\text{fd,p}} t_{\text{tp}}$, $l_{\text{u,l}}$, $A_{\text{u,l}}$ and A_{c} are the displacement in the x direction from the coil center, the tape width, the coil length, the Ramanujan's formula for the ellipse length and the transverse areas (see Fig. 3.17b), respectively. $m_{\text{u,l}} = 2 k_{\text{u,l}} w_{\text{tp}} / \left(N_{\text{fd,p}} t_{\text{tp}}\right)$ is the slope of the line extending from the center of each front of current to their corresponding coil edge and $h_{\text{u,l}} = \left[\left(1 - m_{\text{u,l}}\right) / \left(1 + m_{\text{u,l}}\right)\right]^2$.

The MMF as a function of the x coordinate can be calculated by relating the "pseudo-elliptical" white-colored areas in Fig. 3.17b, corresponding to the enveloped portion of both fronts of current A_u and A_l, with the total area $A_t = w_{tp} N_{fd,p} t_{tp} (k_u + k_l)$.

In agreement with the Ampere's law, the mmf is then given by,

$$F_{mmf,x} = \frac{A_u + A_l}{A_t} N_{fd,p} \, i_{fd} \tag{3.37}$$

where the enclosed areas are $A_{u,l} = \frac{\pi}{2} x^2 m_{u,l}$. The magnetic flux at the position x is then inferred as,

$$\phi_x = \frac{F_{mm,x}}{2(R_{mc} + R_{mu} + R_{ml})} \tag{3.38}$$

As shown in Fig. 3.17c, the closest internal magnetic flux path to the coil surface is assumed to be responsible for the maximum penetration length of the field x_f. Using the field distribution computed by the FEM, the maximum value of the magnetic flux density perpendicular to the tape surface (the most stringent condition) is located around the top of the central turn. It is computed according to (3.38) as follows,

$$B_{sc} = \frac{d\phi}{dA} \approx \frac{\phi_{xf} - \phi_{xf-1}}{l_{ax} \left(y(x_f) - y(x_f - 1) \right)} \tag{3.39}$$

Various configurations of HTS stacks were simulated to determine the applicability of the proposed magnetic method. One such configuration, shown in Fig. 3.18, was simulated using the same field current ramp and methodology as in Fig. 3.15. A set of k_u and k_l as given by (3.34) and (3.35) should be computed for each stack.
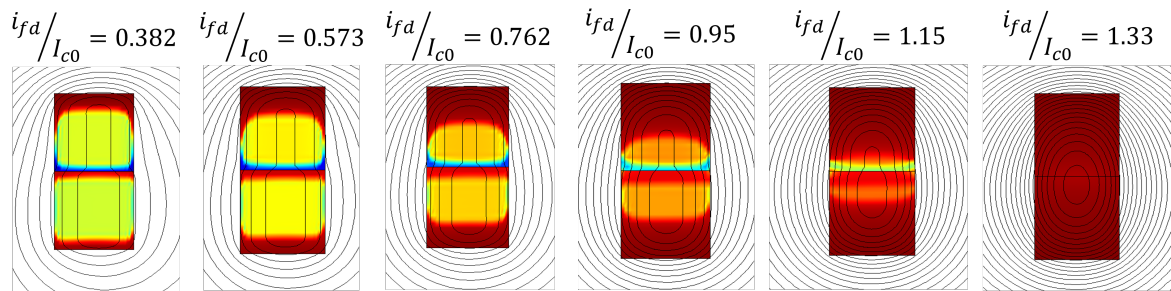
Fig. 3.18 Current and magnetic flux distribution in a 2-stack HTS winding under a ramp of current.

However, due to the complex dynamics of the superconductor's screening currents and their corresponding magnetic flux distribution, different coil shapes and different stack configurations require specific FEM analysis to be able to infer the sets of k function parameters. This is a limitation of the approach in terms of the estimation of the current density distribution affecting the performance of the superconductor. Thus, a database containing the front functions of various stack topologies and their corresponding analyses is still pending for future work.

3.4   HTS machine MEC model

In order to estimate the magnetic behavior of a machine pole section, a reluctance network is created utilizing three distinct types of reluctance, representing the iron, the machine air gap, and the HTS field coil. The iron reluctances are considered with simple shapes to make modeling easier, given their nonlinear behavior. The air reluctances are built with complex geometries to model the magnetic flux leakage over the air. While the HTS field coil reluctances are built by considering the current density distribution and its corresponding magnetic field pattern, both computed via the **T-A** formulation with homogenization technique. The reluctance network is superimposed over the magnetic flux lines obtained obtained form the FEM, as shown in Fig. 3.19. The surrounding circuits drawn with dotted lines indicate an antiperiodicity boundary of the pole section. To address the non-linearity caused by the H dependence of iron magnetic permeability, the mesh analysis method has been chosen to solve the resulting MEC system of equations. This method requires fewer iterations to converge through the Newton-Raphson algorithm compared to nodal analysis, as explained in the Appendix B. To apply properly the mesh-based MEC model, each subcircuit of the MEC must meet the planar circuit condition, i.e., all subcircuits must be drawn on a plane surface without any intersections. The reluctance and its corresponding magnetic flux within a branch "k" represent the key components to conform the mesh-based network as illustrated in Fig. 3.20a. The mesh-based analysis technique uses (3.32) to solve the magnetic fluxes in the network through a equivalent reluctance matrix $\mathbf{R}_{\mathrm{mg}}$, created by a straightforward mesh analysis formulation algorithm (see Appendix A).
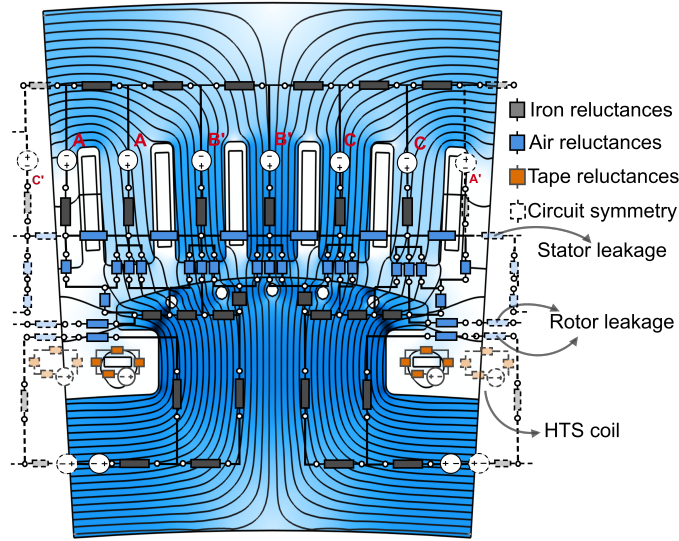
Fig. 3.19 Magnetic flux distribution from FEM and superimposed reluctance network (MEC).

The nonlinear system governing the MEC is,

$$\mathbf{f}(\Phi) = \mathbf{R}_{\mathrm{mg}}(\Phi)\,\Phi - \mathbf{F}_{\mathrm{mm}} = 0 \tag{3.40}$$

where $\mathbf{f}$, $\mathbf{F}_{\mathrm{mm}}$ and Φ are the residual function vector, the vector of magnetomotive forces (mmf) and the vector of magnetic fluxes, respectively. The equivalent reluctance matrix elements are computed for every magnetic circuit branch "k" via (3.33). The remaining components of (3.40) are represented as follows,

$$\Phi = \begin{bmatrix} \phi_{\mathrm{s}}, \ \phi_{\mathrm{r}}, \ \phi_{\mathrm{g}} \end{bmatrix}, \quad \mathbf{F}_{\mathrm{mmf}} = \begin{bmatrix} \mathbf{F}_{\mathrm{s}}, \ \mathbf{F}_{\mathrm{r}}, \ \mathbf{F}_{\mathrm{g}} \end{bmatrix} \tag{3.41}$$

where the subscripts "s", "r" and "g" symbolize the corresponding mesh-flux-loops and the MMF sources in the stator, the rotor and the air gap, respectively.

(a) Branch reluctance element

(b) Non-linear magnetic circuit
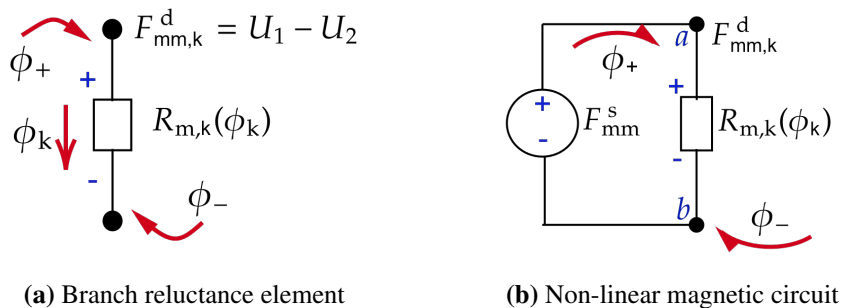
Fig. 3.20 Basic elements constituting the mesh-based MEC loops.

The magnetic sources of stator and rotor are expressed as,

$$\mathbf{F}_s = \mathbf{N}_{abc,s}^{(n_s \times m)} \, \mathbf{i}_{abc}, \quad \mathbf{F}_r = \mathbf{N}_{fd}^{(n_{rl} \times 1)} \, i_{fd} \tag{3.42}$$

where $n_s = N_{ss}/p$, n_{rl}, $\mathbf{N}_{abc,s}$, $\mathbf{N}_{fd}$ and $\mathbf{i}_{abc}$ are the number of stator slots per pole, the number of rotor magnetic loops in the MEC, a matrix containing the number of turns per slot per phase, a matrix containing the number of turns per slot per phase, a vector defining the enclosed field coil turn number within a rotor magnetic loop, and the stator currents, respectively.

The nonlinear system given in (3.40) is solved through a predictor-corrector technique combined with a Newton-Raphson algorithm easing the convergence over a wide range of ampere-turns [108],

$$\Phi_{i+1} = \Phi_i - \mathbf{J}^{-1} \left(\mathbf{R}_{mg}(\Phi_i)\Phi_i - \mathbf{F}_{mmf} \right) \tag{3.43}$$

where "i" is the iteration number and $\mathbf{J}$ is the Jacobian matrix. Since $\mathbf{F}_{mmf}$ is not a function of Φ, the Jacobian matrix can be split into a linear and nonlinear part so that,

$$\mathbf{J} = \frac{\partial}{\partial \Phi}(\mathbf{R}_{mg}(\Phi)\Phi) = \underbrace{\mathbf{R}_{mg}}_{\text{linear}} + \underbrace{\mathbf{DR}_{mg}}_{\text{nonlinear}} \tag{3.44}$$

The matrix $\mathbf{DR}_{mg}$ contains the partial derivatives related to the flux-dependent reluctances, i.e., the reluctance elements associated with iron. While the linear terms related to the air and the superconductor remain unchanged in the Jacobian. The terms of the nonlinear matrix $\mathbf{DR}_{mg}$, computed via the chain rule, are given below,

$$\frac{\partial}{\partial \phi_{k+,k-}}(R_{m,k} \, \phi_{b,k}) = \left(\frac{\partial R_{m,k}}{\partial \mu_k} \frac{\partial \mu_k}{\partial B_{b,k}} \frac{\partial B_{b,k}}{\partial \phi_{b,k}} \frac{\partial \phi_{b,k}}{\partial \phi_{k+,k-}} \right) \phi_{b,k} \pm R_{m,k} \tag{3.45}$$

with,

$$\frac{\partial R_{m,k}}{\partial \mu_{r,k}} = -\frac{R_{m,k}}{\mu_{b,k}}, \qquad\qquad \frac{\partial B_{b,k}}{\partial \phi_{b,k}} = \frac{1}{A_k},$$

$$\frac{\partial \mu_k}{\partial B_{b,k}} \text{ from } B-H \text{ curve}, \qquad\qquad \frac{\partial \phi_{b,k}}{\partial \phi_{k+,k-}} = \pm 1$$

where μ_k and $B_{b,k}$ are the permeability of the ferromagnetic material and the mean magnetic flux density of branch "k".

The mean magnetic flux density $B_{b,k}$ is computed as the ratio of the corresponding magnetic branch flux $\phi_{b,k}$ and the corresponding reluctance element cross-sectional area A_k.

$$B_{b,k} = \frac{\phi_{b,k}}{A_k} = \frac{\phi_+ - \phi_-}{A_k} \tag{3.46}$$

were "+" and "-" correspond to the flux entering and leaving from branch "k" through the associated reluctance element, respectively.

3.5 HTS field coil synchronous machine model

A 8th-order dq0 model with per unit reciprocal mutual inductance is used to simulate a grid-connected generator [109, 110]. The copper bars located within the pole tip has been modelled as damping coils with equivalent resistances and inductances, which provide an extra flux linkage decomposed into λ_{kd} and λ_{kq} to achieve stability during transients [54, 55]. The equivalent diagram of the dq0 machine model is shown in Fig. 3.21. The corresponding electrical machine parameters are obtained analytically based on [102, 104, 105] and given in Table 3.4. All the phase variables "abc" are converted to the dq0 frame-of-reference through the Park transformation $\mathbf{T}_{\text{Park}}$ given in [111] and recalled in (3.47). The electrical angular displacement θ_r is obtained through the mechanical angular displacement θ_{rm} and the pole number p, as $\theta_r = (p/2)\theta_{rm}$.
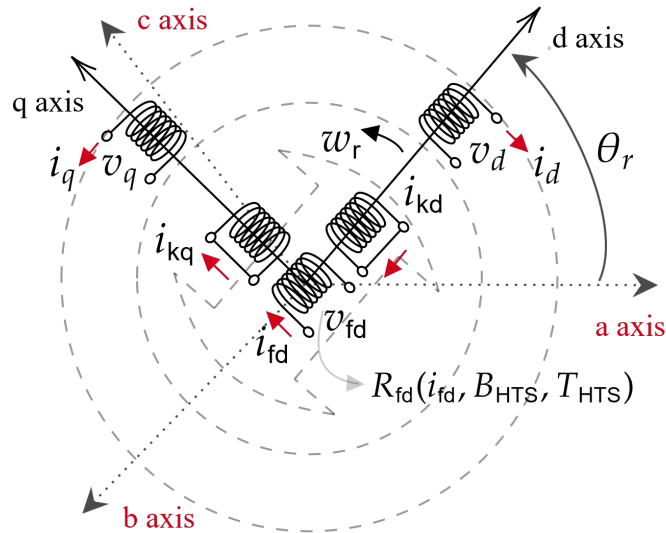
Fig. 3.21 Diagram of synchronous machine in the dq0 frame of reference.

$$\mathbf{T}_{\text{Park}} = \frac{2}{3} \begin{bmatrix} \cos(\theta_r) & \cos\left(\theta_r - \frac{2\pi}{3}\right) & \cos\left(\theta_r + \frac{2\pi}{3}\right) \\ -\sin(\theta_r) & -\sin\left(\theta_r - \frac{2\pi}{3}\right) & -\sin\left(\theta_r + \frac{2\pi}{3}\right) \\ 1/2 & 1/2 & 1/2 \end{bmatrix} \quad (3.47)$$

The flux linkage state vector $\boldsymbol{\lambda}_{\text{dq0,r}}$ and the swing equation (with no damping torque considered, $\tau_D = 0$), expressed in pu (the base being the stator), are solved simultaneously via the set of equations,

$$\frac{d\boldsymbol{\lambda}_{\text{dq0,r}}}{dt} = \omega_{\text{rb}} \left(\mathbf{v}_{\text{dq0,r}} - \left(\text{RL}^{-1} - \text{W} \right) \boldsymbol{\lambda}_{\text{dq0,r}} \right) \quad (3.48)$$

$$\frac{d\Delta\omega_r}{dt} = \frac{1}{2H_{\text{in}}} (\tau_m - \tau_e) \quad (3.49)$$

$$\frac{d\delta}{dt} = \Delta\omega_r \quad (3.50)$$

where $\boldsymbol{\lambda}_{\text{dq0,r}} = [\lambda_d, \lambda_q, \lambda_0, \lambda'_{\text{fd}}, \lambda'_{\text{kd}}, \lambda'_{\text{kq}}]^{\text{T}}$ is the vector of magnetic flux linkages of the machine coils referred to the stator; $\mathbf{v}_{\text{dq0,r}}$ and $\mathbf{i}_{\text{dq0,r}}$ are the voltages and currents at the rotor and stator coils, respectively; $\Delta\omega_r$ is the deviation of the rotor angular speed and ω_{rb} is the base rotor angular speed, both in rad/s; $\delta = \theta_r - \theta_e$ is the load angle; H_{in} is the combined inertia constant of the turbine, the rotor, and the shaft that connects them; $\tau_m - \tau_e$ is the difference between the mechanical and electromagnetic torques. The electromagnetic torque is given in the dq0 reference as follows,

$$\tau_e = \frac{3p}{4} \left(\lambda_d i_q - \lambda_q i_d \right) \quad (3.51)$$

The resistance matrix R in pu given in (3.52) is a diagonal matrix representing the resistances of every coil within the machine, including the nonlinear HTS field coil resistance $r'_{\text{fd}}(i_{\text{sc}}, T_{\text{sc}}, B_{\text{sc}})$. The inductance matrix L in pu shown in (3.53) assumes that the current is uniform across the stator and rotor conductors (stranded model). In both matrices, the apostrophe means that rotor variables are referred to the stator.

$$R = \begin{bmatrix} r_s & 0 & 0 & 0 & 0 & 0 \\ 0 & r_s & 0 & 0 & 0 & 0 \\ 0 & 0 & r_s & 0 & 0 & 0 \\ 0 & 0 & 0 & r'_{\text{fd}} & 0 & 0 \\ 0 & 0 & 0 & 0 & r'_{\text{kd}} & 0 \\ 0 & 0 & 0 & 0 & 0 & r'_{\text{kq}} \end{bmatrix} \quad (3.52)$$

$$
L = \begin{bmatrix}
x_d & 0 & 0 & x_{md} & x_{md} & 0 \\
0 & x_q & 0 & 0 & 0 & x_{mq} \\
0 & 0 & x_0 & 0 & 0 & 0 \\
x_{md} & 0 & 0 & x'_{fd} & x_{md} & 0 \\
x_{md} & 0 & 0 & x_{md} & x'_{kd} & 0 \\
0 & x_{mq} & 0 & 0 & 0 & x'_{kq}
\end{bmatrix} \tag{3.53}
$$

Finally, the angular velocity matrix W of (3.54) is obtained from the phase flux linkages transformed via the Park transformation $\mathbf{T}_{Park}$.

$$
W = \begin{bmatrix}
0 & \omega_r & 0 & 0 & 0 & 0 \\
-\omega_r & 0 & 0 & 0 & 0 & 0 \\
0 & 0 & 0 & 0 & 0 & 0 \\
0 & 0 & 0 & 0 & 0 & 0 \\
0 & 0 & 0 & 0 & 0 & 0 \\
0 & 0 & 0 & 0 & 0 & 0
\end{bmatrix} \tag{3.54}
$$

Table 3.4 Hybrid superconducting SM dq-model parameters (see Appendix C).

Parameter	Value (pu)	Parameter	Value (pu)
Stator resistance, r_s	0.02090	Rated field resistance, r'_{fd}	8.39×10^{-10}
d-axis damper resistance, r_{kd}	0.07552	q-axis damper resistance, r_{kq}	0.07519
Stator leakage reactance, x_{ls}	0.18377	Field leakage reactance, x'_{lfd}	0.03566
d-axis mutual reactance, x_{md}	0.75909	q-axis mutual reactance, x_{mq}	0.45334
d-axis damper leakage reactance, x'_{kd}	0.03807	q-axis damper leakage reactance, x'_{kq}	0.03790
Friction coefficient, F_{fr}	0	Inertia constant, H_{in}	0.047387 (s)

It is important to emphasize that in this work, the inputs to the MEC model are the field and the stator currents obtained through the SM dq0 model. The sole purpose of these inputs is to estimate the flux density impacting the HTS field coil. Nevertheless, further work could include the stator magnetic flux linkages from the MEC model as inputs to the SM dq0 model at each time step. This would result in a more realistic inclusion of saturation or signal distortion effects on the resultant flux linkages and their associated harmonics.

3.6   FEM formulation

The **T**-**A** formulation of the Maxwell's equations with homogenization technique is applied for the machine geometry defined in Table 4.1. The FEM was used for two purposes. First, a 2D quasi-magnetostatic FE analysis of one pole of the HTS-SM was performed to create a basis for the machine magnetic equivalent circuit model. The magnetic field generated by the stator was added to the dynamic field arising from current changes in the HTS field coil. This approach avoids the simulation of the machine transients while offering through a dynamic analysis the nonuniform distribution of current in the superconductor that would arise otherwise in transients. Second, a 2D rotating FE analysis was used to ensure that the no-load voltage and full-load current matched the initial design results.

Displacement current in the Ampere's law is neglected. Then, the governing equations for the model are given by,

$$\nabla \times \mathbf{H} = \mathbf{J} \tag{3.55}$$

$$\nabla \times \mathbf{E} = -\frac{\partial \mathbf{B}}{\partial t} \tag{3.56}$$

The constitutive relations characterize the machine materials' electromagnetic behavior and define the bounded universe's subdomains through the following expressions,

$$\mathbf{E} = \rho \mathbf{J} \tag{3.57}$$

$$\mathbf{B} = \mu \mathbf{H} \tag{3.58}$$

where μ is the magnetic permeability depending on the magnetic field for the iron core and equal to the permeability of vacuum μ_0 for the copper, the superconductor and the surrounding space; ρ is the electrical resistivity equal to ρ_{Cu} for the cooper, and ρ_{sc} for the superconductor.

The current density and the magnetic flux density can be expressed in terms of vector potentials **T** and **A** yielding to,

$$\nabla \times \mathbf{T} = \mathbf{J} \tag{3.59}$$

$$\nabla \times \mathbf{A} = \mathbf{B} \tag{3.60}$$

For current carrying regions, by substituing (3.57) and (3.59) in (3.56), the electric vector potential can be defined by the time variation of magnetic flux density, as shown in (3.61).
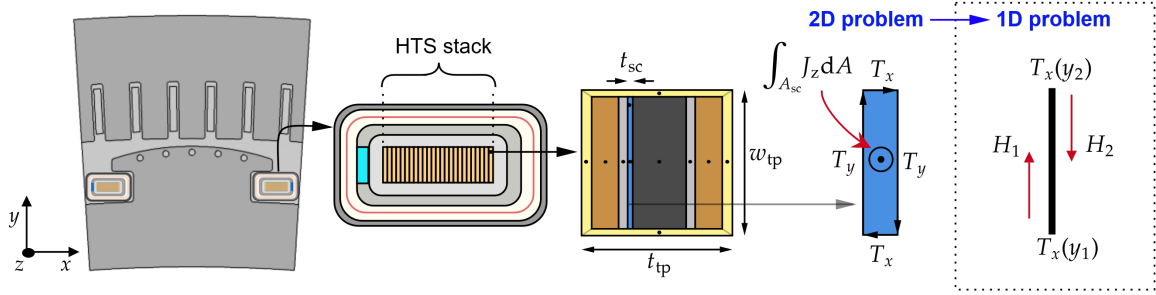
Fig. 3.22 Assumptions for the **T-A** formulation. The current vector potential **T** is defined over the transformed 2D-to-1D HTS layer. The magnetic vector potential **A** is computed over the entire machine cross-section.

In addition, by substituing (3.60) in (3.55), the magnetic vector potential can be expressed as a function of the current density, as shown in (3.62).

$$\nabla \times \rho \left(\nabla \times \mathbf{T} \right) = -\frac{\partial \mathbf{B}}{\partial t} \tag{3.61}$$

$$\nabla \times \frac{1}{\mu} \left(\nabla \times \mathbf{A} \right) = \mathbf{J} \tag{3.62}$$

By developing the left-hand expression of (3.62), It should be noted that the value of **A** can be uniquely defined if its divergence is also defined. A trivial choice for this requirement is known as the Coulomb's gauge condition given by,

$$\nabla \cdot \mathbf{A} = 0 \tag{3.63}$$

As long as the displacement current remains negligible and assuming the Coulomb's gauge condition of (3.63), the magnetic vector potential defined within current-carrying regions is solved by,

$$\nabla^2 \mathbf{A} = -\mu \mathbf{J} \tag{3.64}$$

It is assumed that the current flows only in the HTS layers of the field coil, so the tape's metallic layers are neglected, while the surrounding medium is assumed to be non-conductive. Therefore, the right-hand term in (3.64) becomes zero for all regions other than the SC layers, i.e., $\nabla^2 \mathbf{A} = 0$. In the presented 2D problem, the current density only has one component in the z-axis direction $\mathbf{J} = J_z \, \hat{\mathbf{k}}$ as shown in Fig. 3.22.

According to (3.64) and (3.57), **J** determines **A** and **E**, respectively, so both vectors have only one component in the z-axis direction too. Furthermore, **E** can be expressed as a combination of the electric scalar potential V and the derivative of the magnetic vector potential as follows,

$$\mathbf{E} = -\left(\frac{\partial \mathbf{A}}{\partial t} + \nabla V\right) \tag{3.65}$$

As the z component of the magnetic vector potential A_z remains constant through the axial length direction, their iso-potential curves agree with the magnetic flux lines, and the field solution defined by (3.60) can be found over plane xy as shown next,

$$B_x = \frac{\partial A_z}{\partial y}, \quad B_y = -\frac{\partial A_z}{\partial x} \tag{3.66}$$

Moreover, the current density can also be represented by the electric vector potential given in (3.59), as follows,

$$J_z = \left(\frac{\partial T_y}{\partial x} - \frac{\partial T_x}{\partial y}\right)\hat{\mathbf{k}} \tag{3.67}$$

The central assumption for modelling the superconducting field coil with the **T**-**A** formulation are related with the transformation of a 2D element (the HTS layer) in a 1D element within a 2D model [76]. As long as the SC tape has a large aspect ratio ($\chi_{sc} = w_{tp}/t_{sc}$), the HTS thin layer (with its corresponding thick and width) can be modeled as a 1D line. The 2D-to-1D HTS layer model transformation assumption in a vertical-oriented position illustrated in Fig. 3.22, determines that the first term of the right-hand element of (3.67) must be zero-valued due to the negligible HTS layer thickness. Then, the resultant current density corresponds to $J_z = -\partial T_x/\partial y$.

The field current, the field current density and the electric vector potential are coupled by the flux equation and the Stokes' theorem as follows,

$$i_{fd} = \int_{A_{sc}} \mathbf{J} \cdot \mathbf{n} dA = \oint_{l_{sc}} \mathbf{T} \cdot d\mathbf{l} \tag{3.68}$$

To ensure the appropriate boundary conditions for the component T_x over the equivalent 1D layer, the integration of the current density from (3.68) is applied, resulting the following expression,

$$J_z = -\frac{T_x(y_1) - T_x(y_0)}{t_{sc}} \tag{3.69}$$
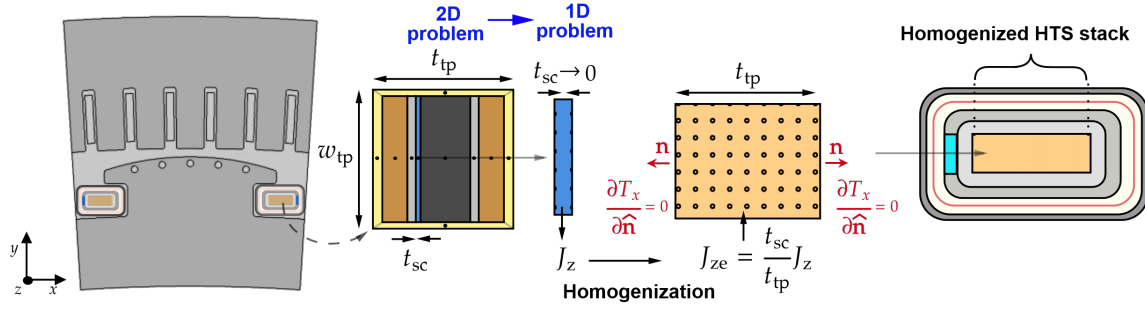
Fig. 3.23 Assumptions for the **T-A** formulation with homogenization technique which transform the HTS stack into a homogeneous bulk.

Substituting (3.69) in (3.68) and rearranging terms while considering $y_0 = 0$ and $y_1 = w_{tp}$, the boundary values for T_x in terms of the field current are given by,

$$i_{fd} = -(T_x(y_1) - T_x(y_0))t_{sc} \tag{3.70}$$

The above equation states that the field current can be imposed by modifying the values of $T_x(y_0)$ and $T_x(y_1)$.

For practical purposes, the boundary condition $T_x(y_0)$ can be set to zero, while the remaining one naturally yields $T_x(y_1) = i_{fd}/t_{sc}$. However, as the current density within the HTS layer has been transformed into a 1D problem, an equivalent current density must be defined in order to solve the 2D density distribution. For this reason, the boundary conditions given in (3.68) are applied along the tape's horizontal edges illustrated in Fig. 3.23. Whereas the tape's vertical edges must satisfy the Neumann boundary condition given by $\partial T_x/\partial\hat{\mathbf{n}} = 0$, where $\hat{\mathbf{n}}$ is the unit vector normal to the tape. Therefore, the homogenization strategy illustrated in Fig. 3.23 can be applied to express the HTS layer 1D current density J_z into an equivalent 2D current density J_{ze} over the tape, as follows,

$$J_{ze} = \frac{t_{sc}}{t_{tp}}J_z \tag{3.71}$$

where t_{sc}/t_{tp} is the ratio between the actual thickness of the HTS layer and the tape thickness. Then, according to (3.64), J_{ze} is imposed as a source term in the 2D tape subdomain, resulting in,

$$\nabla^2 A_z = -\mu J_{ze} \tag{3.72}$$
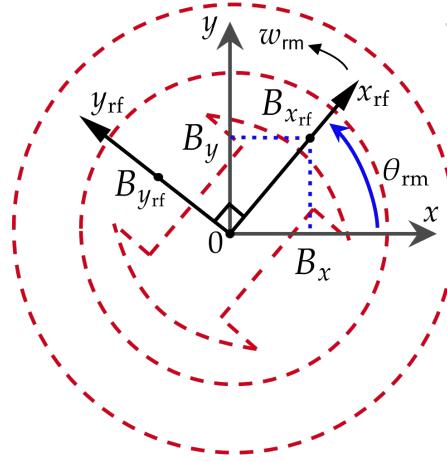
Fig. 3.24 Representation of the static coordinate system xy, and the rotating coordinate system $x_{rf}y_{rf}$ for modelling the relative motion between stator and rotor electromagnetic fields.

One racetrack field coil is composed of $N_{fd,p}$ number of tape turns wounded as a stack. Therefore, with the homogenization technique, the HTS stack can be converted into a homogeneous anisotropic bulk to integrate all the remaining SC layers. According to (3.71), the total stack current density naturally corresponds to $N_{fd,p}J_{ze}$, so the superconducting properties of the HTS layers are rescaled to a new cross-section area with almost the same electromagnetic behavior as the original HTS stack.

Since the rotor mechanical angular displacement θ_{rm} must be considered to simulate the induced stator voltages created by the rotating magnetic field of the rotor, it is convenient to use two reference systems, one for the fixed machine elements (xy coordinates) and one for the rotating machine elements ($x_{rf}y_{rf}$ coordinates). Given the diagram of Fig. 3.24, a transformation $\mathbf{M}_{rf}$ may be defined over an arbitrary rotating vector of the rotor, and the resultant vector will undergo a similar transformation as the magnetic flux density given by,

$$\mathbf{B}_{rf} = \begin{bmatrix} B_{x_{rf}} \\ B_{y_{rf}} \end{bmatrix} = \underbrace{\begin{bmatrix} \cos\left(\theta_{rm}\right) & \sin\left(\theta_{rm}\right) \\ -\sin\left(\theta_{rm}\right) & \cos\left(\theta_{rm}\right) \end{bmatrix}}_{\mathbf{M}_{rf}} \begin{bmatrix} B_x \\ B_y \end{bmatrix} \tag{3.73}$$

Such a transformation allows the electromagnetic field equations to be solved in a rotating coordinate system where the rotor is virtually fixed (the rotor frame), whereas the stator problem is solved in the conventional static coordinate system (the stator frame). Consequently, a new set of equations are available by applying the transformation M_{rf} to the electromagnetic fields.

Most vector quantities are merely rotated when transformed from the stator to the rotor frame, and their norms remain invariant. However, an exception occurs with the electric field, where the magnitude does not remain invariant. For this reason, the Lorentz transformations are used to simplify the rotating model problem [77]. The software COMSOL contains these transformations built within the rotating machine interface in its predefined library. The transformations for the magnetic and electric field yields,

$$\mathbf{B}(x,y) = \mathbf{B}_{\mathrm{rf}}(x_{\mathrm{rf}}, y_{\mathrm{rf}}) \tag{3.74}$$

$$\mathbf{E}(x,y) = \mathbf{E}_{\mathrm{rf}}(x_{\mathrm{rf}}, y_{\mathrm{rf}}) - v(x,y) \times \mathbf{B}_{\mathrm{rf}}(x_{\mathrm{rf}}, y_{\mathrm{rf}}) \tag{3.75}$$

where $v(x,y)$ is the velocity of a point (x,y) of the rotor in the stator frame.

Chapter 4

Wind power system modeling framework

4.1 Introduction

This chapter presents a wind power system consisting of a direct-drive horizontal-axis three-blade wind turbine with an HTS field coil synchronous generator coupled to a power grid through a variable-frequency full-scale power converter. The mechanical parameters from a reference wind turbine of 15 MW given in [101] are used to define the electrical generator input mechanical power P_{mec} and its rated angular rotor speed ω_{mec}. Those values are used as inputs for the electrical machine design procedure. The proposed electrical generator corresponds to a 15 MW HTS field coil SM and is used as a basis for modeling such a machine connected to a power grid through a variable-frequency back-to-back power converter.

4.2 Wind turbine modeling

The mechanical power of a wind turbine is given by

$$P_{\text{mec}} = \frac{1}{2}\zeta_{\text{air}}A_{\text{wtr}}c_{\text{P}}v_{\text{w}}^3 \qquad (4.1)$$

where ζ_{air}, A_{wtr}, c_{P} and v_{w} are the air density, the wind turbine rotor swept area, the wind turbine power coefficient and the wind speed, respectively. The power coefficient c_{P} is a nonlinear function depending on the wind incidence angle β and the tip speed ratio λ_{tsr}, and defines the maximum wind power that can be extracted from the wind kinetical energy at specific conditions.
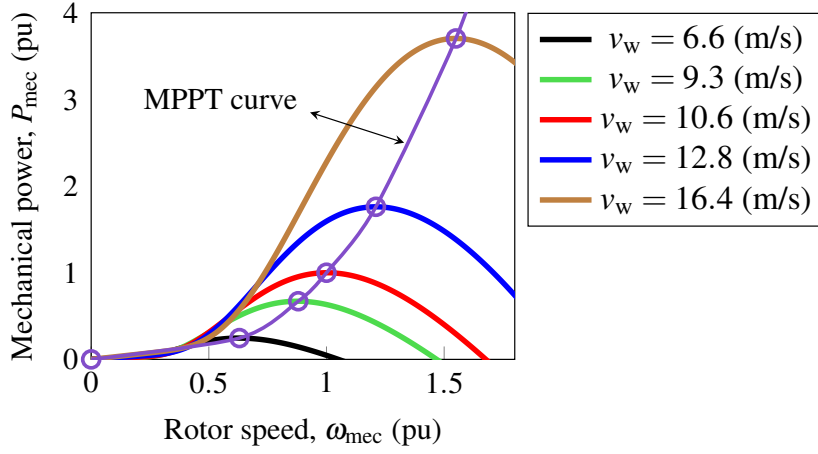
Fig. 4.1 Wind turbine power extraction as a function of the rotor speed in pu.

The wind turbine c_P is modeled with the following fitting function based in [101],

$$c_P = 0.5186 \left(\frac{115}{\lambda_{tsr,i}} - 0.4\beta - 4 \right) e^{-23/\lambda_{tsr,i}} + 0.0068\, \lambda_{tsr} \tag{4.2}$$

where $\lambda_{tsr,i}$ is given by

$$\frac{1}{\lambda_{tsr,i}} = \frac{1}{\lambda_{tsr} + 0.08\beta} - \frac{0.035}{\beta^3 + 1} \tag{4.3}$$

and the tip speed ratio is defined as,

$$\lambda_{tsr} = \frac{\omega_{mec} R_{wtr}}{v_w} \tag{4.4}$$

where ω_{mec} and R_{wtr} are the mechanical rotor speed and the wind turbine swept radius.

By assuming a given wind velocity, there is an optimal value for ω_{mec} at which c_P is the maximum for every curve generated by (4.2). If a swept of v_w is made, a fitting function which tracks the wind turbine maximum power extraction can be constructed as illustrated in Fig.4.1. This function is used to control the generator rotor speed to an optimal value at a given wind velocity for maximum power generation. The algorithm that follows this principle is known as the maximum power point tracking (MPPT).

The rotor turbine diameter D_{wtr} is obtained by rearranging (4.1), as shown in (4.5) [13]. The mechanical angular speed ω_{mec} is computed with the rated tip speed ratio $\lambda_{tsr,n}$ and the rated wind velocity $v_{w,n}$ as given in (4.6).

$$D_{wtr} = 2 \sqrt{\frac{2P_{mec}}{\pi c_P \zeta_{air} v_{w,n}^3}} \tag{4.5}$$

$$\omega_{mec} = 2 \frac{\lambda_{tsr,n} v_{w,n}}{D_{wtr}} \tag{4.6}$$

4.3   HTS-SM sizing

The HTS generator sizing starts with the output power equation given in (4.7) expressed in terms of the air-gap flux density B_L (magnetic loading), the magnetic field produced by the stator currents H_L (electric loading), the machine volume and the rotor speed ω_{mec} [102].

$$S_n = \frac{\pi}{2\sqrt{2}} k_w H_L B_L D_{is}^2 l_{ax} \omega_m \tag{4.7}$$

The proposed 15 MW machine design process is summarized in Fig. 4.2 based in [102–105]. The process begins by defining the machine's rated parameters and the key geometric factors, which are optimal values based on empirical research. The rated values correspond to the apparent power S_n, the RMS line-to-line voltage V_n, the mechanical frequency f_{mec}, the magnetic loading B_L, the electrical loading H_L, and the sator current density J_s. The geometric relation factors correspond to the stator winding factor k_w, the stator slot width ratio k_{ssr} and the rotor pole body width ratio k_{pb}. A suitable stator inner diameter D_{is} and axial length l_{ax} are obtained to compute the stator coil parameters. These parameters correspond to the stator coil number of turns $N_{\phi s}$, the stator number of slots N_{ss}, the stator conductors per slot Z_{slot}, the stator conductor cross-section area Z_{scsa} and the pole pitch length τ_{sp}. The stator coil parameters are modified if k_{ssr} is out of the range $0.3 \leq k_{ssr} \leq 0.6$. Then, the slot-filling factor k_{sfill}, the stator tooth depth d_{ss}, and the stator yoke depth d_{sy} are computed. After this, the field coil space factor k_{fd}, the rotor pole depth d_{pb}, and the rotor yoke depth d_{ry} are calculated. If the rotor pole body width ratio satisfies the condition $0.55 \leq k_{pb} \leq 0.75$, a saturation factor α_{sat} is calculated; else, k_{pb} is changed and a new geometry is computed. In agreement with [102], if $\alpha_{sat} \geq 0.8$, k_{ssr} is modified, and the cycle is repeated. Finally, if α_{sat} is within the defined range, the resulting magnetomotive force F_{mmT} is computed to obtain a suitable field coil number of turns N_{fd}. The design parameters and resulting dimensions of the machine are provided in Table. 4.1.
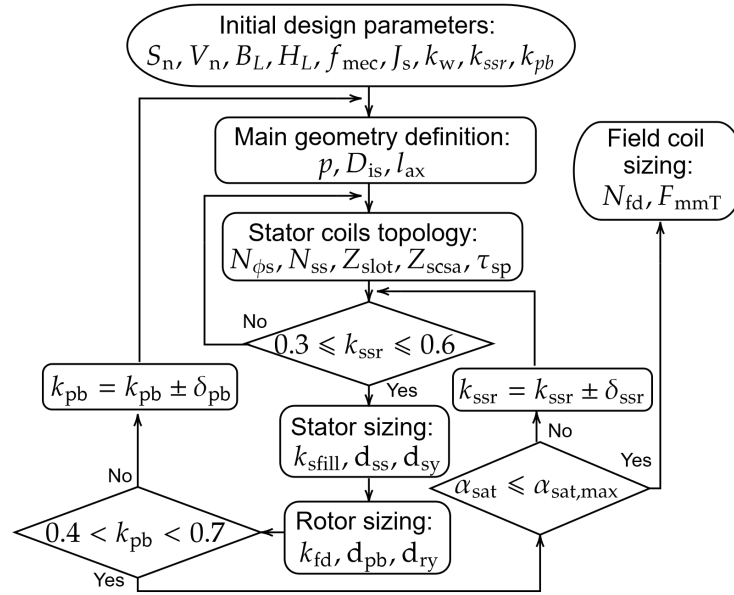
Fig. 4.2 Machine's sizing flow chart.

Table 4.1 Design parameters and resulting dimensions of a 15 MW wind turbine generator

Turbine rated parameters			
Rated wind velocity, $v_{w,n}$	10.6 m/s	Power coefficient, c_P	0.489
Cut-on velocity, $v_{w,on}$	3 m/s	Cut-off velocity, $v_{w,off}$	25 m/s
Tip speed ratio, λ_{rat}	9	Mechanical frequency, f_{mec}	0.12 Hz
Generator parameters and rated values			
Stator yoke flux density, B_{sy}	1.82 T	Rotor yoke flux density, B_{ry}	1.96 T
Stator tooth flux density, B_{st}	2.10 T	Pole body flux density, B_{pb}	2.10 T
Voltage Line-to-Line, V_n	4.77 kV	Frequency, f_n	3.05 Hz
Stator current density, J_s	3.20 A/mm^2	Field current, I_{fdn}	135 A
Magnetic loading, B_L	1.45 T	Electrical loading, H_L	90.0 kA/m
Rotor and stator geometry			
Winding factor, k_w	0.97	Stator slot ratio, k_{ssr}	0.30
Pole body ratio, k_{pb}	0.55	Saturation factor, α_{sat}	0.70
Stator fill factor, k_{sfill}	0.50	Modular cryostat space factor, k_{fd}	0.85
Number of poles, p	48	Aspect ratio, χ_{rat}	0.214
Stator axial length, l_{ax}	1.97 m	Inner stator diameter, D_{is}	9.214
Rotor inner radius, r_{ir}	8.53 m	Rotor yoke depth, d_{ry}	174 mm
Rotor pole depth, d_{rp}	144 mm	Rotor shank width, w_{pb}	319 mm
Rotor tip width, w_{pt}	438 mm	Stator yoke depth, d_{sy}	140 mm
Stator slot pitch, τ_{sp}	100 mm	Stator tooth depth, d_{st}	15.0 mm
Number of phases, m	3	Stator slot number, N_{ss}	288
Conductors per slot, Z_{slot}	4	Gap length, l_{gap}	20.4 mm
Stator phase turn number, $N_{\phi s}$	192	Rotor field turn number, N_{fd}	18,384

4.4   Back-to-back power converter modeling framework

In the back-to-back power converter configuration, one VSC is connected to the generator terminals, while the other is connected to the power grid through a coupling impedance. To simplify power flow modeling and control, the dq0 transformation is used to convert three-phase time-varying AC signals into two time-invariant DC signals. This transformation is applied on the VSC terminals of both the HTS machine side (refered with the subscript "str") and the electrical grid side (refered with the subscript "gtr").

4.4.1   Grid-side equations

The state equations for modeling the grid-side VSC currents, considering the grid-side coupling impedance consisting of a resistance R_g and an inductance L_g (as shown in Fig. 2.10), are given by

$$\frac{d}{dt}\begin{bmatrix} i_{g,q} \\ i_{g,d} \end{bmatrix} = \begin{bmatrix} -\frac{R_g}{L_g} & -\omega_s \\ \omega_s & -\frac{R_g}{L_g} \end{bmatrix}\begin{bmatrix} i_{g,q} \\ i_{g,d} \end{bmatrix} + \frac{1}{L_g}\begin{bmatrix} v_{gtr,q} - v_{g,q} \\ v_{gtr,d} - v_{g,d} \end{bmatrix} \tag{4.8}$$

where ω_s is the angular speed given by the power grid and the subscript g represents the electrical grid elements. It can be noted that (4.8) present cross-coupling terms representing rotational voltages between d and q axis. To ease the transfer function extraction, a decoupling of these terms are obtained by defining two new voltages given by,

$$\Delta v_{g,d} = v_{gtr,d} - v_{g,d} + \omega_s L_g i_{g,q} \tag{4.9}$$

$$\Delta v_{g,q} = v_{gtr,q} - v_{g,q} - \omega_s L_g i_{g,d} \tag{4.10}$$

Therefore, the first-order transfer functions for the grid dq elements correspond to,

$$F_g(s) = \frac{i_{g,d}}{\Delta v_{g,d}} = \frac{i_{g,q}}{\Delta v_{g,q}} = \frac{1}{R_g}\frac{1}{1 + \tau_g s} \tag{4.11}$$

where the time constant $\tau_g = L_g/R_g$.

4.4.2 DC-link equations

The instantaneous power balance relation between the grid-side VSC and the DC-link is defined by,

$$v_{DC} \, i_{DC} - \frac{3}{2} v_{g,d} \, i_{g,d} = 0 \tag{4.12}$$

The DC-link voltage is given by,

$$C \frac{dv_{DC}}{dt} = -i_{g,DC} - i_{s,DC} \tag{4.13}$$

the capacitor value must be selected by considering the voltage ripple and the control response of the DC-link voltage. This value may be computed as,

$$C = \frac{S_n}{4\pi V_{DC,n} \Delta V_{DC}} \tag{4.14}$$

where ΔV_{DC} is the peak-to-peak voltage ripple condition, typically chosen around 2% of the rated DC-link voltage $V_{DC,n}$.

The DC-link voltage controller is given by a first-order transfer function obtained by substituting $i_{g,DC}$ from (4.12) in (4.13) and by considering $i_{s,DC}$ as a disturbance, which yields,

$$F_{DC}(s) = \frac{v_{dc}}{i_{g,d}} = -\frac{3}{4C} \frac{1}{s} \tag{4.15}$$

4.4.3 HTS machine equations

The HTS generator inherently possesses a resistance and inductance, which together constitute the coupling impedance between the HTS machine and the machine-side VSC. Assuming a rotor position-oriented dq reference frame, the state equations for modeling the generator-side VSC currents can be obtained by extracting the d, q, and field components expressed as a function of currents instead of the flux linkages in (3.48), as follows:

$$\frac{d}{dt} \begin{bmatrix} i_q \\ i_q \\ i'_{fd} \end{bmatrix} = \begin{bmatrix} \frac{R_s}{L_q} & \frac{\omega_r L_d}{L_q} & 0 \\ -\frac{\omega_r L_q}{L_d} & \frac{R_s}{L_d} & 0 \\ 0 & 0 & -\frac{R'_{fd}}{L_{fd}} \end{bmatrix} \begin{bmatrix} i_q \\ i_d \\ i'_{fd} \end{bmatrix} + \begin{bmatrix} \frac{v_q}{L_q} - \frac{\omega_r L_{md} i'_{fd}}{L_q} \\ \frac{v_d}{L_d} \\ \frac{v'_{fd}}{L_{fd}} \end{bmatrix} \tag{4.16}$$

A decoupling of the rotational voltages from (4.16) is obtained by defining two new voltages given by,

$$\Delta v_{\mathrm{d}} = v_{\mathrm{d}} + \omega_{\mathrm{r}} L_{\mathrm{q}} i_{\mathrm{q}} \tag{4.17}$$

$$\Delta v_{\mathrm{q}} = v_{\mathrm{q}} - \omega_{\mathrm{r}} L_{\mathrm{d}} i_{\mathrm{d}} - \omega_{\mathrm{r}} L_{\mathrm{md}} i_{\mathrm{fd}}' \tag{4.18}$$

The corresponding first-order transfer functions for (4.16) are given by,

$$F_{\mathrm{s}}(s) = \frac{i_{\mathrm{d}}}{\Delta v_{\mathrm{d}}} = \frac{1}{R_{\mathrm{s}}} \frac{1}{1 + \tau_{\mathrm{d}} s} \tag{4.19}$$

$$F_{\mathrm{s,q}}(s) = \frac{i_{\mathrm{q}}}{\Delta v_{\mathrm{q}}} = \frac{1}{R_{\mathrm{s}}} \frac{1}{1 + \tau_{\mathrm{q}} s} \tag{4.20}$$

$$F_{\mathrm{fd}}(s) = \frac{v_{\mathrm{fd}}'}{i_{\mathrm{fd}}'} = \frac{1}{R_{\mathrm{fd}}'} \frac{1}{1 + \tau_{\mathrm{fd}} s} \tag{4.21}$$

where $\tau_{\mathrm{d}} = L_{\mathrm{d}}/R_{\mathrm{s}}$, $\tau_{\mathrm{q}} = L_{\mathrm{q}}/R_{\mathrm{s}}$ and $\tau_{\mathrm{fd}} = L_{\mathrm{fd}}'/R_{\mathrm{fd}}'$.

By expressing (3.51) in terms of the corresponding currents, an strategy is adopted to facilitate the torque control by regulating $i_{\mathrm{d}} = 0$ and mantaining a constant field current at a reference value $i_{\mathrm{fd}}' = i_{\mathrm{fd}}'^*$. This strategy yields,

$$\tau_{\mathrm{e}} = \frac{3}{4} p \, L_{\mathrm{md}} \, i_{\mathrm{fd}}'^* \, i_{\mathrm{q}} \tag{4.22}$$

The first-order transfer function for the mechanical speed control that responds to the q-axis current can be obtained by substituting (4.22) in (3.51), by neglecting the damping torque and considering the mechanical torque as a disturbance, yielding to,

$$F_{\omega} = \frac{\omega_{\mathrm{mec}}}{i_{\mathrm{q}}} = \frac{3}{4} p \frac{L_{\mathrm{md}} i_{\mathrm{fd}}'^*}{2 J_{\mathrm{in}}} \frac{1}{s} \tag{4.23}$$

where J_{in} is the inertia moment computed through the inertia constant H_{in} as follows,

$$J_{\mathrm{in}} = \frac{2 H_{\mathrm{in}} S_{\mathrm{n}}}{\omega_{\mathrm{mec,n}}^2} \tag{4.24}$$

4.4.4 Back-to-back control system

The main objective of this work is focused on the HTS-SM modeling, so an optimal control design for the wind power system is outside the scope of this thesis and will be considered in the outgoing doctoral works. Every system open-loop transfer function H_i given by (4.25) is simplified and represented as a PI controller in the wind power control system. The step-by-step tuning for the PI parameters and its associated control strategies are taken from [88–90].

$$H_i = G_{ci}F_i \tag{4.25}$$

where F and G are the plant and the controller transfer functions for the control of the variable of interest i. The controllers are defined through compensators with a transfer function G_c with the following structure,

$$G_c(s) = \frac{1}{1 + \tau_a s} \tag{4.26}$$

where $\tau_a = 1/f_{ref}$ is the time delay based in the pulse-width modulation reference signal frequency. Figures 4.4a to 4.5 provide an overview of the wind power control system.

The wind velocity determines the reference control signal for the machine rotor speed control. This signal is obtained by interpolating the optimal rotor speed values as a function of the corresponding wind speed as illustrated in Fig.4.3. It is assumed that the wind turbine enters into an aerodynamic loss behavior after the rated wind velocity is achieved so the optimal rotor speed is maintained in 1 pu.
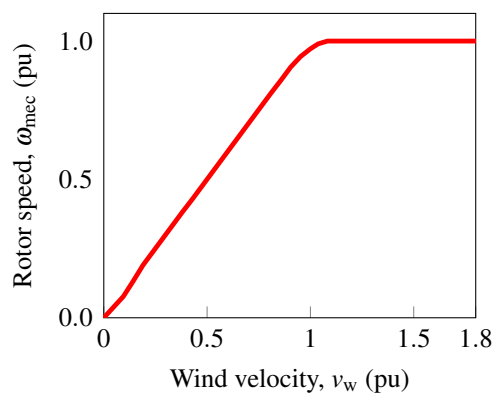
Fig. 4.3 Optimal rotor speed as a function of the wind velocity.
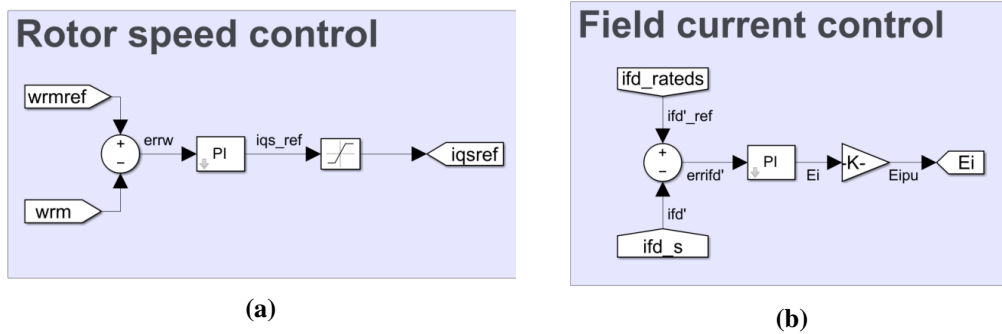
Fig. 4.4 Speed and field voltage control diagrams.

The output of the rotor speed control illustrated in Fig. 4.4a determines a reference q-axis current for the electromagnetic torque control that the machine must generate in response to a given mechanical torque. This is only possible by regulating the field current to a reference constant value through the field current control system (see Fig.4.4b), but also by regulating the machine reference d-axis current to a zero value, as shown in Fig. 4.5. The DC-link voltage control shown in 4.6 is regulated trough a constant reference voltage $v_{DC*} = V_{DC}$. The corresponding output determines the active power related to the reference d-axis current value entering the VSC grid-side control system given in Fig.4.7. With the reference control variables defined, the modulation signals which control the transistors for both VSCs are obtained.
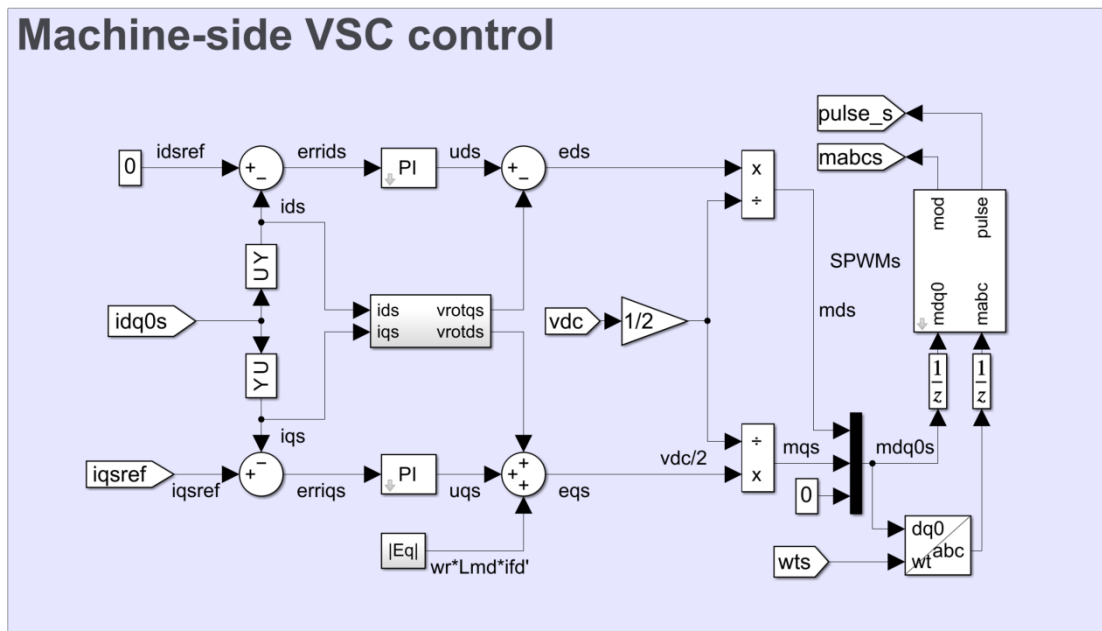
Fig. 4.5 HTS-SM side control diagram.
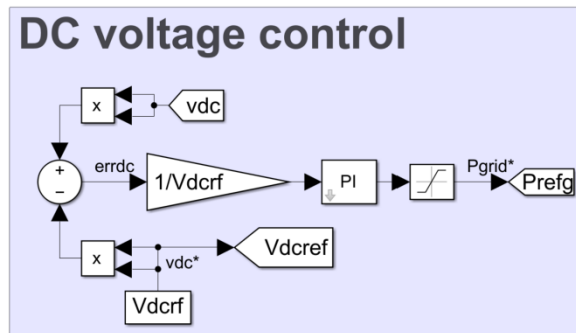
Fig. 4.6 DC-link voltage control diagram.
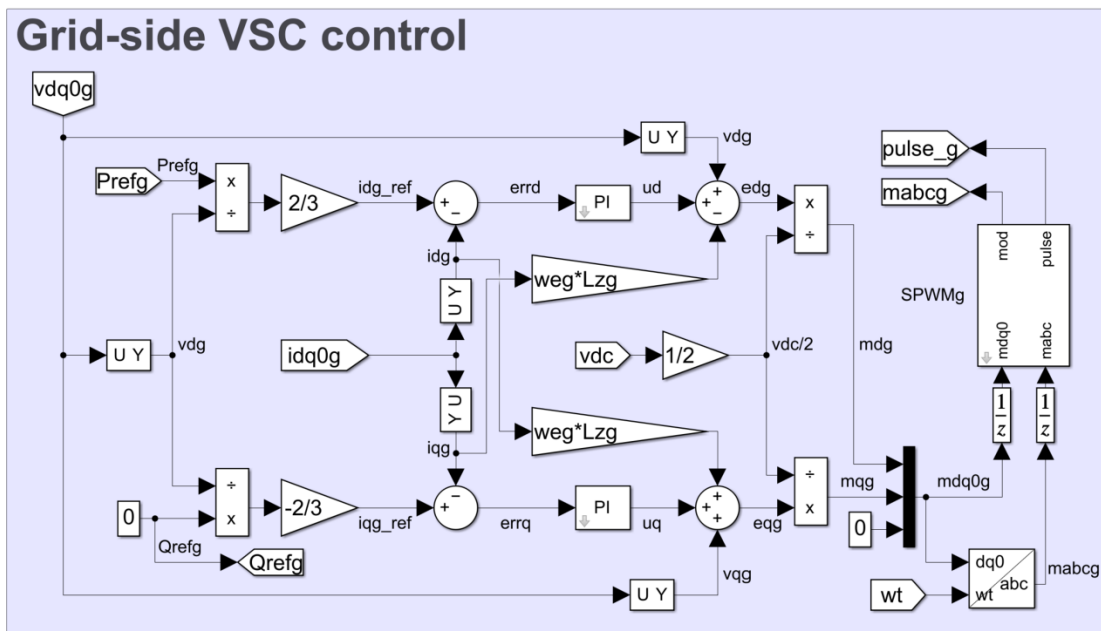
Fig. 4.7 Grid side control diagram.

Chapter 5

Case study

5.1 Introduction

The 15 MW HTS machine for wind power applications given in the previous chapter is the foundation for the FEM simulation outlined in the subsequent sections. The commercial finite element solver COMSOL Multiphysics (version 5.6) is used to perform a FEM simulation to verify the design results and create a foundation for MEC modeling. Then, the lumped-parameter generic model for such a machine, which includes the HTS stack thermoelectromagnetic model integrated with the field coil resistance, is used to study its transient stability under the most severe operating condition by applying a three-phase short circuit at the stator terminals. Lastly, a simulation of the HTS machine connected to the power grid through a variable-frequency full-scale power converter is presented. This work is preliminary and improvements in the control of the power flow is still ongoing at the time of the writing of this manuscript. A proper analysis using a refined FEM including electrical circuit coupling for transient is being developed to adress this approximation as part of the continuation of the present work outside the scope of the doctorate thesis.

5.2 FEM simulation

A pole section of the proposed generator has been simulated using the **T-A** formulation in the FEM software COMSOL Multiphysics®. The total domain is divided into two sections separated each other by a boundary (identity pair) located at the air gap: the rotor and the stator. Both sections have their respective mesh. Every mesh is built with smaller triangle elements near the air gap division and at iron element vertices, while the triangle sizes are

(a) Flux Distribution

(b) Harmonic content

(c) Stator voltages

(d) No load voltage test
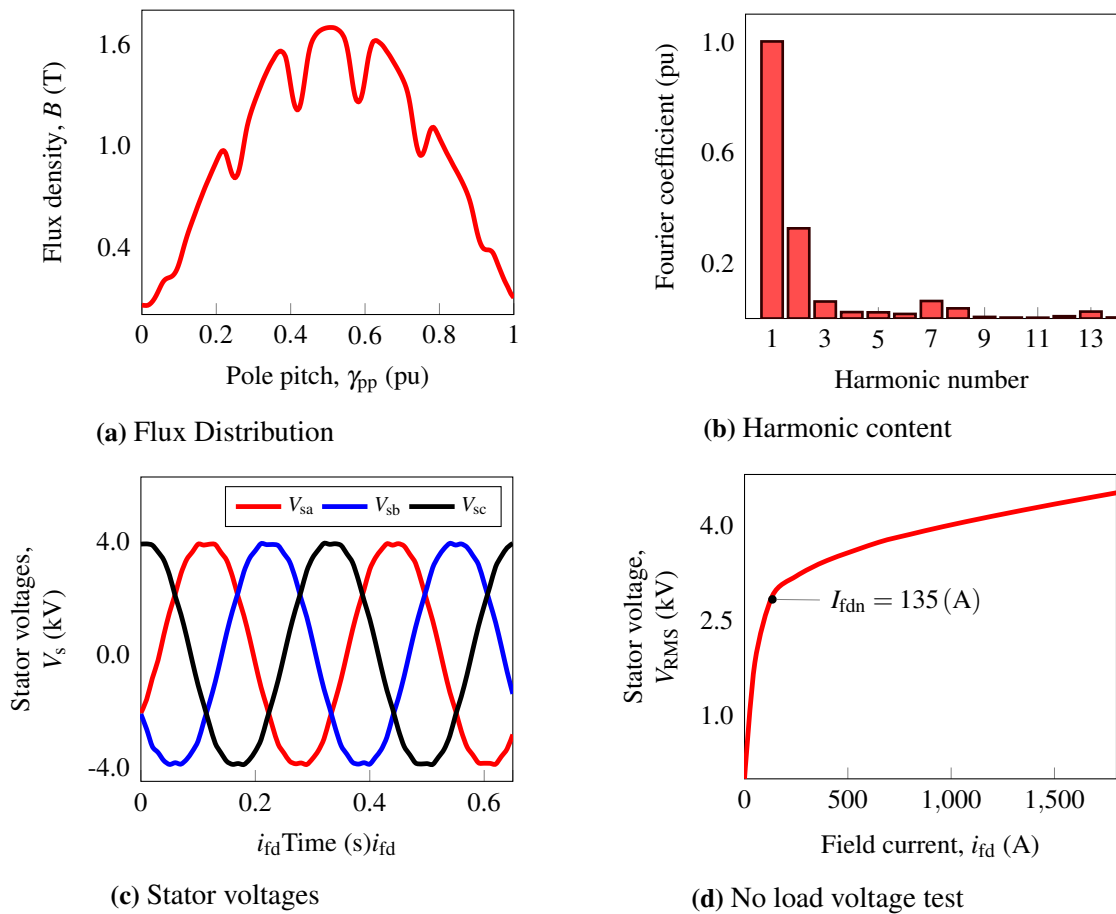
Fig. 5.1 FEM results for the proposed generator design operating at rated speed using the **T-A** formulation with homogenization technique.

bigger near the iron cores. The rotation is only applied to the rotor domain using the moving mesh approach, and modeled using a ready-made physics interface for rotating machinery.

The rated field current density is imposed through the HTS field coil cross-section, and the rated mechanical angular speed is defined as an initial value in the rotor domain. Over these assumptions, some of the FEM results are shown in Fig. 5.1. The air-gap flux density distribution with its corresponding impact due to the slotted stator is shown in Fig. 5.1a. It can be seen that the waveform is nearly sinusoidal but with a high-valued second harmonic as shown on the frequency spectrum of Fig. 5.1b. The flux density in air sections is smaller than in the yoke due to their lower permeability. The stator voltages at no-load condition, rated field current, rated speed and with barely distorted peak values due saturation, are presented in Fig. 5.1c.
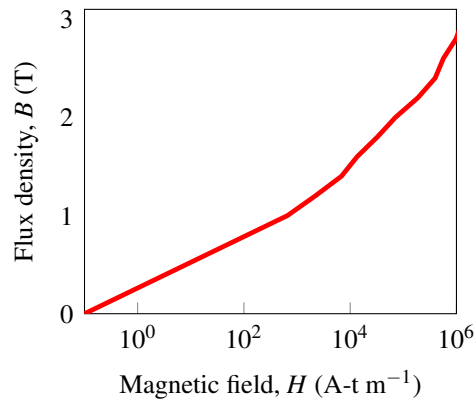
Fig. 5.2 *B-H* curve provided in the FEM COMSOL software.

Finally, the open-circuit characteristic is shown in Fig. 5.1d using the *B-H* curve provided in the FEM software (see Fig. 5.2). The machine magnetic flux distribution was computed for one electrical cycle at open circuit condition. Fig. 5.3 showcases the magnetic flux and magnetic flux density distributions at three distinct angular displacements. It should be noted that the rated current I_{fdn} is located on the "knee" of the open-circuit characteristic (Fig. 5.1d). This indicates that saturation levels within the machine's iron do not surpass reference prohibited values, i.e., the machine magnetic flux density magnitude does not go beyond $|\mathbf{B}| > 2.3$ T in any of the machine elements. Additionally, the average flux density values were solved over the 2D cut lines of the main machine elements shown in Table. 5.1 at a rotor displacement angle $\theta_{\text{e}} = 0$. The FEM results were cross-checked with those obtained through the MEC and their associated relative errors are presented. A comparison between the results of the HTS field coil MEC model with those from the FEM is shown in Fig. 5.4.

(a) $\theta_{\text{e}} = 66°$ **(b)** $\theta_{\text{e}} = 33°$ **(c)** $\theta_{\text{e}} = 0°$

Fig. 5.3 Magnetic flux density and magnetic flux distribution over a pole section in steady-state operation applying the **T-A** formulation with homogenization technique.
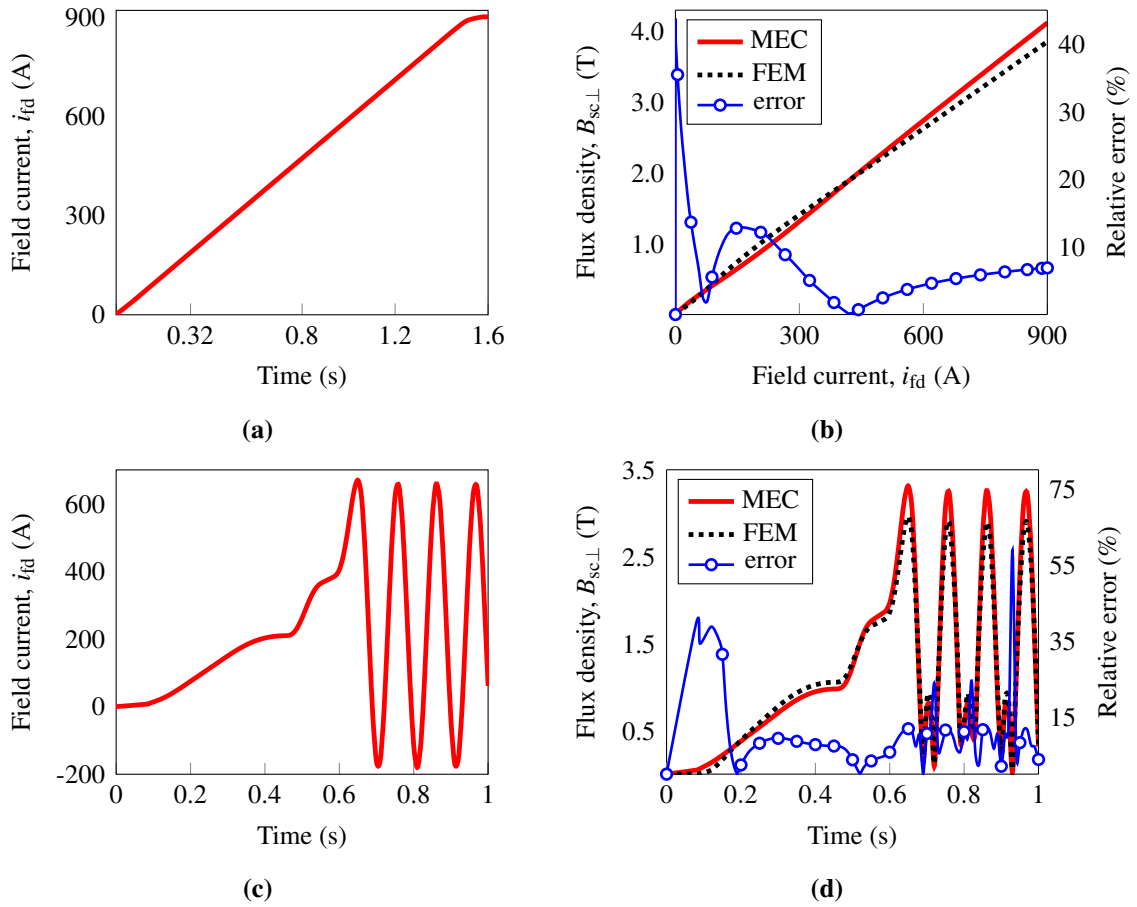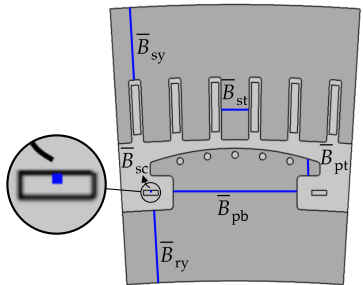
Fig. 5.4 FEM results for the proposed generator design operating at rated speed using the **T**-**A** formulation with homogenization technique.

The FEM assumes that for each increment of the machine rotor angle, the magnetic field generated by the stator is magnetostatic whereas the field co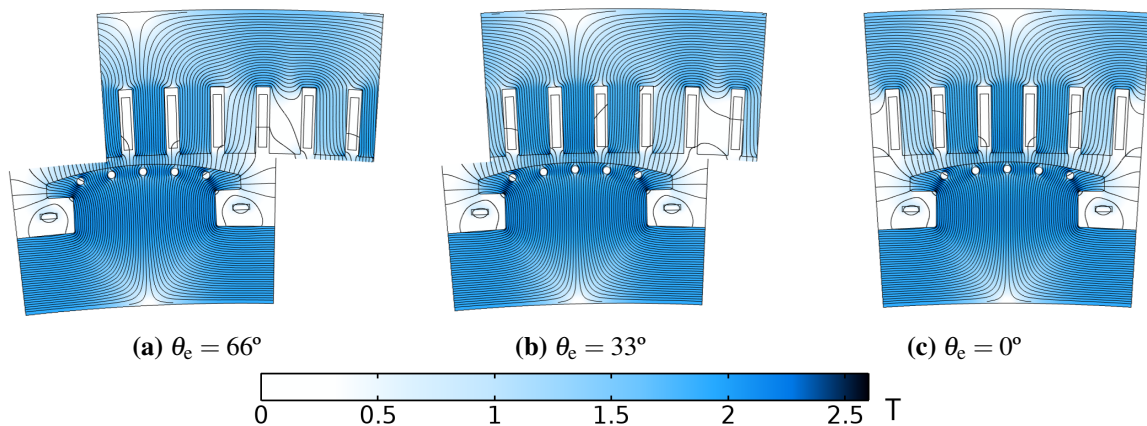il current is ramped from 0 to 900 A throughout the rotation (three times the critical current Ic of a single HTS tape) as given in Fig. 5.4a. Furthermore, the simulation is carried out for the HTS tape seeing the maximum value of the magnetic flux density on the winding for a component perpendicular to the tape surface $B_{sc\perp}$. This is the most stringent magnetic situation for the superconductor as the critical current of REBCO tapes significantly degrades with increasing magnitude of magnetic flux density and for a direction of the magnetic flux density perpendicular to the tape surface [33, 36]. Different HTS coil widths with ratios $w_{tp}/t_{tp} = \{1 : 0.5 : 5\}$ were simulated and a similar overall agreement as in Fig. 5.4b was achieved. In addition, the alternating field current of Fig. 5.4c was employed to verify the MEC model's accuracy during field coil transient conditions.

The results shown in Fig. 5.4d, present a reasonable accuracy compared to those obtained with COMSOL. Whereas the computation time is reduced to less than a second instead of hours using the FEM. It should be noted that Fig. 5.4b and Fig. 5.4d show a significant increase in the relative error generated by the poor fitting of the front functions near the origin when the field current approaches zero. Indeed, the relative error starts to increase rapidly to more than 12% over the range of $-23\,\text{A} \leq i_{\text{fd}} \leq 23\,\text{A}$. Whatever the case, the proposed MEC model methodology is definitely relevant for conducting analysis of the transient stability of power systems with HTS field coil SM including the response of the superconductor to transients.

Table 5.1 Machine's main average flux densities obtained by the MEC and the FEM. The FEM results are computed over the blue 2D cut lines shown in the figure.

Machine element	FEM (T)	MEC (T)	error (%)
Rotor yoke, $\overline{B}_{\text{ry}}$	1.9103	1.8231	4.56
Rotor shank, $\overline{B}_{\text{pb}}$	2.0377	1.9873	2.47
Rotor tip, $\overline{B}_{\text{pt}}$	2.0319	2.0911	2.91
Stator teeth, $\overline{B}_{\text{st}}$	1.9511	2.0000	2.50
Stator yoke, $\overline{B}_{\text{sy}}$	1.6121	1.6583	2.86
HTS field coil, $\overline{B}_{\text{sc}\perp}$	0.6256	0.5600	11.01

5.3 HTS field coil SM simulation

The thermoelectromagnetic lumped-parameter model of the HTS field winding presented in Chapter 3 is built as a Matlab function with the field current and machine geometry as inputs and the resistance defined by (3.6) and physical dynamics of the HTS winding as outputs. This function can be incorporated into a Simulink's block within the dq0 SM model that solve the flux linkages state variables found in (3.48) at the same time that solves the mechanical equations given in (3.49) and (3.50) following the chart diagram given in Fig. 3.1. The general circuit model given in Fig. 5.5 corresponds to one of the chosen case of studies. The study simplified the analysis of fundamental HTS machine behavior by excluding conversion stages and power devices connecting the machine to the network. This approach allowed for a deeper understanding of a stand-alone HTS machine's behavior when connected to an infinite bus before considering external circuits in a subsequent stage. Therefore, the generator is connected to the grid and a transient three-phase fault occurs at its stator terminals. The transient stability of the machine is studied for two cases, no transition of the HTS and its full transition from the superconducting to the normal-resistive state.
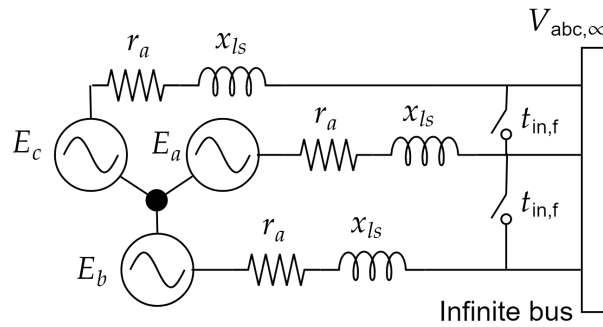
Fig. 5.5 Case study: a three-phase short circuit applied to the stator terminals. The generator is connected to an infinite bus simulating the connection of the machine to the power grid providing constant frequency for transient stability analysis.

These cases are compared to the response of a conventional machine of same output power at unity power factor and rated operation. As the fault occurs at the terminals of the machine, the infinite bus is therefore used to provide synchronism. Even though it is an approximation in terms of power systems engineering modelling, the idea behind this simplification is to study only the transient stability analysis of the synchronous machine alone [81, 84]. Three case studies are considered for the given synchronous generator subjected to a transient three-phase fault: 1) conventional generator (stable machine condition), 2) HTS generator with no transition of the HTS (stable machine condition), and 3) HTS generator with full transition of the HTS without the magnetic shielding (unstable machine condition). The first case includes current dampers in the poles of the rotor. The second case models the electromagnetic shields as damping coils [54]. The third case is an extreme, somehow unrealistic scenario for which no electromagnetic shields have been included in the design to destabilize the machine and quench the HTS coil. The infinite bus keeps the network frequency constant at $f_n = 3.05$ Hz (electric frequency provided by the generator before any conversion stages). The simulation is carried out in Simscape Electrical of Simulink [114]. The thermo-electromagnetic model is coded in a Matlab function interacting with the machine model built entirely in Simulink [115]. The simulation starts at steady-state nominal regime, delivering the rated active power to the bus before the fault occurs. The mechanical torque is assumed constant over the entire duration of the simulation with a nominal value of $\tau_m = 18.76$ MN.m. The tape flux density fitting parameter is considered as $B_0 = 0.5$ T. The fault occurs at $t_{in,f} = 16.7$ ms ($1/f$) with a duration of 4 cycles $t_{fin,f} = 66.7$ ms ($4/f$). The whole simulation lasts 100 s.

5.3.1 Response to a transient fault

For the subsequent analysis, the results are extracted from the turn located at the center of the field winding. The response of the induced field current for all three cases are shown in Fig.5.6(a). The resistance of the field winding for the conventional machine is assumed to be $R_{\text{fd,n}} \simeq R_{\text{fd}}$ (> 1 AWG wire) whereas the field winding for the HTS machine is $R_{\text{fd}} + R_{\text{sc}}$. During a fault, the resistance of the HTS winding increases according to the power law given by (2.2) so that the actual resistance of the rotor winding of the HTS machine increases by $R_{\text{fd}} + R_{\text{sc}}(0.105\ \Omega) > R_{\text{fd,n}}(0.1\ \Omega)$. Therefore, as the resistance of the HTS rotor is larger than the resistance of the conventional rotor during transients, the peak field current reached by the HTS machine is smaller than that of the conventional machine.

(a) Field current

(b) Rotor speed

(c) Field flux linkage

(d) Active and reactive power
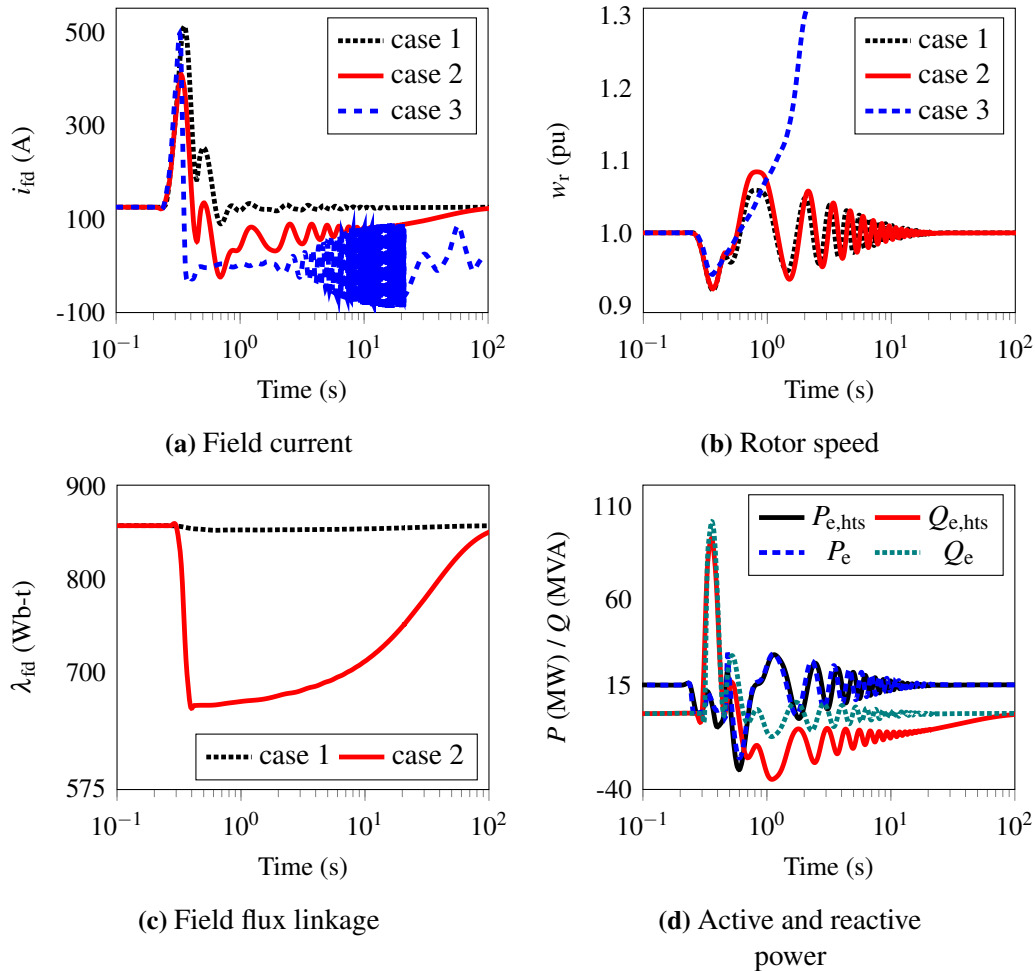
Fig. 5.6 Response of the machines (three cases) to the transient three-phase fault. The conventional machine is used as reference.

(a) Case 1   **(b)** Case 2
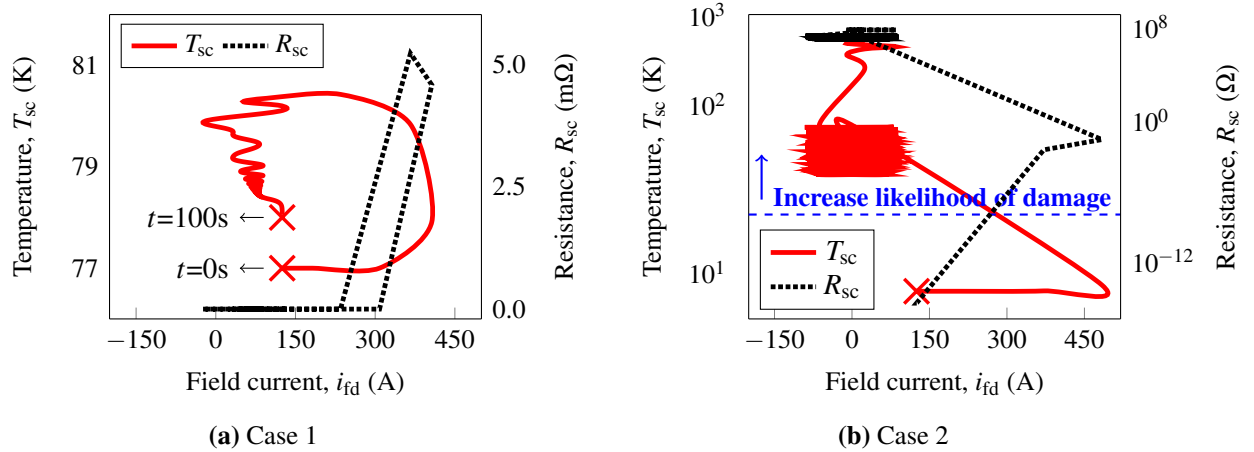
Fig. 5.7 Evolution of the temperature of the HTS layer T_{sc} and the corresponding resistance R_{sc} for the central turn of the field winding.

In the case 3, as the superconductor undergoes a full transition from the superconducting state to the normal-resistive state, the resistance of the HTS winding saturates to the resistance of the tape metallic layers ($> 1\ \Omega$) leading to a further reduction of the field current which remains near zero during the duration of the fault. In this case, the machine does not recover its nominal regime as shown in Fig. 5.6(b) and the angular speed diverges. For case 1 and 2, the nominal regime is recovered. As shown in Fig. 5.6(a), it takes longer for the HTS machine to recover its original state.

Indeed, its dynamic behavior is largely dictated by the thermal response of the HTS whose thermal time constant is much slower than the electromechanical one. The latter is the same for cases 1 and 2 as shown in Fig. 5.6(b). In case 2, the flux linkage λ_{fd} drops considerably during the fault which leads as well to an increase in the reactive power exchange between the machine and the network as emphasized by Fig. 5.6(c) and Fig. 5.6(d). The active power is similar for both cases which is consistent with the evolution of the angular speed (see Fig. 5.6(b)). The flux linkage evolves according to the ratio of the inductance and the resistance. As the resistance of the HTS depends on current, magnetic flux density and temperature, the time response is also depending on the same variables. It takes more than 100 s for the temperature of the superconductor to retrieve the operating temperature. However, the HTS resistance which also depends on the magnitude of the current recovers sooner (about 100 s) since the HTS machine in case 2 never fully transits as shown in Fig. 5.7a.
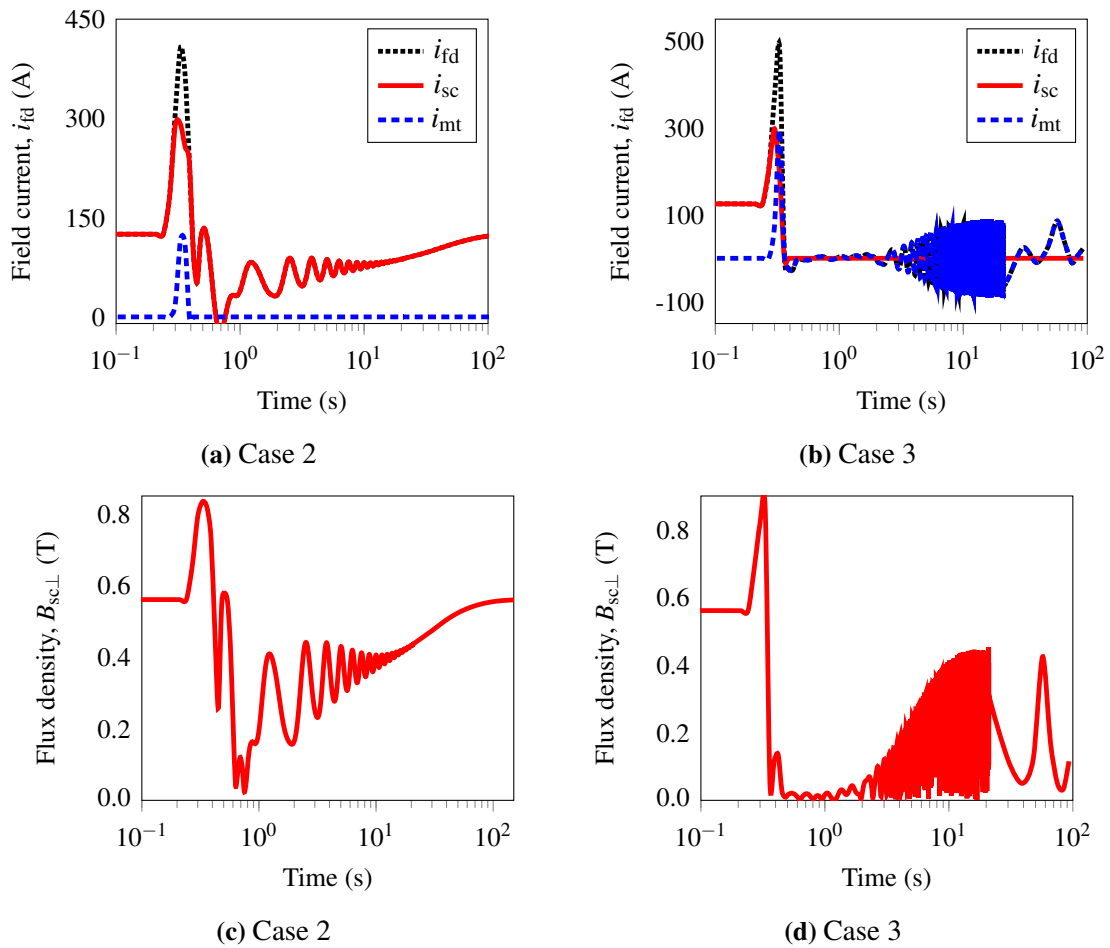
Fig. 5.8 Electrical response of the central turn of the HTS field winding during the fault and evolution of the average magnetic flux density over the winding $\bar{B}$.

In the case of a full transition, Fig. 5.7b, the resistance and temperature are never recovered and the HTS rotor is likely to be damaged (extreme case scenario 3). Figure 5.8 provides details of the distribution of current inside the HTS rotor and the evolution of the average magnetic flux density for case 2 and 3. In case 2, the machine operates in its current sharing regime during the fault; when the fault clears, the resistance of the HTS reduces quickly as discussed previously and the current flows entirely in the superconducting layers. Even though the recovery of the steady state regime of the HTS machine is dictated by the thermal response of the HTS, it is important to include the rapid evolution of the magnetic field at the field winding as shown in Fig. 5.8(b). These rapid changes affect the transient behavior of the machine as well as its recovery as the resistance increases further due to a decrease in the critical current.

5.4 Superconducting-based wind power system simulation

The following model is still on development at the moment of writing the manuscript. The results are preliminary but showing a fair response of the machine to its surroundings. Some additional works should help finalizing the sizing of the machine and its control to get a smooth power flow. The Simulink block diagram of the wind power system consisting of an HTS machine connected to the power grid through a variable-frequency full-scale power converter is shown in Fig. 5.9. The HTS-SM is connected to an infinite bus with an RMS line-to-line voltage of $V_{\mathrm{L,g}} = 4.7$ kV and an electrical frequency of $f_{\mathrm{e,g}} = 60$ Hz. The coupling impedance values R_{g} and L_{g} are chosen as a fraction of the base impedance of the grid-side system defined as $Z_{\mathrm{g,b}} = 1.4727\,[\Omega]$. The corresponding values are $R_{\mathrm{g}} = 0.01 Z_{\mathrm{g,b}}$ and $L_{\mathrm{g}} = 0.1 Z_{\mathrm{g,b}}$. The DC-link voltage $V_{\mathrm{DC}} = 8060$ is obtained based on (2.10) while considering an overvoltage factor of $k_{\mathrm{VDC}} = 1.05$. The wind turbine block is modeled through (4.1) and transformed in pu. This block includes a look-up table where the optimal rotor speed and wind velocity values are defined to obtain the reference optimal rotor speed for the control speed block. The wind incidence angle is considered zero $\beta = 0$. The field current of HTS-SM block is regulated at $i_{\mathrm{fd}} = 130$ A. A parasite load demanding 5% of the nominal power is connected in parallel at the machine terminals as a Simscape electrical requirement for convergence. The two case studies shown in Table. 5.2 are analyzed to evaluate the performance of the HTS-SM whilst monitoring power transformation throughout the wind power system.

Table 5.2 Superconducting-based wind power system case studies.

Case	Operating temperature T_{sc} K	Critical current I_{cr} A	Fitting parameter B_0 T	Simulation time t s
1	77	300	0.4	7.72
2	67	500	0.5	60
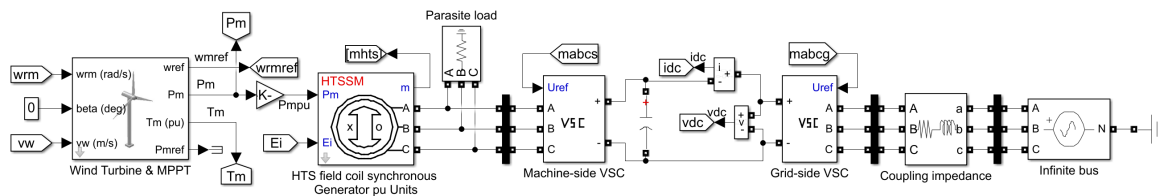
Fig. 5.9 Simscape electrical block diagram of a superconducting-based wind power system.

5.4.1 Case 1: steady state

In case 1, the critical current is lower than the field current $I_c < i_{fd}$, as shown in Fig. 5.10a. The flux density influencing the HTS coil oscillates in response to the field current behavior (Fig. 5.10b). Subsequently, power losses increase progressively, raising the field resistance and causing a temperature rise above the HTS critical temperature, as illustrated in Fig. 5.10c. Then, the superconducting state is extinguished. The simulation is stopped at $t = 7.72$ s because the operating temperature of the central HTS field coil turn raised at more than 300 K. This is a drastic response of the HTS rotor coil corresponding to an undesired quench. The interest variables of the wind power system are shown in Fig. 5.11. The wind speed remains constant, as shown in Fig. 5.11a. However, starting the simulation at exactly the proper initial conditions is difficult due to the presence of power electronics devices.
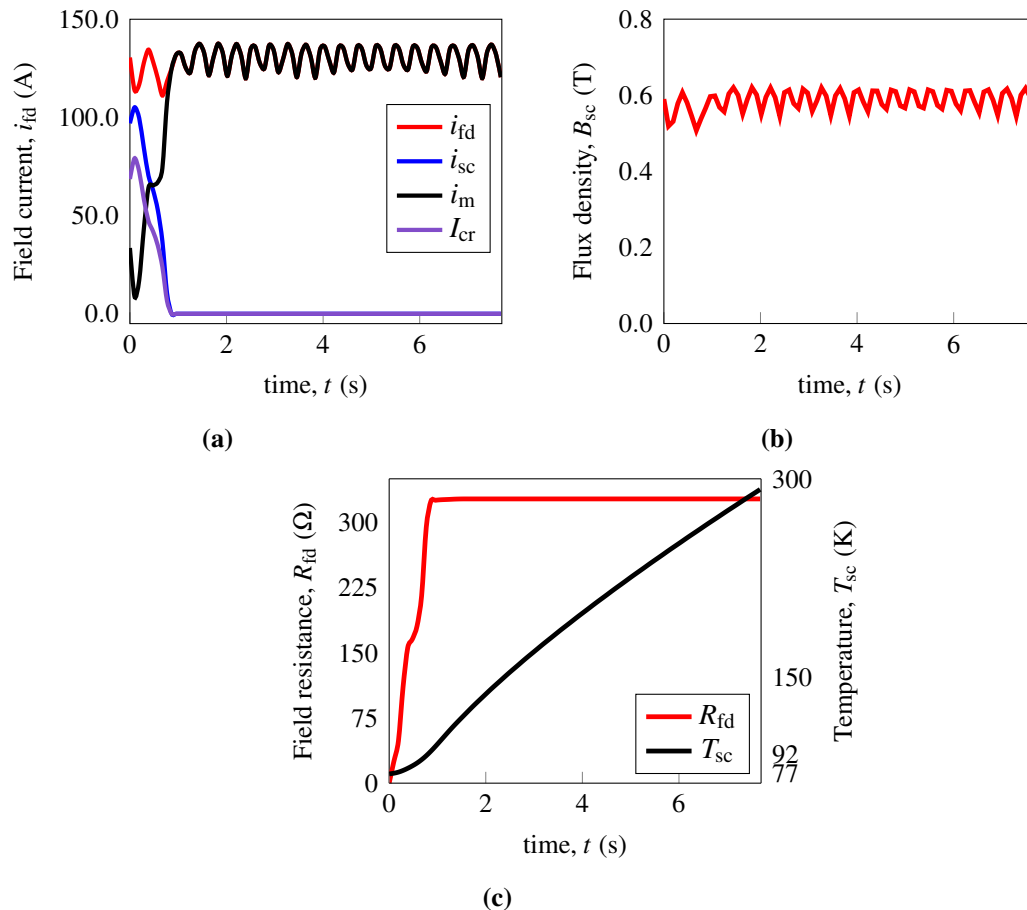
Fig. 5.10 HTS machine simulation with quench on the superconducting state. a) Field current. b) HTS field coil maximum perpendicular flux density. c) Field resistance and HTS layer temperature (Middle of stack).

Therefore, all variables shown in Fig. 5.11 present transients at the beginning of the simulation. Before the transients, the DC-link voltage presents a ripple with less than 2% of the reference DC voltage, and remains oscillating around it, as shown in Fig. 5.11b. The DC-link voltage ripple is expected to produce some noise in the reference signal to the grid-side VSC power injection. The rotor speed tracks the reference rotor speed given by the MPPT curve, as shown in Fig. 5.11c. At last, the wind power system balance is shown in Fig. 5.11d. It can be noted that the HTS-SM is delivering power to the machine-side VSC while the grid-side VSC is injecting power controlled by the DC link.
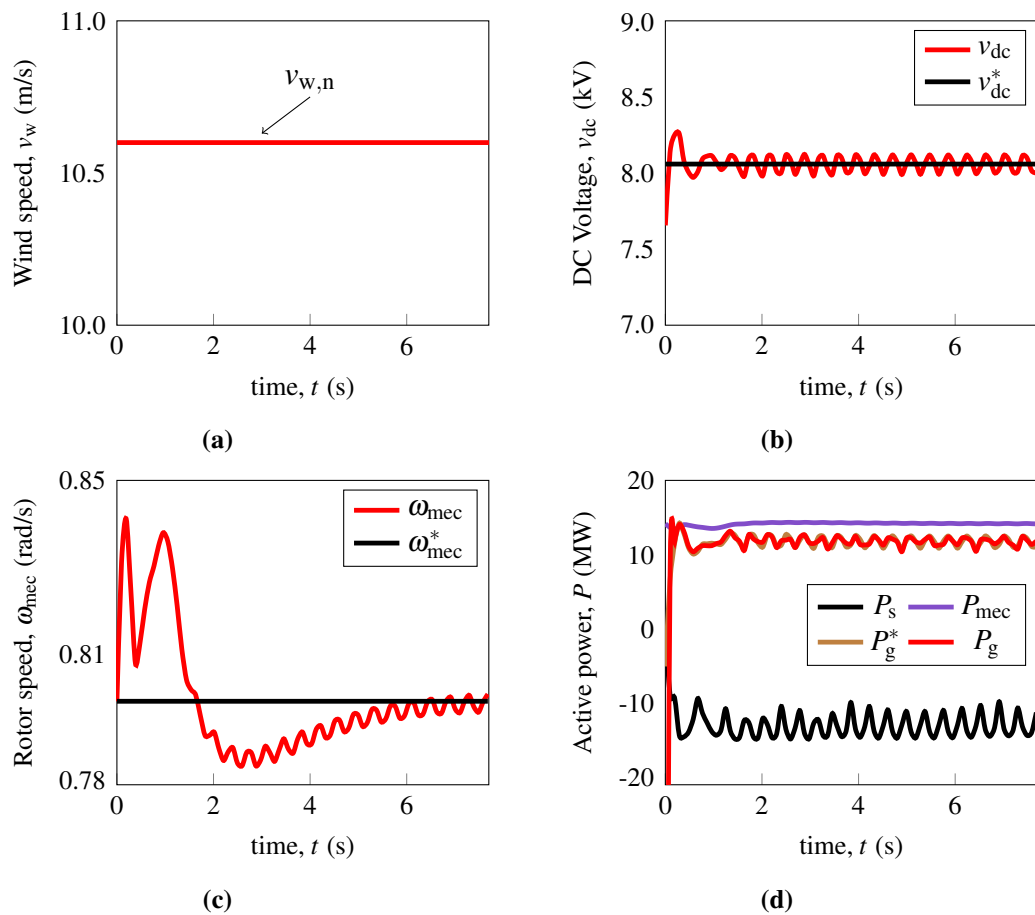
Fig. 5.11 Wind power system simulation with quench on the superconducting state. a) Wind speed input variation. b) DC-link voltage. c) Rotor speed. d) Power balance.

5.4.2 Case 2: transient

In case 2, the critical current initially falls below the field current, $I_c < i_{fd}$, as depicted in Figure 5.10a. Subsequently, the field current is stabilized at a level that maintains $I_c > i_{fd}$. Consistent with case 1, the field current exhibits similar general behavior, resulting in minimal fluctuations in the flux density affecting the HTS coil (Figure 5.10b). Despite the extremely low power losses, they do not reach zero due to oscillations in the critical current. Consequently, the field resistance fluctuates in response to these oscillations while the temperature remains at the corresponding reference value of $T_{ref} = 67$ K, as shown in Fig. 5.12c. The simulation lasts $t = 60$ s. The wind power system variables for this case are shown in Fig. 5.13. The wind speed is defined with the variations shown in Fig. 5.11a. Despite the wind speed changes, the DC-link voltage mantains its reference value with a $\Delta V_{DC} < 2\%$, as given in Fig. 5.11b.

Fig. 5.12 HTS machine simulation without quench of the superconducting state. a) Field current. b) HTS field coil maximum perpendicular flux density. c) Field resistance and HTS layer temperature (HTS stack center).
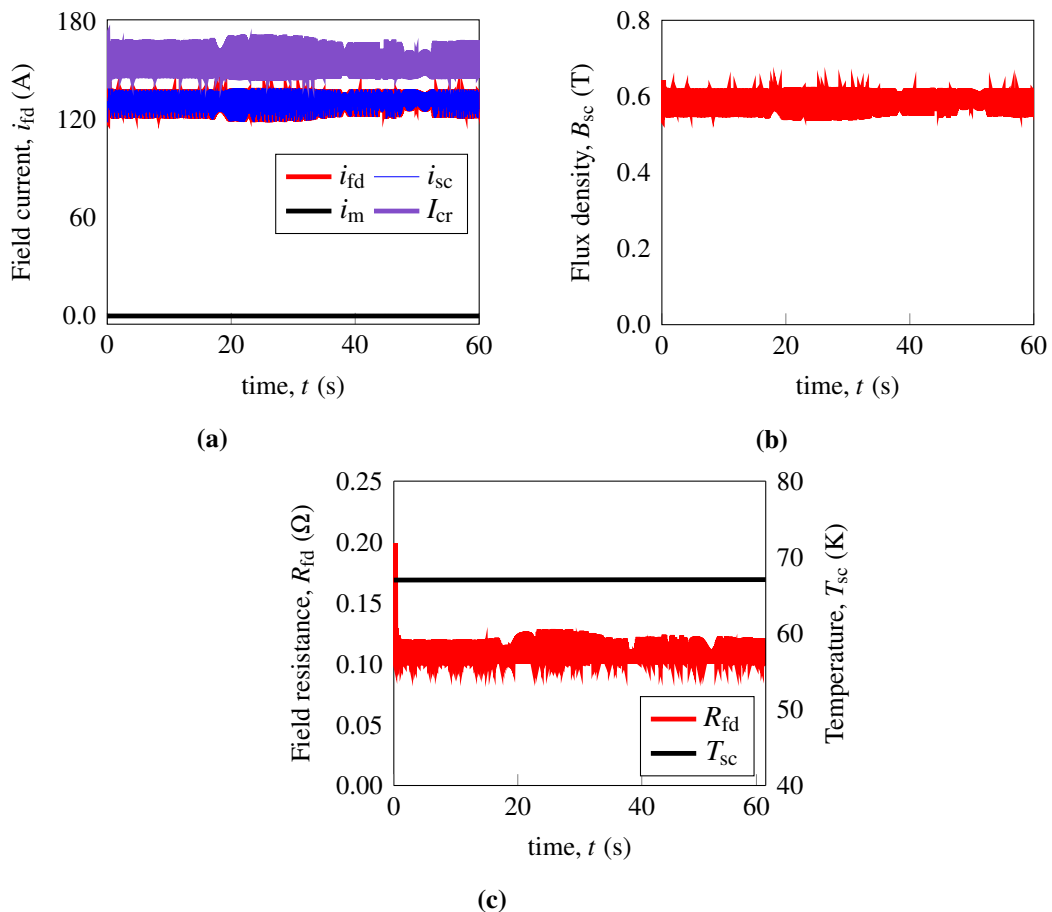
The DC-link voltage ripple produce some noise in the reference signal that controls the grid-side VSC power injection. The rotor speed effectively tracks the reference rotor speed given by the MPPT curve (Fig. 5.11c. However, rotor speed oscillations occurr throughout the simulation. They distort both machine output power and grid injected power. These oscillations are the result of a non-optimal control design in the rotor speed that are transferred to the field coil through induced currents. Further work ought to address this issue. Finally, Fig. 5.11d illustrates the power tracking as a function of the wind speed changes. Thus, the variable-frequency full-scale power converter meets one of the wind power system transformation objectives.

Fig. 5.13 Wind power system simulation without quench of the superconducting state. a) Wind speed input variation. b) DC-link voltage. c) Rotor speed. d) Power balance.
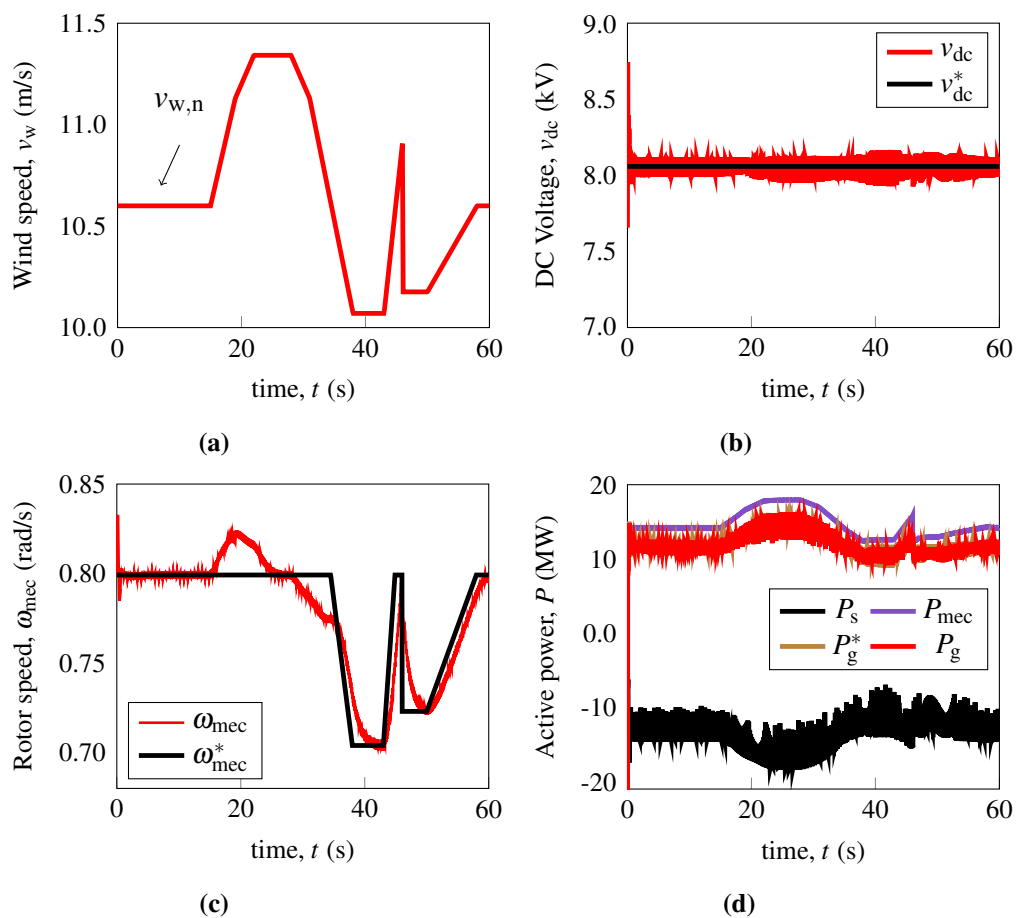
5.5   Discussion on transient stability

When there is a disruption in the system, the generator electromagnetic interactions undergo rapid changes, resulting in high currents and torques that last for a few milliseconds. During this time frame, the inertia of the turbine and generator prevents any substantial alteration in rotor speed. Therefore, it is enough to assume that the rotor speed remains constant. During a short circuit, when the stator current increases quickly, the stator's flux linkage experiences a sudden change, immediately attempting to modify the machine's main flux. First, the induced currents in both the field and the damper (or magnetic shield) windings create a strong reaction in the rotor and resist flux changes by redirecting the machine's stator winding flux to leakage paths near the air gap. This state is known as the subtransient state. Then, the induced currents in damper windings decay rapidly to zero due to their relatively large resistances, whereas the field current would tend to recover its prefault value if the field winding resistance were constant. This state is known as transient state. However, as the field winding time constant is dependent on the dynamic variation of the HTS field resistance, achieving the prefault value of the field current after the fault may delay more as a function of the operating conditions and the fault intensity. The decaying of the amplitude in the stator AC current suggests that the internal impedance of the generator is changing over time due to interactions between the armature, field, and damper windings. However, it remains constant in the steady state. Therefore, inmediatly after a fault, the generator becomes a dynamic source that can be represented with a time-changing synchronous reactance $X_s(t)$ and an internal voltage $E_i(t)$ [116]. In order to gain insight into the influence of steady-state AC armature flux on generator performance, the voltage drop across the synchronous reactance X_s can be examined in both conventional and SC machines. Moreover, it is possible to categorize the effects of this flux during fault conditions into three key states which characterize the rotor magnetic screening, i.e., into subtransient, transient, steady states represented through d-axis and q-axis synchronous reactances $X''_{d,q}$, $X'_{d,q}$, $X_{d,q}$, respectively, as shown in Fig. 5.14. But also through d-axis and q-axis subtransient $T''_{d,q}$ and transient $T'_{d,q}$ time constants. The time-varying reactance $X_s(t)$ can be calculated by dividing the open-circuit emf E_i by the short circuit stator current $I_{ac}(t)$. Dividing the emf by the appropriate reactance will give the subtransient, transient and steady-state currents. The successive effect of the three reactances leads to a gradual reduction in the short-circuit current.

The sum of the three characteristic elements including a DC component [117] can express roughly the fault current, as follows,

$$
\begin{aligned}
I_{ac}(t) = & -E_m \cos\left(\theta_e(t) + \theta_0\right) \left[\left(\frac{1}{X_d''} - \frac{1}{X_d'} \right) e^{-t/T_d''} + \left(\frac{1}{X_d'} - \frac{1}{X_d} \right) e^{-t/T_d'} + \frac{1}{X_d} \right] \\
& + \frac{E_m}{2} e^{-t/T_a} \left[\left(\frac{1}{X_d''} + \frac{1}{X_q''} \right) \cos\left(\theta_0\right) + \left(\frac{1}{X_d''} - \frac{1}{X_q''} \right) \cos\left(2\theta_e(t) + \theta_0\right) \right]
\end{aligned}
\tag{5.1}
$$

where I_{ac} is the short circuit phase current; E_m is the back emf of the stator winding; X_d'', X_d', X_d are the subtransient, transient and steady-state d-axis reactances; X_q'' and X_q are the subtransient and steady-state q-axis reactances; T_d'' and T_d' are the subtransient and transient d-axis time constants; T_a is the stator time constant; θ_e and θ_0 are the electrical angular displacement and the angle between the d-axis and the a-axis at time $t = 0$. In order to determine T_d'' during a short circuit condition, it is necessary to incorporate the damper winding resistance R_{kd} (which is "active" in the subtransient state) into the branch containing X_{kd} as seen in Fig. 5.14a.

The same procedure can be applied to determine T_d' but by considering that the only "active" resistance corresponds to the field winding resistance R_{fd}. However, depending on the operational condition of the SC machine, R_{fd} may vary and its corresponding value could be either $R_{fd} \ll R_s$ (Fig. 5.14b), $R_{fd} \approx R_s$ (Fig. 5.14c) or $R_{fd} \gg R_s$ (Fig. 5.14d).

(a) Subtransient period.

(b) Transient period $R_{fd} \ll R_s$.

(c) Transient period $R_{fd} \approx R_s$.

(d) Transient period $R_{fd} \gg R_s$.
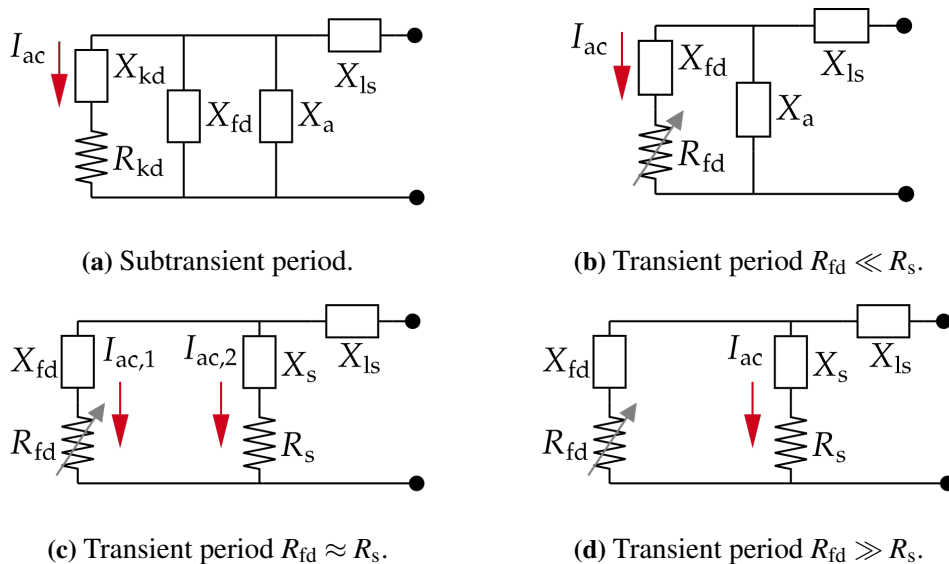
Fig. 5.14 Representation of key characteristic states in a fault condition

It can be seen then that the stator fault current behavior, which impacts the field current behavior, becomes complex to analyze, so a different approach from the traditional analysis must be considered in order to study the transient stability of such machines connected to the power grid.

5.6 Conclusion

A lumped-parameter model including the thermal, electric and magnetic physics of an HTS field synchronous machine has been presented and simulated in this work. To achieve this goal, a 15 MW HTS field coil SM design for wind power applications was developed and simulated under no-load conditions using the FEM. The rated design parameters was validated and a FEA was conducted to establish a basis for the proposed MEC model. The machine dimensions were used to calculate the lumped parameters for the electrical, thermo-electrical, and magnetic circuits conforming the HTS field coil thermoelectromagnetic model. Then, a dq0 frame-of-reference SM model was coupled through the HTS winding nonlinear resistance in the Simulink software. Subsequently, a transient analysis was performed in the Simscape electrical environment for three different case studies of the proposed HTS machine.

This machine was connected to an infinite bus and subjected to a transient three-phase fault condition. The first case, considered as a reference, was a conventional machine with the same electrical parameters as the 15 MW HTS machine design but with a constant field winding resistance. The second and third cases considered the nonlinear HTS field winding resistance under non-quench and quench conditions, respectively. Under such transient analysis, the maximum value of the magnetic flux density on the field winding for a component perpendicular to the tape surface $B_{\mathrm{sc}\perp}$ (the most stringent magnetic condition of the HTS winding) was computed with the proposed MEC model. This model facilitates the inclusion of diverse coil configurations, providing flexibility in terms of building the reluctance mesh of the MEC to account for the performance of the HTS winding. A set of fitted parameters allows for the addition of the non-uniform distribution of current density in the superconducting coils. Therefore, the MEC model represents a one step forward for studying complex transient regimes with duration of several power cycles instead of using the FEM. Indeed, the FEM are impractical for analyzing this type of studies due to the modeling complexity, memory and time constraints. Then, the proposed model methodology is relevant for conducting transient stability studies of interconnected HTS field coil synchronous machines with power systems. However, this approach should be carried out on the basis of the coil shape and the tape technology. The transient analysis results, considering the

stator winding transient magnetic behavior, shown the hierarchy of the thermal response on the overall system behavior. It was shown that the dynamic response of the HTS machine is dictated by the thermal response of the HTS. Therefore, the time constant of the HTS machine differs significantly from the conventional machine and should be considered in the overall stability of the power grid. These results present an agreement with the short circuit tests performed on a real air-core HTS hybrid SM given in [83], where the measures of the field current indicate that the corresponding transient lasts longer than anticipated compared with a traditional machine. Additionally, one of the critical results of the analysis was the damping circuits behavior in HTS rotating machines. The importance of including these circuits, such as short-circuited bars or electromagnetic screens, allows the shielding of the HTS field winding from the rapid changes in the magnetic main flux due to the machine transients. They also dissipate energy, which helps to protect the HTS winding from damage. Therefore, a suitable design and modeling of the damping circuits are essential for the safe and reliable operation of HTS synchronous generators connected to the grid.

Furthermore, a superconducting-based wind power system was simulated and analyzed. The integration of a variable-frequency full-scale power converter between the HTS-SM and the power grid was done. The wind power system achieve two main objectives: 1) Convert the variable frequency signals from the stator windings into a constant frequency at the output of the conversion system. 2) Maintains the HTS field current at a permissible value defined by the mode of operation of the system connected and the critical parameters of the superconductor. However, due to their inherent characteristics, a deeper understanding between the interactions of the HTS field coil SMs with their associated power electronics and control systems is needed to satisfy power system requirements and ensure reliable operation. This is because HTS-SMs can present low inertia and power balancing issues which can lead to stability problems [15, 118].

5.7   Future work

Further research will focus on optimizing the control design of the presented superconducting-based wind power system. The modeling of superconducting machines at various power outputs in IEEE test feeders with a limited number of nodes is planned. Power converters and power devices will be incorporated as needed for specific applications or analyses.

Additionally, the HTS field winding magnetic model will be enhanced to include saturation and harmonics effects, but also, considering the machine rotation in the MEC model to achieve more realistic results and improve the estimation of the HTS winding resistance. Specific FEM analysis will be required for different coil shapes and stack configurations to determine the sets of k function parameters. Consequently, a database of front functions for various stack topologies and their corresponding analyses will be developed for future work.

References

[1] U.S. Energy Information Administration (EIA). "International Energy Outlook 2021, https://www.eia.gov/outlooks/ieo/." (2021).

[2] NREL. "2022 Electricity ATB Technologies and Data Overview." (2022), [Online]. Available: {https://atb.nrel.gov/electricity/2022/index}.

[3] C. Lewis, ""Direct drive superconducting wind generators"," in *Wind Power Generation and Wind Turbine Design*, WIT Press, 2010, pp. 303–331. DOI: 10.2495/978-1-84564-205-1/09.

[4] M. Rezkalla, M. Pertl, and M. Marinelli, "Electric power system inertia: Requirements, challenges and solutions," *Electrical Engineering*, vol. 100, no. 4, pp. 2677–2693, Aug. 2018. DOI: 10.1007/s00202-018-0739-z.

[5] J. Fang, H. Li, Y. Tang, and F. Blaabjerg, "On the inertia of future more-electronics power systems," *IEEE Journal of Emerging and Selected Topics in Power Electronics*, vol. 7, no. 4, pp. 2130–2146, Dec. 2019. DOI: 10.1109/jestpe.2018.2877766.

[6] General Electric. "Haliade-X offshore wind turbineRecord-setting offshore wind technology, https://www.ge.com/renewableenergy/wind-energy/offshore-wind/haliade-x-offshore-turbine." (2023).

[7] K. S. Stegen, "Heavy rare earths, permanent magnets, and renewable energies: An imminent crisis," *Energy Policy*, vol. 79, pp. 1–8, Apr. 2015. DOI: 10.1016/j.enpol.2014.12.015.

[8] International Renewable Energy Agency, *"Global Energy Transformation: A roadmap to 2050"*.

[9] IRENA, Global Energy Transformation, ""A Roadmap to 2050"," *Abu Dhabi: International Renewable Energy Agency*, 2018.

[10] REN21, ""Renewables 2018 Global Status Report"," Renewable Energy Policy Network for the 21st Century, Tech. Rep., 2018.

[11] L. Wang, J. Wei, X. Wang, and X. Zhang, ""The development and prospect of offshore wind power technology in the world"," in *2009 World Non-Grid-Connected Wind Power and Energy Conference*, IEEE, 2009. DOI: 10.1109/wnwec.2009.5335761.

[12] C. Lewis and J. Muller, ""A Direct Drive Wind Turbine HTS Generator"," in *2007 IEEE Power Engineering Society General Meeting*, IEEE, 2007. DOI: 10.1109/pes.2007.386069.

[13] A. B. Abrahamsen *et al.*, "Superconducting wind turbine generators," *Superconductor Science and Technology*, vol. 23, no. 3, p. 034019, 2010. DOI: 10.1088/0953-2048/23/3/034019.

[14]   X. Song *et al.*, ""Designing and Basic Experimental Validation of the World's First MW-Class Direct-Drive Superconducting Wind Turbine Generator"," *IEEE Transactions on Energy Conversion*, p. 1, 2019. DOI: 10.1109/TEC.2019.2927307.

[15]   S. K. Moore, ""Rough seas for the superconducting wind turbine: To keep offshore turbines light, engineers look beyond superconductors to a new permanent-magnet tech"," *IEEE Spectrum*, vol. 55, no. 8, pp. 32–39, Aug. 2018. DOI: 10.1109/MSPEC. 2018.8423581.

[16]   G. Komurgoz and T. Gundogdu, ""Comparison of salient pole and Permanent Magnet Synchronous Machines designed for wind turbines"," in *2012 IEEE Power Electronics and Machines in Wind Applications*, IEEE, 2012. DOI: 10.1109/pemwa.2012. 6316381.

[17]   R. Sharma, *Superconductivity*. Springer International Publishing, 2015. DOI: 10. 1007/978-3-319-13713-1.

[18]   A. M. Forrest, "Meissner and ochsenfeld revisited," *European Journal of Physics*, vol. 4, no. 2, pp. 117–120, Apr. 1983. DOI: 10.1088/0143-0807/4/2/011.

[19]   V. Kozhevnikov, "Meissner effect: History of development and novel aspects," *Journal of Superconductivity and Novel Magnetism*, vol. 34, no. 8, pp. 1979–2009, Jul. 2021. DOI: 10.1007/s10948-021-05925-8.

[20]   M Cyrot, "Ginzburg-landau theory for superconductors," *Reports on Progress in Physics*, vol. 36, no. 2, pp. 103–158, Feb. 1973. DOI: 10.1088/0034-4885/36/2/001.

[21]   B. B. Goodman, "Type II superconductors," *Reports on Progress in Physics*, vol. 29, no. 2, pp. 445–487, Jul. 1966. DOI: 10.1088/0034-4885/29/2/302.

[22]   J. G. Bednorz and K. A. Muller, "Possible highT c superconductivity in the Ba-La-Cu-O system," *Zeitschrift fur Physik B Condensed Matter*, vol. 64, no. 2, pp. 189–193, Jun. 1986. DOI: 10.1007/bf01303701.

[23]   M. K. Wu *et al.*, "Superconductivity at 93 k in a new mixed-phase Y-Ba-Cu-O compound system at ambient pressure," *Phys. Rev. Lett.*, vol. 58, pp. 908–910, 1987. DOI: 10.1103/PhysRevLett.58.908.

[24]   NASA, Glenn Research center. "https://www1.grc.nasa.gov/aeronautics/eap/technology/soft-magnetic-materials/superconducting-wire-development/." (2023).

[25]   Sumitomo Electric. "https://sumitomoelectric.com/rd/power-systems-rd-center." (2023).

[26]   SuperPower Inc. "https://www.superpower-inc.com/specification.aspx." (2023).

[27]   Furukawa electric group. "https://www.furukawa.co.jp/en/rd/superconduct/smartgrid.html." (2023).

[28]   SuperOx Japan LLC. "https://www.superoxjapan.com/en/products/." (2023).

[29]   S. C. Wimbush and N. M. Strickland, "A public database of high-temperature superconductor critical current data," *IEEE Transactions on Applied Superconductivity*, vol. 27, no. 4, pp. 1–5, Jun. 2017. DOI: 10.1109/tasc.2016.2628700.

[30]   J. J. Pérez-Chávez, F. Trillaud, L. M. Castro, L. Quéval, A. Polasek, and R. de Andrade Junior, ""Generic Model of Three-Phase (RE)BCO Resistive Superconducting Fault Current Limiters for Transient Analysis of Power Systems"," *IEEE Transactions on Applied Superconductivity*, vol. 29, no. 6, pp. 1–11, Sep. 2019, ISSN: 2378-7074. DOI: 10.1109/TASC.2019.2891229.

[31] F. Trillaud, G. dos Santos, and G. G. Sotelo, "Essential material knowledge and recent model developments for REBCO-coated conductors in electric power systems," *Materials*, vol. 14, no. 8, p. 1892, Apr. 2021. DOI: 10.3390/ma14081892.

[32] S. S. Kalsi, *"Applications of High Temperature Superconductors to Electric Power Equipment"*. JOHN WILEY and SONS INC, 2011, 332 pp., ISBN: 0470167688.

[33] X. Zhang *et al.*, ""Study of Critical Current and n-Values of 2G HTS Tapes: Their Magnetic Field-Angular Dependence"," vol. 31, pp. 3847–3854, 2018, ISSN: 1557-1939. DOI: 10.1007/s10948-018-4678-8.

[34] Victoria University of Wellington. "https://htsdb.wimbush.eu/." (2023).

[35] G. G. Sotelo, M. Carrera, J. Lopez-Lopez, and X. Granados, ""H-Formulation FEM Modeling of the Current Distribution in 2G HTS Tapes and Its Experimental Validation Using Hall Probe Mapping"," *IEEE Transactions on Applied Superconductivity*, vol. 26, no. 8, pp. 1–10, 2016. DOI: 10.1109/tasc.2016.2591825.

[36] B. C. Robert, M. U. Fareed, and H. S. Ruiz, "How to choose the superconducting material law for the modelling of 2g-HTS coils," *Materials*, vol. 12, no. 17, p. 2679, Aug. 2019. DOI: 10.3390/ma12172679.

[37] S. Kalsi, K. Weeber, H. Takesue, C. Lewis, H.-W. Neumueller, and R. Blaugher, "Development status of rotating machines employing superconducting field windings," *Proceedings of the IEEE*, vol. 92, no. 10, pp. 1688–1704, Oct. 2004. DOI: 10.1109/jproc.2004.833676.

[38] K. S. Haran *et al.*, "High power density superconducting rotating machines—development status and technology roadmap," *Superconductor Science and Technology*, vol. 30, no. 12, p. 123 002, Nov. 2017. DOI: 10.1088/1361-6668/aa833e.

[39] M. Frank, J. Frauenhofer, P. van Hasselt, W. Nick, H.-W. Neumueller, and G. Nerowski, "Long-term operational experience with first siemens 400 kW HTS machine in diverse configurations," *IEEE Transactions on Appiled Superconductivity*, vol. 13, no. 2, pp. 2120–2123, Jun. 2003. DOI: 10.1109/tasc.2003.813013.

[40] R. Fair, C. Lewis, J. Eugene, and M. Ingles, "Development of an HTS hydroelectric power generator for the hirschaid power station," *Journal of Physics: Conference Series*, vol. 234, no. 3, p. 032 008, Jun. 2010. DOI: 10.1088/1742-6596/234/3/032008.

[41] A. M. US, S. N. JP, F. S. DE, B. W. DE, and A. W. US, *Status of development and field test experience with high-temperature superconducting power equipment.* ., 2010.

[42] P. Tixador, "Development of superconducting power devices in europe," *Physica C: Superconductivity and its Applications*, vol. 470, no. 20, pp. 971–979, Nov. 2010. DOI: 10.1016/j.physc.2010.05.014.

[43] M. Frank *et al.*, ""High-Temperature Superconducting Rotating Machines for Ship Applications"," *IEEE Transactions on Applied Superconductivity*, vol. 16, no. 2, pp. 1465–1468, 2006. DOI: 10.1109/tasc.2005.864263.

[44] J. Frauenhofer, M. Kaufhold, P. Kummeth, G. Nerowski, and W. Nick, ""High-temperature-superconducting machines- a high-technology step for large rotating electric machines"," in *International Symposium on Power Electronics, Electrical Drives, Automation and Motion, 2006. SPEEDAM 2006.*, IEEE, 2006. DOI: 10.1109/speedam.2006.1649802.

[45] P. K. Ghoshal, T. A. Coombs, R. Fair, and A. M. Campbell, "Experimental set up to measure AC losses of HTS in rotating magnetic field," *IEEE Transactions on Applied Superconductivity*, vol. 17, no. 2, pp. 3199–3202, Jun. 2007. DOI: 10.1109/tasc.2007. 897419.

[46] M. Zhang *et al.*, "AC loss estimation of HTS armature windings for electric machines," *IEEE Transactions on Applied Superconductivity*, vol. 23, no. 3, pp. 5 900 604– 5 900 604, Jun. 2013. DOI: 10.1109/tasc.2013.2239341.

[47] L. Queval and H. Ohsaki, ""AC Losses of a Grid-Connected Superconducting Wind Turbine Generator"," *IEEE Transactions on Applied Superconductivity*, vol. 23, no. 3, pp. 5 201 905–5 201 905, 2013. DOI: 10.1109/tasc.2013.2251252.

[48] S. Kalsi, "Development status of superconducting rotating machines," in *2002 IEEE Power Engineering Society Winter Meeting. Conference Proceedings (Cat. No.02CH37309)*, IEEE. DOI: 10.1109/pesw.2002.985030.

[49] H. Matsuzaki *et al.*, "HTS bulk pole-field magnets motor with a multiple rotor cooled by liquid nitrogen," *IEEE Transactions on Applied Superconductivity*, vol. 17, no. 2, pp. 1553–1556, Jun. 2007. DOI: 10.1109/tasc.2007.898488.

[50] J. M. Pina *et al.*, ""Research and Development of Alternative Concepts in HTS Machines"," *IEEE Transactions on Applied Superconductivity*, vol. 21, no. 3, pp. 1141– 1145, 2011. DOI: 10.1109/tasc.2010.2094594.

[51] M. Zhang, W. Wang, Y. R. Chen, and T. Coombs, ""Design Methodology of HTS Bulk Machine for Direct-Driven Wind Generation"," *IEEE Transactions on Applied Superconductivity*, vol. 22, no. 3, pp. 5 201 804–5 201 804, 2012. DOI: 10.1109/tasc. 2011.2179696.

[52] C. Oberly, ""Lightweight superconducting generators for mobile military platforms"," in *IEEE Power Engineering Society General Meeting*, IEEE, 2006. DOI: 10.1109/pes. 2006.1709644.

[53] P. Elhaminia, M. Yazdanian, M. R. Zolghadri, and M. Fardmanesh, ""An analytical approach for optimal design of rotor iron for superconducting synchronous machine"," in *Proc. IECON 2011 - 37th Annual Conf. of the IEEE Industrial Electronics Society*, Nov. 2011, pp. 1741–1745. DOI: 10.1109/IECON.2011.6119569.

[54] H. Kim *et al.*, ""Design of Damper to Protect the Field Coil of an HTS Synchronous Motor"," *IEEE Transactions on Applied Superconductivity*, vol. 19, no. 3, pp. 1683– 1686, 2009. DOI: 10.1109/tasc.2009.2017842.

[55] R. Shafaei and F. Amirkhanloo, "Design of a combined screening and damping layer for a 10-MW-class wind turbine HTS synchronous generator," *IEEE Transactions on Applied Superconductivity*, vol. 28, no. 6, pp. 1–12, Sep. 2018. DOI: 10.1109/tasc. 2018.2837007.

[56] G. Klaus, M. Wilke, J. Frauenhofer, W. Nick, and H.-W. Neumuller, ""Design Challenges and Benefits of HTS Synchronous Machines"," in *2007 IEEE Power Engineering Society General Meeting*, IEEE, 2007. DOI: 10.1109/pes.2007.385756.

[57] Y. Liu, R. Qu, and J. Wang, "Comparative analysis on superconducting direct-drive wind generators with iron teeth and air-gap winding," *IEEE Transactions on Applied Superconductivity*, vol. 24, no. 3, pp. 1–5, Jun. 2014. DOI: 10.1109/tasc.2013. 2292309.

[58] J Frauenhofer, J Grundmann, G Klaus, and W Nick, ""Basic concepts, status, opportunities, and challenges of electrical machines utilizing high-temperature superconducting (HTS) windings"," *Journal of Physics: Conference Series*, vol. 97, p. 012 189, 2008. DOI: 10.1088/1742-6596/97/1/012189.

[59] A. Bergen *et al.*, ""Design and in-field testing of the world's first ReBCO rotor for a 3.6 MW wind generator"," *Superconductor Science and Technology*, vol. 32, no. 12, p. 125 006, 2019. DOI: 10.1088/1361-6668/ab48d6.

[60] O Tuvdensuren, H. J. Sung, B. S. Go, T. T. Le, M Park, and I. K. Yu, "Structural design and heat load analysis of a flux pump-based HTS module coil for a large-scale wind power generator," *Journal of Physics: Conference Series*, vol. 1054, p. 012 084, Jul. 2018. DOI: 10.1088/1742-6596/1054/1/012084.

[61] R. Qu, Y. Liu, and J. Wang, "Review of superconducting generator topologies for direct-drive wind turbines," *IEEE Transactions on Applied Superconductivity*, vol. 23, no. 3, pp. 5 201 108–5 201 108, Jun. 2013. DOI: 10.1109/tasc.2013.2241387.

[62] S. S. Kalsi, ""Superconducting Wind Turbine Generator Employing MgB_2 Windings Both on Rotor and Stator"," *IEEE Transactions on Applied Superconductivity*, vol. 24, no. 1, pp. 47–53, 2014. DOI: 10.1109/tasc.2013.2291275.

[63] Y. Xu, N. Maki, and M. Izumi, ""Study of Key Parameters and Cryogenic Vessel Structure of 10-MW Salient-Pole Wind Turbine HTS Generators"," *IEEE Transactions on Applied Superconductivity*, vol. 25, no. 2, pp. 1–6, 2015. DOI: 10.1109/tasc.2014.2368118.

[64] J. H. Kim *et al.*, "Economic analysis of a 1.5-MW-class HTS synchronous machine considering various commercial 2g CC tapes," *IEEE Transactions on Applied Superconductivity*, vol. 26, no. 4, pp. 1–5, Jun. 2016. DOI: 10.1109/tasc.2016.2521408.

[65] X. Song *et al.*, "Ground testing of the world's first MW-class direct-drive superconducting wind turbine generator," *IEEE Transactions on Energy Conversion*, vol. 35, no. 2, pp. 757–764, Jun. 2020. DOI: 10.1109/tec.2019.2960255.

[66] M. Rosu, P. Zhou, D. Lin, D. M. Ionel, and M. Popescu, *"Multiphysics Simulation by Design for Electrical Machines, Power Electronics and Drives"*. Wiley John and Sons, Mar. 9, 2018, 320 pp., ISBN: 1119103444.

[67] B. Dutoit, F. Grilli, and F. Sirois, *Numerical Modeling of Superconducting Applications*. WORLD SCIENTIFIC, Nov. 2022. DOI: 10.1142/13282.

[68] F. Grilli, E. Pardo, A. Stenvall, D. N. Nguyen, W. Yuan, and F. Gomory, "Computation of losses in HTS under the action of varying magnetic fields and currents," *IEEE Transactions on Applied Superconductivity*, vol. 24, no. 1, pp. 78–110, Feb. 2014. DOI: 10.1109/tasc.2013.2259827.

[69] F. Grilli, "Numerical modeling of HTS applications," *IEEE Transactions on Applied Superconductivity*, pp. 1–1, 2016. DOI: 10.1109/tasc.2016.2520083.

[70] B. Shen, F. Grilli, and T. Coombs, "Review of the AC loss computation for HTS using *h* formulation," *Superconductor Science and Technology*, vol. 33, no. 3, p. 033 002, Feb. 2020. DOI: 10.1088/1361-6668/ab66e8.

[71] G. Meunier, Y. L. Floch, and C. Guerin, "A nonlinear circuit coupled $t - t_0 - \phi$ formulation for solid conductors," *IEEE Transactions on Magnetics*, vol. 39, no. 3, pp. 1729–1732, May 2003. DOI: 10.1109/tmag.2003.810200.

[72] F. Grilli *et al.*, "Finite-element method modeling of superconductors: From 2-d to 3-d," *IEEE Transactions on Appiled Superconductivity*, vol. 15, no. 1, pp. 17–25, Mar. 2005. DOI: 10.1109/tasc.2004.839774.

[73] C. R. Vargas-Llanos, S. Lengsfeld, and F. Grilli, "T-a formulation for the design and AC loss calculation of a superconducting generator for a 10 MW wind turbine," *IEEE Access*, vol. 8, pp. 208 767–208 778, 2020. DOI: 10.1109/access.2020.3038058.

[74] F. Huber, W. Song, M. Zhang, and F. Grilli, "The t-a formulation: An efficient approach to model the macroscopic electromagnetic behaviour of HTS coated conductor applications," *Superconductor Science and Technology*, vol. 35, no. 4, p. 043 003, Mar. 2022. DOI: 10.1088/1361-6668/ac5163.

[75] G. dos Santos, B. M. O. Santos, F. Sass, F. G. dos Reis Martins, G. G. Sotelo, and R. de Andrade Junior, "J-a formulation: A finite element methodology for simulating superconducting devices," *Superconductivity*, vol. 6, p. 100 049, Jun. 2023. DOI: 10.1016/j.supcon.2023.100049.

[76] E. Berrospe-Juarez, F. Trillaud, V. M. R. Zermeño, and F. Grilli, ""Advanced electromagnetic modeling of large-scale high-temperature superconductor systems based on H and T-A formulations"," *Superconductor Science and Technology*, vol. 34, no. 4, p. 044 002, 2021. DOI: 10.1088/1361-6668/abde87.

[77] R. Brambilla, F. Grilli, L. Martini, M. Bocchi, and G. Angeli, "A finite-element method framework for modeling rotating machines with superconducting windings," *IEEE Transactions on Applied Superconductivity*, vol. 28, no. 5, pp. 1–11, 2018. DOI: 10.1109/tasc.2018.2812884.

[78] L. Quéval, M. Sekino, and H. Ohsaki, ""A Coupled FE Phase-Domain Model for Superconducting Synchronous Machine"," *IEEE Transactions on Applied Superconductivity*, vol. 22, no. 3, pp. 5 200 804–5 200 804, 2012. DOI: 10.1109/tasc.2011.2177621.

[79] K. Sivasubramaniam *et al.*, "Performance of an hts generator field coil under system fault conditions," *IEEE Transactions on Applied Superconductivity*, vol. 16, no. 4, pp. 1971–1975, 2006. DOI: 10.1109/tasc.2006.881814.

[80] S. D. Umans, "Transient performance of a high-temperature-superconducting generator," in *2009 IEEE International Electric Machines and Drives Conference*, IEEE, 2009. DOI: 10.1109/iemdc.2009.5075245.

[81] R. Shafaie and M. Kalantar, "Transient performance of a large scale wind turbine HTS synchronous generator under short circuit conditions," in *2014 5th Conference on Thermal Power Plants (CTPP)*, IEEE, Jun. 2014. DOI: 10.1109/ctpp.2014.7040702.

[82] S.-J. Jung *et al.*, "Stator winding fault influence on the field coil of a 10 MW superconducting synchronous generator," *IEEE Transactions on Applied Superconductivity*, vol. 23, no. 3, pp. 5 200 104–5 200 104, Jun. 2013. DOI: 10.1109/tasc.2012.2232334.

[83] W. O. S. Bailey, Y. Yang, C. Beduz, and K. F. Goddard, "Short circuit tests on a coreless HTS synchronous generator," *IEEE Transactions on Applied Superconductivity*, vol. 23, no. 3, pp. 5 201 505–5 201 505, Jun. 2013. DOI: 10.1109/tasc.2013.2244196.

[84] X. Song, D. Liu, H. Polinder, N. Mijatovic, J. Holboll, and B. B. Jensen, "Short circuits of a 10-MW high-temperature superconducting wind turbine generator," *IEEE Transactions on Applied Superconductivity*, vol. 27, no. 4, pp. 1–5, 2017. DOI: 10.1109/tasc.2017.2656623.

[85] M. H. Rashid, *Power Electronics Handbook (Academic Press Series in Engineering)*. Academic Press, 2001, p. 895, ISBN: 9780125816502.

[86] N. Mohan, T. M. Undeland, and W. P. Robbins, *Power Electronics, Converters, Applications, and Design*. Wiley, 2002, p. 824, ISBN: 9780471226932.

[87] S. Bacha, I. Munteanu, and A. I. Bratcu, *Power Electronic Converters Modeling and Control with Case Studies, with Case Studies*. Springer, p. 477, ISBN: 9781447154778.

[88] A. Yazdani, *Voltage-sourced converters in power systems, modeling, control, and applications*. IEEE Press/John Wiley, 2010, p. 451, ISBN: 9780470521564.

[89] O. Anaya-Lara, J. O. Tande, K. Uhlen, and K. Merz, *"Offshore Wind Energy Technology"*. John Wiley and Sons Inc, 2018, 456 pp., ISBN: 1119097762.

[90] L. Queval, ""Modeling and Simulation of Grid-connected Superconducting Wind Turbine Generators"," Ph.D. dissertation, Department of Advanced Energy, University of Tokyo, 2012.

[91] O. Anaya-Lara, *Offshore Wind Energy Generation Control Protection And Integration To Electrical Systems*. John Wiley and Sons Inc, 2014, ISBN: 9781118539620.

[92] L. M. Castro, D. Guillen, and F. Trillaud, "On short-circuit current calculations including superconducting fault current limiters (ScFCLs)," *IEEE Transactions on Power Delivery*, vol. 33, no. 5, pp. 2513–2523, 2018. DOI: 10.1109/tpwrd.2018.2800732.

[93] J. Rhyner, ""Magnetic properties and AC-losses of superconductors with power law current—voltage characteristics"," *Physica C: Superconductivity*, vol. 212, no. 3-4, pp. 292–300, 1993.

[94] W. T. B. de Soua, ""Transient simulations of superconducting fault current limiters"," Ph.D. dissertation, Federal University of Rio de Janeiro, 2014.

[95] W. T. B. de Sousa, O. Näckel, and M. Noe, ""Transient Simulations of an Air-Coil SFCL"," *IEEE Transactions on Applied Superconductivity*, vol. 24, no. 4, pp. 1–7, 2014. DOI: 10.1109/TASC.2014.2311396.

[96] B. Lukasik, K. F. Goddard, and J. K. Sykulski, "Finite element assisted method of estimating equivalent circuit parameters for a superconducting synchronous generator with a coreless rotor," *IEEE Transactions on Magnetics*, vol. 45, no. 3, pp. 1226–1229, 2009. DOI: 10.1109/tmag.2009.2012572.

[97] M. L. Bash and S. D. Pekarek, "Modeling of salient-pole wound-rotor synchronous machines for population-based design," *IEEE Transactions on Energy Conversion*, vol. 26, no. 2, pp. 381–392, Jun. 2011. DOI: 10.1109/tec.2011.2105874.

[98] H. Karmaker and E. Chen, ""Design concepts for a direct drive wind generator using new superconductors"," in *2015 IEEE Electrical Power and Energy Conference (EPEC)*, IEEE, 2015. DOI: 10.1109/epec.2015.7379921.

[99] SuperPower Inc, *2G HTS wire, https://www.superpower-inc.com/specification.aspx*, 2022.

[100] A. W. Zimmermann and S. M. Sharkh, ""Design of a 1 MJ/100 kW high temperature superconducting magnet for energy storage"," 2020, ISSN: 2352-4847. DOI: https://doi.org/10.1016/j.egyr.2020.03.023.

[101] G. Evan *et al.*, ""Definition of the IEA 15-Megawatt Offshore Reference Wind"," Golden, CO: National Renewable Energy Laboratory., Tech. Rep., 2020.

[102] T. A. L. Lipo, *"Introduction to AC Machine Design"*. John Wiley and Sons, 2017, 538 pp., ISBN: 1119352169.

[103] J. Pyrhonen, *Design of rotating electrical machines*. Wiley, 2014, p. 584, ISBN: 9781118581575.

[104] I. Boldea, *"Synchronous Generators"*. CRC Press, 2015, ISBN: 9781498723558.

[105] T. de Paula Machado Bazzo, V. de Oliveira Moura, and R. Carlson, ""A Step-by-Step Procedure to Perform Preliminary Designs of Salient-Pole Synchronous Generators"," *Energies*, vol. 14, no. 16, p. 4989, 2021. DOI: 10.3390/en14164989.

[106] V. Ostović, *Dynamics of Saturated Electric Machines*. Springer New York, 1989. DOI: 10.1007/978-1-4613-8933-0.

[107] Sudhoff, *"Power Magnetic Devices"*. John Wiley and Sons, 2014, 488 pp., ISBN: 1118489993.

[108] T. J. McDougall and S. J. Wotherspoon, ""A simple modification of Newton's method to achieve convergence of order 1+ 2"," *Applied Mathematics Letters*, vol. 29, pp. 20–25, 2014.

[109] P. Krause, O. Wasynczuk, S. Sudhoff, and S. Pekarek, *"Analysis of Electric Machinery and Drive Systems"*. John Wiley & Sons, Inc., 2013. DOI: 10.1002/9781118524336.

[110] C.-M. Ong, *"Dynamic Simulations of Electric Machinery: Using Matlab/Simulink"*. PRENTICE HALL, Sep. 1, 1997, 656 pp., ISBN: 0137237855.

[111] P. Kundur, N. J. Balu, and M. G. Lauby, *"Power system stability and control"*. McGraw-hill New York, 1994, vol. 7.

[112] O. Sakamoto, Y. Hitotsubashi, and T. Nitta, "Development of a new superconducting generator model for power system transient analysis with XTAP," *IEEE Transactions on Applied Superconductivity*, vol. 25, no. 3, pp. 1–4, Jun. 2015. DOI: 10.1109/tasc.2014.2384732.

[113] R. Kato, O. Sakamoto, and T. Nitta, "Consideration on transient stability of superconducting generator introduced power system by electromagnetic transient analysis," *IEEE Transactions on Applied Superconductivity*, vol. 29, no. 5, pp. 1–5, Aug. 2019. DOI: 10.1109/tasc.2019.2909239.

[114] *Simscape™ Electrical™User's Guide (Specialized Power Systems)*.

[115] *Simulink® User's Guide*.

[116] J. Machowski, Z. Lubosny, J. W. Bialek, and J. R. Bumby, *Power System Dynamics Stability and Control, Stability and Control*. Wiley & Sons, Incorporated, John, 2020, p. 888, ISBN: 9781119526360.

[117] Y. Liu, R. Qu, J. Wang, H. Fang, X. Zhang, and H. Chen, "Influences of generator parameters on fault current and torque in a large-scale superconducting wind generator," *IEEE Transactions on Applied Superconductivity*, vol. 25, no. 6, pp. 1–9, Dec. 2015. DOI: 10.1109/tasc.2015.2493126.

[118] B. Kroposki *et al.*, "Achieving a 100% renewable grid: Operating electric power systems with extremely high levels of variable renewable energy," *IEEE Power and Energy Magazine*, vol. 15, no. 2, pp. 61–73, 2017. DOI: 10.1109/mpe.2016.2637122.

[119] F. Trillaud, "YBCO test coil assembly quench behavior and active protection scheme study," Lecture notes, Massachussets Institute of Technology, Francis Bitter magnetic laboratory, 2007.
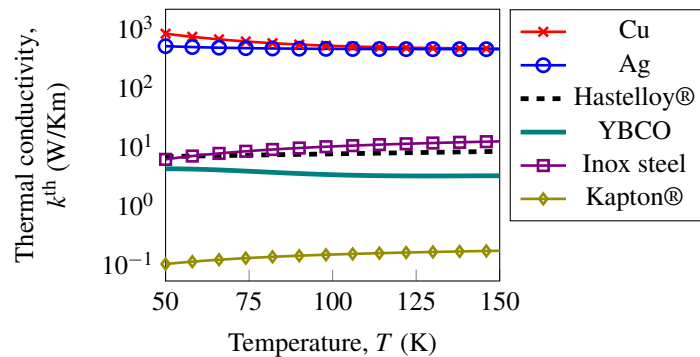
Appendix A

# Material properties for modeling the MC

The polynomials that model the temperature dependence of the electrical resistivity (Fig. A.1), thermal conductivity (Fig. A.2), and heat capacity (Fig. A.3) of the materials in the modular cryostat were extracted from [119].
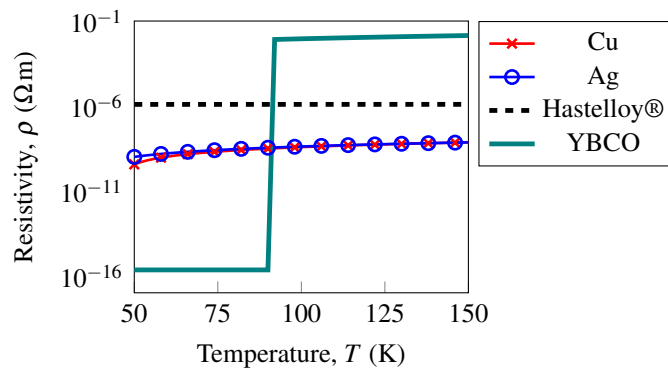
Fig. A.1 Electrical resistivities as a function of temperature.

Fig. A.2 Thermal conductivities as a function of temperature.
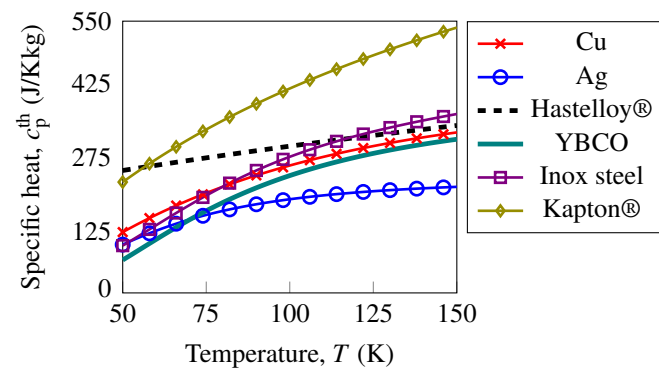
Fig. A.3 Heat capacities as a function of temperature.

Appendix B

Convergence for nodal and mesh analysis

The nonlinear circuit shown in Figure 3.20b, which consists of an iron reluctance and an MMF source, is a nonlinear system that can be represented in terms of either the magnetic flux Φ as shown in (B.1) or the magnetomotive force F_{mm} given by (B.2), respectively.

$$F_{\mathrm{mm}}(\Phi) = R_{\mathrm{m}}(\Phi)\, \Phi \tag{B.1}$$

$$\Phi(F_{\mathrm{mm}}) = P_{\mathrm{m}}(F_{\mathrm{mm}})\, F_{\mathrm{mm}} \tag{B.2}$$

These nonlinear equations can be solved numerically with the nodal or mesh formulations by applying the Newton-Raphson algorithm. In order to briefly highlight the main advantage of the mesh formulation over the nodal formulation, the residual functions for both formulations are presented in the following form, respectively,

$$f(\Phi) = R_{\mathrm{m}}(\Phi)\, \Phi - F_{\mathrm{mm}}(\Phi) = 0 \tag{B.3}$$

$$g(F_{\mathrm{mm}}) = P_{\mathrm{m}}(F_{\mathrm{mm}})\, F_{\mathrm{mm}} - \Phi(F_{\mathrm{mm}}) = 0 \tag{B.4}$$

The corresponding circuit is solved through both formulations under a semi saturated condition of 1.6 T. In order to easier the figure visualization, the residual functions given in (B.3) and (B.4) are normalized with the maximum value obtained over the chosen ranges of $-\Phi_x : \Phi_x$ and $-U_{\mathrm{m,x}} : U_{\mathrm{m,x}}$, respectively. The results, given in Fig. B.1, show that mesh analysis has a significant advantage over nodal analysis due to the reduction of iterations needed to converge through the Newton-Raphson algorithm. Moreover, nodal analysis tends to oscillate and even does not converge when saturated values above 1.8 T are presented in the magnetic iron. This problem can be stated straightforwardly through the nodal-based residual function shown in Fig. B.1b.

The resultant curve changes sharply in a short interval around the magnetic potential $U_m = 0$ and remains quasi-linear at the borders. It should be noted that the MMF drop corresponds to the magnetic scalar potential difference between the magnetic nodes "a" and "b" of the corresponding magnetic circuit represented as $F_{mm}^d = U_a - U_b$. In this case, the node "b" is the reference node, so $U_b = 0$, while U_a is represented as the magnetic potential U_m given in Fig. B.1b.

The larger the saturation value is, the farther from zero the node potential will be. Therefore, when solving the problem through the Newton-Raphson algorithm, the iterated value of the independent variable could fall near the curve's sharp zone and start oscillating without convergence. On the contrary, the mesh-based residual function in the mesh analysis does not present neither a sharp variation zone nor oscillations, while convergence is easier to obtain despite a bigger saturation value as shown in Fig. B.1a.

(a) Mesh-based solution procedure   (b) Nodal-based solution procedure
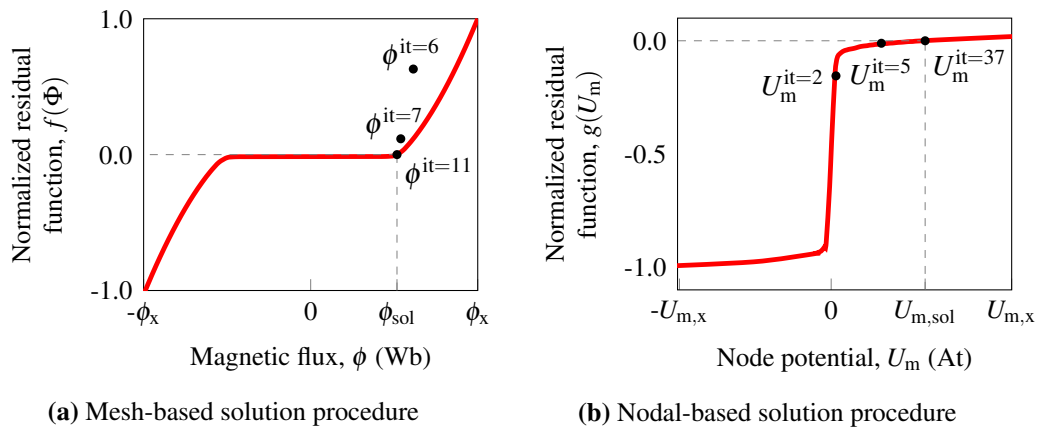
Fig. B.1 Solution of a nonlinear magnetic circuit by applying both mesh and nodal analysis. The tolerance error is constrainted to 0.01.

Appendix C

SM electrical Parameters

This appendix presents the equations to compute the main electrical parameters of a wound-rotor synchronous machines neccesary to simulate the dq0 SM model.

The phase armature resistance R_s is given by,

$$R_s = \rho_{Cu} \frac{N_{\Phi s} l_{av}}{A_{stc}} \tag{C.1}$$

where A_{stc} is the stator conductor cross-section area and l_{av} is the average length of one stator turn. The copper resistivity is assumed at ambient temperature.

The stator magnetizing inductance L_m is obtained as follows,

$$L_m = \mu_0 \frac{2m}{\pi \, p \, k_C} \alpha_{sat} \, l_{eff} \, \tau_{spp} \left(k_{w1} N_{\Phi s} \right)^2 \tag{C.2}$$

where m, l_{eff}, τ_{spp}, k_C and k_{w1} are the number of stator phases, the effective axial length (stator back iron length), the stator pole pitch, the Carter's factor and the winding factor for the fundamental component, respectively.

The dq-axis mutual inductances L_{md} and L_{mq} are computed by applying the reduction factors k_{ad} and k_{aq} to (C.2), as follows,

$$L_{md} = k_{ad} L_{md} ; \qquad L_{mq} = k_{aq} L_{md} \tag{C.3}$$

The reduction factors in the d and q axis are approximated by the expressions,

$$k_{ad} = k_{shr} + \frac{\sin(\pi k_{shr})}{\pi} \tag{C.4}$$

$$k_{aq} = k_{shr} - \frac{\sin(\pi k_{shr})}{\pi} + \frac{2}{3\pi}\cos(0.5\pi k_{shr}) \tag{C.5}$$

where $k_{shr} = w_{sh}/\tau_{rpp}$ is the ratio of the rotor tip arc width and the rotor pole pitch.

The stator leakage inductance L_{ls} is defined as,

$$L_{ls} = L_{lslot} + L_{lgap} + L_{lend} + L_{ltip} \tag{C.6}$$

where L_{lslot}, L_{lgap}, L_{lend} and L_{ltip} are the leakage inductances corresponding to the stator slots, the air gap, the end winding and the stator tip (tooth), respectively. The expressions for compute these leakage inductances are given by,

$$L_{lslot} = \frac{4m}{N_{ss}}\mu_0 k_{p,slot} l_{eff} N_{\Phi s}^2, \qquad L_{lgap} = k_{gleak} L_m$$

$$L_{ltip} = \frac{4m}{N_{ss}}\mu_0 k_{p,tip} l_{eff} N_{\Phi s}^2, \qquad L_{lend} = \frac{4}{p} N_{\Phi s}^2 P_{m,end}$$

where $k_{p,slot}$, $k_{p,tip}$, k_{gleak} and $P_{m,end}$ are the specific slot permeance, the specific tip permeance, the leakage air gap factor, and the end winding permeance, respectively.

As the rotor is a superconducting one and the field coil is enveloped in a modular cryostat, the development of analytical expressions to compute the rotor leakage inductance become a complex task. Furthermore, there are no sources in the literature for calculating this value analytically because of the variety of design concepts and the lack of research on HTS machines modeled with lumped parameters. Therefore, an approximated rotor leakage inductance value is obtained from conventional machines theory given by the next expression,

$$L_{lfd} = p\left(L_{lrtip} + L_{lpole} + L_{lrslot}\right) \tag{C.7}$$

where L_{lrslot}, L_{lpole} and L_{lrtip} are the rotor leakage inductances corresponding to the rotor slots, the interpolar regions, and the pole tip, respectively.

The expressions for compute these leakage inductances are given by,

$$L_{\text{lrtip}} = \frac{4}{p}\mu_0 k_{\text{p,rtip}} l_{\text{r,eff}} N_{\text{fd,p}}^2$$

$$L_{\text{lpole}} = N_{\text{fd,p}}^2 P_{\text{m,int}}$$

$$L_{\text{lrslot}} = N_{\text{fd,p}}^2 P_{\text{m,rslot}}$$

where $k_{\text{p,rtip}}$, $P_{\text{m,int}}$, $P_{\text{m,rslot}}$ are the specific rotor tip permeance, the interpolar region permeance and the rotor bars slots, respectively.

An approximation of the damping resistance and damping inductance are calculated direclty in pu through the next expression,

$$R_{\text{damp}} = \frac{2m\rho_{\text{bar}}}{p}(k_{\text{w1}}N_{\Phi\text{s}})^2 \left(\frac{w_{\text{pt}}l_{\text{reff}}}{\tau_{\text{rpp}}N_{\text{bars}}A_{\text{bar}}} + \frac{D_{\text{ring}}\rho_{\text{ring}}}{\rho_{\text{bar}}\pi p A_{\text{ring}}} \right) \tag{C.8}$$

$$L_{\text{damp}} = 2\mu_0 m l_{\text{reff}} w_{\text{pt}} \frac{(k_{\text{w1}}N_{\Phi\text{s}})^2}{p\tau_{\text{rpp}}N_{\text{bars}}} \left(k_{\text{p,rslot}} + \frac{0.131 w_{\text{pt}} D_{\text{sin}}}{p\tau_{\text{rpp}}N_{\text{bars}}k_{\text{C}}l_{\text{gap}}} \right) \tag{C.9}$$

where N_{bars}, A_{ring}, A_{bars}, D_{ring}, l_{reff}, $k_{\text{p,rslot}}$, D_{sin} are the number of damping bars, the short-circuit ring cross-section area, the damping bars cross-section area, the shortcircuit ring diameter, the rotor effective length (rotor iron length), the specific rotor slot permeance and the inner stator diameter, respectively. The resistivities ρ_{bar} and ρ_{ring} are equal to ρ_{Cu}.

The wind turbine inertia moment J_{turbine} is given in. The rotor inertia moment J_{rotor} is computed by using the FEM. Therefore, the approximation of the total inertia moment J_{total} yields,

$$J_{\text{total}} = J_{\text{rotor}} + J_{\text{turbine}} \tag{C.10}$$

Appendix D

HTS SM Simulink block description

The Simulink SM block model is presented in this appendix. It is based on the governing system of equations given in (3.48), (3.49), and (3.50). The masked and unmasked Simulink SM blocks are shown in Figs. D.1a and D.1b, respectively. The block model consists of three principal sub-blocks: the light blue sub-block converts SimPower voltage signals into Simulink variables; the dark green sub-block converts Simulink stator currents variables i_a, i_b and i_c into SimPower current signals; and the dark gray sub-block describes the electromechanical conversion system model. The corresponding inputs to the block model are the mechanical torque τ_m, the internal voltage E_i, and the stator voltages v_{sa}, v_{sb} and v_{sc}.

(a) Masked SM block   **(b)** Unmasked SM block
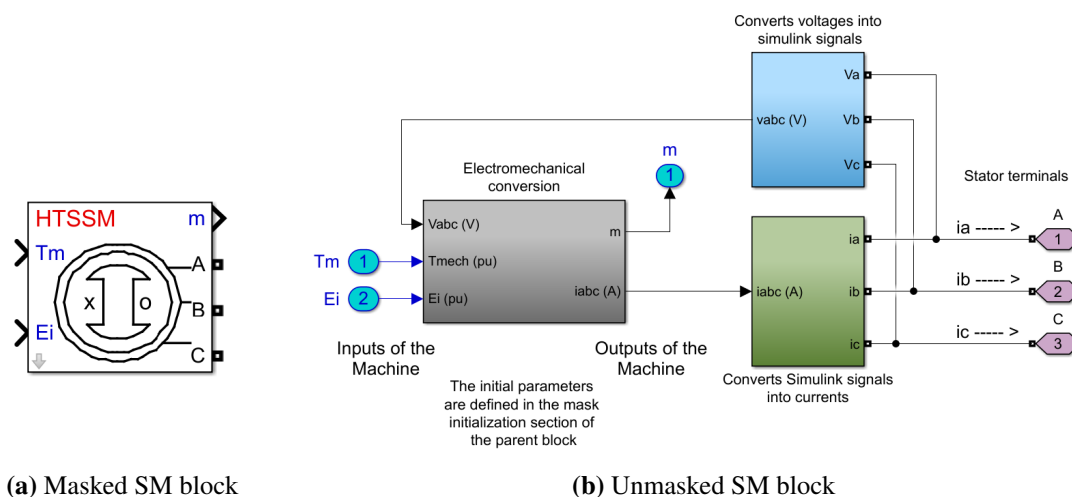
Fig. D.1 Synchronous machine block developed in Simulink.

The electromechanical conversion sub-block system shown in Fig. D.2 consists of three main blocks: the electrical model, the mechanical model and the measurements block.
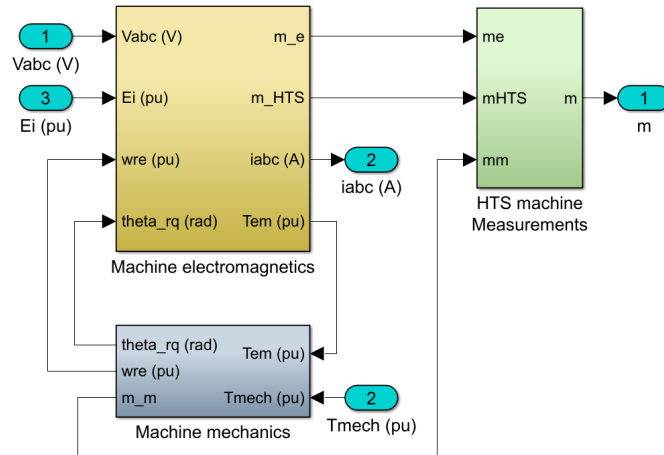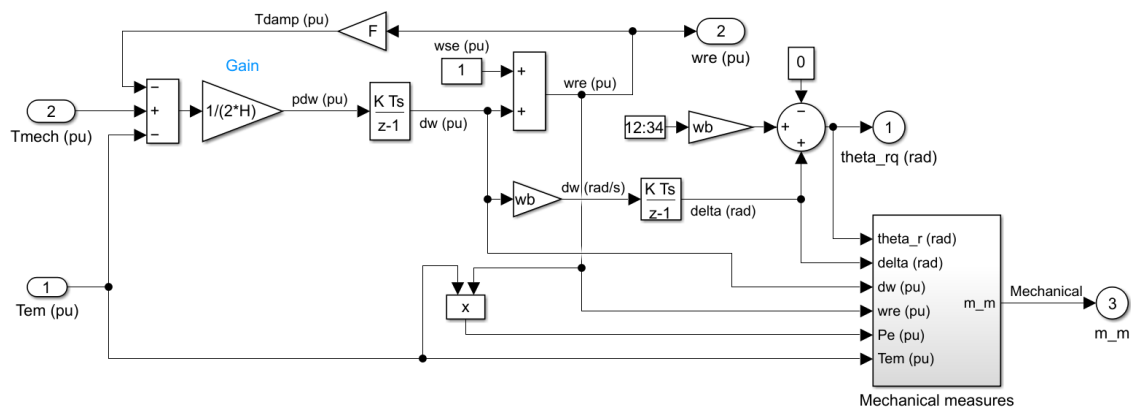
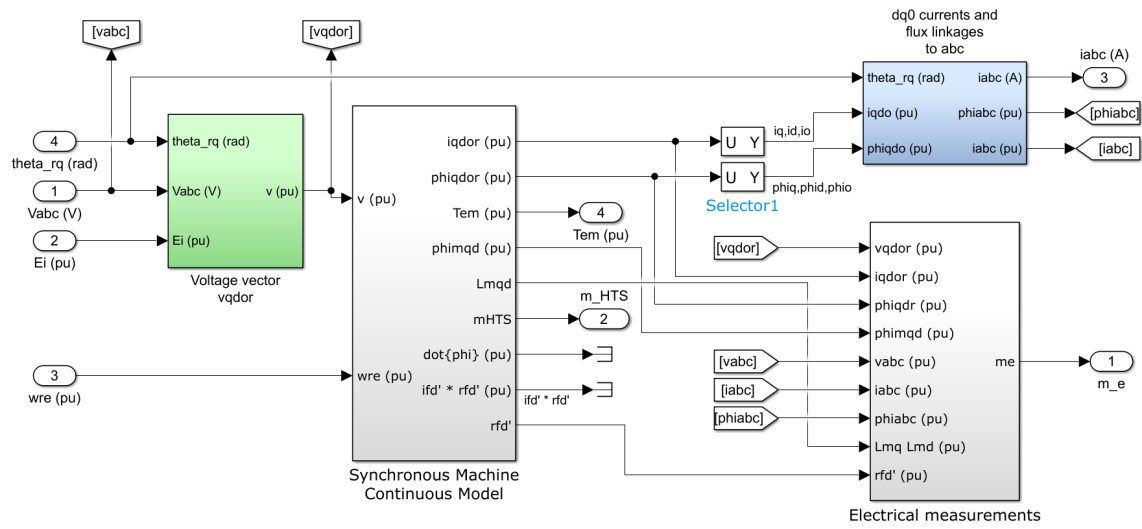**Fig. D.2** Blocks conforming the electromechanical conversion system model.

The mechanical model, whose inputs are the mechanical and the electromagnetic torques, is represented by the block diagram shown in Fig. D.3 and governed by the following state variables,

$$\frac{\mathrm{d}\Delta\omega_r}{\mathrm{d}t} = \frac{1}{2H_{in}}\left(\tau_m - \tau_e\right) \tag{D.1}$$

$$\frac{\mathrm{d}\delta}{\mathrm{d}t} = \Delta\omega_r \tag{D.2}$$

**Fig. D.3** Mechanical block diagram and its corresponding description.

Fig. D.4 SM mechanical block diagram.

In order to solve the electrical model, the internal voltage input E_i is refered to the stator v'_{fd}, while the simulink phase voltage variables are transformed into the dq0 frame-of-reference using the Park transformation (Fig. D.5), as follows,

$$\mathbf{v}_{dq0} = \mathbf{T}_{Park} \mathbf{v}_{abc} \tag{D.3}$$

The state variables, the electromagnetic torque and other calculations related to the inclusion of the saturation in the machine are computed in the SM continuous model block of Fig. D.6. The outputs of such a block include the electromagnetic torque, the "dq0" mutual inductances, the machine currents, the flux linkages, the state variables vectors, and all the HTS field coil variables of interest as the redistribution currents, the temperatures, the resistances, the power losses and the magnetic flux density.
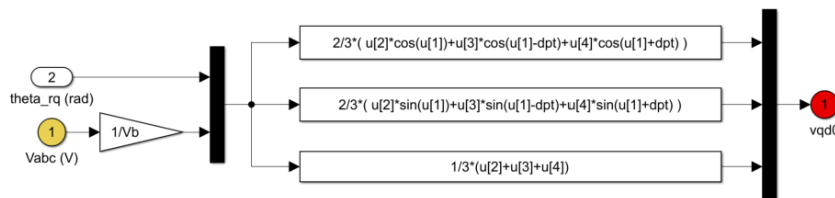
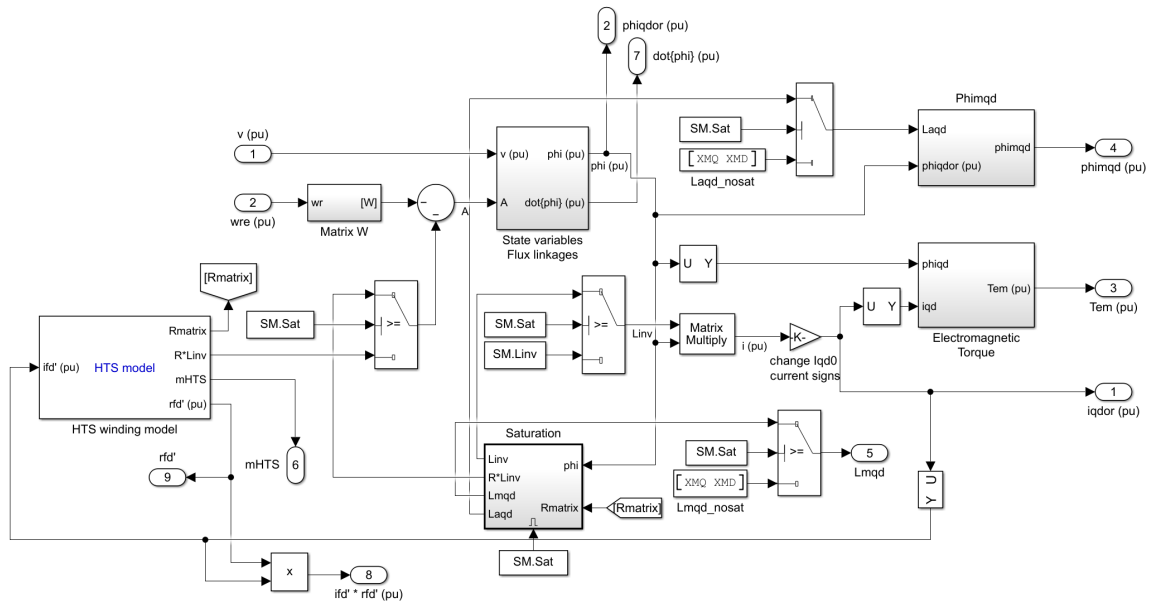**Fig. D.5** Park transformation block diagram.

Fig. D.6 SM model continuous block diagram.

The elements of the HTS model block given in Fig. D.7, transforms the field current referred to the stator into the rotor frame-of-reference. This field current is then used to feed a Matlab function containing the thermoelectromagnetic HTS field coil model which computes the HTS field coil resistance and then added into the resistance matrix R.
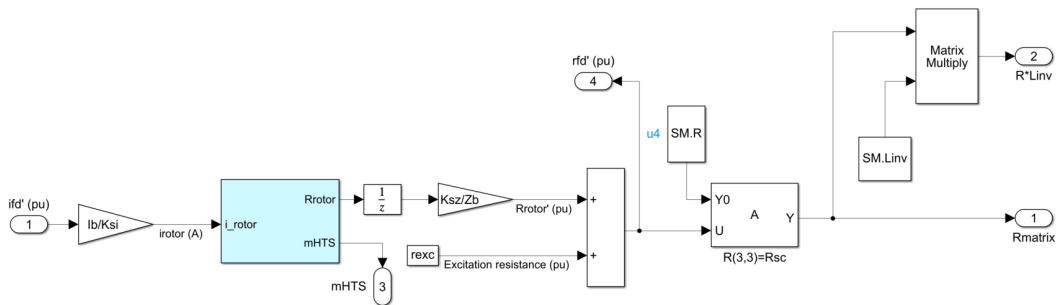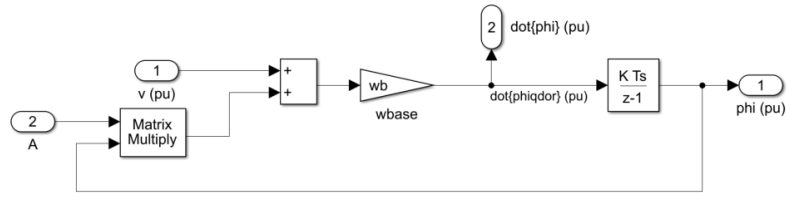

Fig. D.7 HTS model block diagram.

Fig. D.8 State variables and flux linkages block diagram.

Subsequently, the transformed voltages, the inductance matrix L, the angular velocity matrix W and the resistance matrix R containing the nonlinear field coil resistance, conforms the the state variables block illustrated in Fig. D.8, and governed by,

$$\frac{d\boldsymbol{\lambda}_{\mathrm{dq0,r}}}{dt} = \omega_{\mathrm{rb}} \left(\mathbf{v}_{\mathrm{dq0,r}} - \left(\mathrm{RL}^{-1} - \mathrm{W} \right) \boldsymbol{\lambda}_{\mathrm{dq0,r}} \right) \tag{D.4}$$

The machine current vector is then computed as $\mathbf{i}_{\mathrm{dq0,r}} = \mathrm{L}^{-1} \boldsymbol{\lambda}_{\mathrm{dq0,r}}$, and the electromagnetic torque, governed by (D.5), is constructed with the block diagram of Fig. D.9.

$$\tau_{\mathrm{e}} = \frac{3p}{4} \left(\lambda_{\mathrm{d}} i_{\mathrm{q}} - \lambda_{\mathrm{q}} i_{\mathrm{d}} \right) \tag{D.5}$$
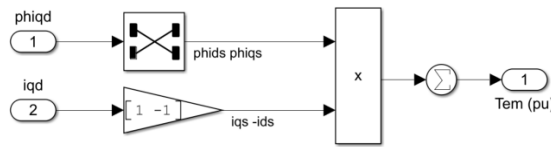
Fig. D.9 Electromagnetic torque block diagram.

The "dq0" stator currents included in the current vector $\mathbf{i}_{\mathrm{dq0,r}}$ are transformed to the "abc" domain by applying the inverse of the Park transformation (Fig. D.10). Finally, the Simulink signals corresponding to the "abc" currents are then converted to SimPower systems signals.
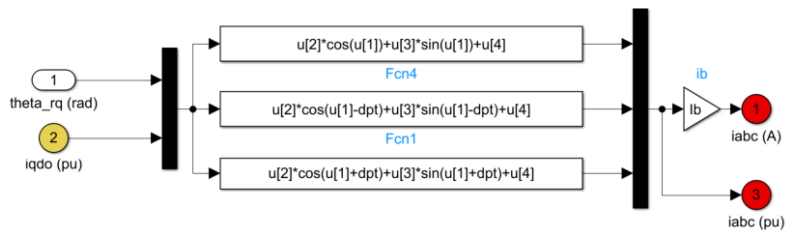
Fig. D.10 Inverse of Park transformation block diagram.